

**DRIFTER STUDY OF CIRCULATION NEAR INDIAN RIVER INLET, DE**

by

Douglas Krafft

A thesis submitted to the Faculty of the University of Delaware in partial fulfillment of the requirements for the degree of Master of Civil Engineering

Summer 2017

© 2017 Douglas Krafft  
All Rights Reserved

**DRIFTER STUDY OF CIRCULATION NEAR INDIAN RIVER INLET, DE**

by

Douglas Krafft

Approved: \_\_\_\_\_  
Jack A. Puleo, Ph.D.  
Professor in charge of thesis on behalf of the Advisory Committee

Approved: \_\_\_\_\_  
Sue McNeil, Ph.D.  
Chair of the Department of Civil and Environmental Engineering

Approved: \_\_\_\_\_  
Babatunde A. Ogunnaike, Ph.D.  
Dean of the College of Engineering

Approved: \_\_\_\_\_  
Ann L. Ardis, Ph.D.  
Senior Vice Provost for Graduate and Professional Education

## ACKNOWLEDGMENTS

Funding for this project was provided by the Delaware Department of Natural Resources and Environmental Control.

I would like to thank my advisor, Dr. Jack Puleo, for his unfailing support and guidance in the project but also a broader professional career. From the numerous conversations about how to approach the project to the many trips around Newark to see if the GPS worked, I owe an enormous debt of gratitude. I could not have completed this project without his help.

I would also like to thank everyone who helped on field work. I appreciate the contributions of Nicholas DiCosmo, Patricia Chardon-Maldonado, Ryan Mieras, Demetra Cristaudo, Michaela McGuire, and Matthew Doelp who helped in the experiments, I could not have collected data without their help. I would like to thank Matt Doelp for substituting for me on the research vessel not once but twice. Additionally, I would like to thank Nicholas DiCosmo and Mohammed Keshtpoor for their previous works on the Indian River Inlet, which proved invaluable in understanding the area. I also would like to thank Nicholas DiCosmo for his collection and processing of Aquadopp data, which was directly used for model validation, as well as his compilation of bathymetry, from which the model bathymetry data was determined. I would also like to thank Michael Davidson for his help resolving RF noise issues. Many thanks to Ryan Mieras as well for his adept and frequent MATLAB help.

I would like to thank Jeremiah Kogon from OC Dive Boat Scuba Charters and Captain Kevin Beam from the University of Delaware for their help releasing and collecting drifters. I would also like to thank Jonathan Harp, from CPHT Manufacturing Inc., for fabricating drifter fins and mounts.

## TABLE OF CONTENTS

LIST OF TABLES .....	vii
LIST OF FIGURES .....	viii
ABSTRACT .....	xv
Chapter	
1 INTRODUCTION .....	1
1.1 Hydrodynamics Associated with Inlets .....	3
1.2 Morphology Associated with Inlets.....	5
1.3 Study Motivation and Approach .....	7
2 STUDY AREA.....	9
2.1.1 Study Area Generalized Hydrodynamic Forcing Conditions.....	11
2.1.2 Indian River Inlet Area Morphology.....	12
2.2 Previous Hydrodynamic Studies near the Indian River Inlet .....	14
2.2.1 NearCoM Simulations of Hydrodynamics to the North of the Indian River Inlet.....	14
2.2.2 Eulerian Measurements to the North of the Indian River Inlet ...	15
2.3 Project Objectives and Overview .....	18
3 INSTRUMENTATION .....	20
3.1 Lagrangian Drifters .....	20
3.1.1 Lagrangian Drifter Design.....	21
3.1.2 Wind Slippage .....	24
3.1.2.1 Wind Slippage Resistant Drifter.....	26
3.1.3 Depth-Dependent Wave Impacts on Drifter Velocities.....	29
3.2 Drifter Tracking System .....	32
3.2.1 Drifter GPS System .....	33
3.2.2 GPS System Post-Processed Accuracy .....	35
3.3 Drifter Deployment Strategy .....	38

4	DRIFTER FIELD DATA .....	39
4.1	Field Experiment I.....	41
4.2	Field Experiment II.....	46
4.3	Field Experiment III .....	51
4.4	Field Experiment IV .....	56
4.5	Field Experiment Results Separated by Tidal Phase.....	61
5	DELFT3D LARGE-SCALE 2D SIMULATION.....	69
5.1	Tidal Forcing Simulations with Delft3D-Flow .....	70
5.1.1	Delft3D-FLOW Computational Grid .....	71
5.1.2	Delft3D-FLOW Boundary Conditions .....	73
5.2	Wave Forcing Component of Simulations with Coupled Delft3D- FLOW/WAVE.....	75
5.2.1	Delft3D-WAVE Computational Grid.....	76
5.2.2	Delft3D-WAVE Boundary Conditions .....	78
5.3	Numerical Model Setup Validation.....	80
5.3.1	Willmott Skill Score .....	80
5.3.2	Simulation Willmott Skill Scores .....	82
5.4	Simulated Drifter Tracks .....	94
5.4.1	Comparisons of Simulated and Observed Drifter Tracks.....	96
5.4.2	Comparisons of Drifter Tracks Simulated with Different Bathymetries.....	103
5.4.3	The Relative Importance of Tide and Wave Forcing to Current Patterns near the Indian River Inlet .....	107
6	CONCLUSIONS .....	111
	REFERENCES .....	114

## LIST OF TABLES

Table 1:	Wave characteristics for NearCoM simulations of hydrodynamics near the Indian River Inlet.....	15
Table 2:	Tidal harmonic constituents from ADCIRC 2015 database applied at boundary sections in Delft3D-FLOW simulations.....	74
Table 3:	Willmott skill scores, indices of agreement (d), for all hydrodynamic properties and all Aquadopp locations considered.....	83
Table 4:	Refined Willmott skill scores, refined indices of agreement ( $d_r$ ), for all hydrodynamic properties and all Aquadopp locations considered.....	83
Table 5:	Water level (h), easting velocity (u), and northing velocity (v) Willmott skill score (index of agreement, d) validations for simulations with and without wave forcing. ....	108
Table 6:	Willmott skill score differences in water level, easting velocity, and northing velocity validations with and without wave forcing. ....	109

## LIST OF FIGURES

Figure 1:	Schematized inlet, separated into morphologic features. ....	2
Figure 2:	Delaware Atlantic Coast (Google Earth).....	9
Figure 3:	The Indian River Inlet and surrounding shoreline on 7/9/2015 (Google Earth). ....	11
Figure 4:	Lagrangian drifters following currents to the north of the Indian River Inlet in Delaware. ....	19
Figure 5:	Schematic of drifter components indicating vertical dimensions and the location of the computed water line, estimated center of buoyancy (B), and estimated center of gravity (G).....	23
Figure 6:	Wind slippage induced velocity as a function of windspeed for drogues with rectangular cross-sections and subaerial cylindrical poles of approximate projected area $0.045 \text{ m}^2$ (Murray, 1975). Lines for various typical drogue dimensions $L$ are presented. ....	25
Figure 7:	Wind slippage resistant drifter designed and constructed to investigate the impact of wind slippage on tracks from the primary drifters. ....	28
Figure 8:	Drifter IP68 waterproof electronics box containing GPS system (i.e. GPS receiver, antenna cable, and data logger). ....	34
Figure 9:	Results from the 10/13/15 accuracy test A) Leica GS15 GNSS data with RTK corrections and the drifter GPS system as paths followed by the cart. B) Cart velocity as determined by time differencing running averaged antenna positions.....	36
Figure 10:	(A) plot of drifter GPS system RMSE in $\text{m s}^{-1}$ as a function of running average window size in s. (B) plot of $r^2$ between drifter GPS system and RTK corrected Leica GS15 GNSS as a function of running average window size in s. ....	37
Figure 11:	Drifters as transported by research vessel within the Indian River Inlet. The DE Route 1 bridge at the Indian River Inlet visible in background. ....	38

Figure 12: A) Idealized tidal curve divided into twelve phases. Color indicates tidal phase. B) Drifter tracks from all four field experiments plotted over bathymetry data. Drifter position time series have been filtered with a running average using a window size of 120 s. Line color indicates drifter track tidal phase. Release points are indicated in cyan. Dashed white overlays on plotted drifter tracks indicate wind slippage resistant drifter paths. A line at zero m in Mean Sea-Level (MSL) coordinates is plotted with increased thickness and varying black and white coloring..... 40

Figure 13: A) Idealized tidal curve divided into twelve phases. Color indicates tidal phase grouping. B) Drifter tracks collected in the first field experiment on 05/26/2016 plotted over model input bathymetry. Color indicates tidal phase. Release points are indicated in cyan. Drifter position time series have been filtered with a running average using a window size of 120 s. Plot coordinates are referenced to a local northing and easting with an origin at the north jetty tip. .... 43

Figure 14: A) Measured wind speed during the observed tidal cycle at the Delaware Environmental Observing System (DEOS) station 2.7 km north of the Indian River Inlet in the first field experiment ([http://www.deos.udel.edu/data/daily\\_retrieval.php](http://www.deos.udel.edu/data/daily_retrieval.php)). Color indicates tidal phase, specified in Figure 13a. B) Measured wind direction during the observed tidal cycle at the DEOS station near the Indian River Inlet. Color indicates tidal phase. .... 44

Figure 15: A) Significant wave height determined from measured wave spectra at the USACE wave gauge DE003 DWG-BB03 off of Bethany Beach during the first field experiment (<http://www.frf.usace.army.mil/bethanybeach/bb.shtml>). Color indicates tidal phase, specified in Figure 13a. B) Wave direction measured at the USACE wave gauge east of Bethany Beach. Color indicates tidal phase..... 45

Figure 16: A) Idealized tidal curve divided into twelve phases. Color indicates tidal phase grouping. B) Drifter tracks collected in the second field experiment on 10/20/2016 plotted over bathymetry. Color indicates tidal phase. Release points are indicated in cyan. Drifter position time series have been filtered with a running average using a window size of 120 s. Plot coordinates are referenced to a local northing and easting with an origin at the north jetty tip..... 48

Figure 17:	A) Measured wind speed during the observed tidal cycle north of the Indian River Inlet in the second field experiment ( <a href="http://www.deos.udel.edu/data/daily_retrieval.php">http://www.deos.udel.edu/data/daily_retrieval.php</a> ). Color indicates tidal phase, specified in Figure 16a. B) Measured wind direction during the observed tidal cycle north of the Indian River Inlet. Color indicates tidal phase.....	49
Figure 18:	A) Significant wave height determined from measured wave spectra off of Bethany Beach during the second field experiment ( <a href="http://www.frf.usace.army.mil/bethanybeach/bb.shtml">http://www.frf.usace.army.mil/bethanybeach/bb.shtml</a> ). Color indicates tidal phase, specified in Figure 16a. B) Wave direction measured off of Bethany Beach. Color indicates tidal phase.....	50
Figure 19:	A) Idealized tidal curve divided into twelve phases. Color indicates tidal phase grouping. B) Drifter tracks collected in the third field experiment on 05/08/2017 plotted over bathymetry. Color indicates tidal phase. Release points are indicated in cyan. Drifter position time series have been filtered with a running average using a window size of 120 s. Plot coordinates are referenced to a local northing and easting with an origin at the north jetty tip.....	53
Figure 20:	A) Measured wind speed during the observed tidal cycle north of the Indian River Inlet in the third field experiment ( <a href="http://www.deos.udel.edu/data/daily_retrieval.php">http://www.deos.udel.edu/data/daily_retrieval.php</a> ). Color indicates tidal phase, specified in Figure 19a. B) Measured wind direction during the observed tidal cycle north of the Indian River Inlet. Color indicates tidal phase.....	54
Figure 21:	A) Significant wave height determined from measured wave spectra off of Bethany Beach during the third field experiment ( <a href="http://www.frf.usace.army.mil/bethanybeach/bb.shtml">http://www.frf.usace.army.mil/bethanybeach/bb.shtml</a> ). Color indicates tidal phase, specified in Figure 19a. B) Wave direction measured at the off of Bethany Beach. Color indicates tidal phase. ....	55
Figure 22:	A) Idealized tidal curve divided into twelve phases. Color indicates tidal phase grouping. B) Drifter tracks collected in the fourth field experiment on 05/30/2017. Color indicates tidal phase. Drifter position time series have been filtered with a running average using a window size of 120 s. Plot coordinates are referenced to a local northing and easting with an origin at the north jetty tip. ....	58

Figure 23:	A) Measured wind speed during the observed tidal cycle north of the Indian River Inlet during the fourth field experiment ( <a href="http://www.deos.udel.edu/data/daily_retrieval.php">http://www.deos.udel.edu/data/daily_retrieval.php</a> ). Color indicates tidal phase, specified in Figure 22a. B) Measured wind direction during the observed tidal cycle at the north of the Indian River Inlet. Color indicates tidal phase. ....	59
Figure 24:	A) Significant wave height determined from measured wave spectra off of Bethany Beach during the third field experiment ( <a href="http://www.frf.usace.army.mil/bethanybeach/bb.shtml">http://www.frf.usace.army.mil/bethanybeach/bb.shtml</a> ). Color indicates tidal phase, specified in Figure 22a. B) Wave direction measured at the off of Bethany Beach. Color indicates tidal phase. ....	60
Figure 25:	Drifter track data collected in the rising tide separated by tidal phase and plotted on bathymetry. Coordinates are relative to the north jetty tip. Line color indicates tidal phase as defined in Figure 22. Release points are indicated in cyan. ....	62
Figure 26:	Drifter track data (line from cyan dot) collected in the falling tide separated by tidal phase and plotted on bathymetry. Coordinates are relative to the north jetty tip. Line color indicates tidal phase as defined in Figure 22. Drifter release points are indicated in cyan. ....	64
Figure 27:	A-F) Drifter tracks from all field experiments separated into $2\pi/6$ tidal phase groups and plotted over bathymetry. Color represents binned speed between $0 \text{ m s}^{-1}$ and $0.45 \text{ m s}^{-1}$ . G) Speed bins and corresponding colors used to plot drifter tracks as a function of speed. .	67
Figure 28:	A) Model domain and bathymetry. Color displays elevation. The red edge indicates the location of the FLOW boundary conditions. B) Model computational grid resolution. Average M and N direction grid spacing is indicated by color. ....	72
Figure 29:	Wave module outer grid domain and bathymetry. Color displays elevation. The red edge indicates the location of the WAVE boundary conditions. B) Wave module outer computational grid resolution. Average M and N direction grid spacing is indicated by color. ....	77
Figure 30:	Wave module inner grid domain and bathymetry. Color displays elevation. B) Wave module insert computational grid resolution. Average M and N direction grid spacing is indicated by color. ....	78

Figure 31: A) Measured Aquadopp water levels from sites C1 and D1 compared with model predicted water levels at the same locations. B) Measured Aquadopp easting velocities from sites C1 and D1 compared with model predicted easting velocities at the same locations. C) Measured Aquadopp northing velocities from sites C1 and D1 compared with model predicted easting velocities at the same locations. Color indicates Aquadopp site, line width indicates data type (i.e. simulation and measurement)..... 85

Figure 32: A) Measured Aquadopp water levels from sites A2 and B2 compared with model predicted water levels at the same locations. B) Measured Aquadopp easting velocities from sites A2 and B2 compared with model predicted easting velocities at the same locations. C) Measured Aquadopp northing velocities from sites A2 and B2 compared with model predicted northing velocities at the same locations. Color indicates Aquadopp site, line width indicates data type (i.e. simulation and measurement)..... 87

Figure 33: A) Measured Aquadopp water levels from sites A4, B4, C4, D4, and E4 compared with model predicted water levels at the same locations. B) Measured Aquadopp easting velocities from sites A4, B4, C4, D4, and E4 compared with model predicted easting velocities at the same locations. C) Measured Aquadopp northing velocities from sites A4, B4, C4, D4, and E4 compared with model predicted northing velocities at the same locations. Color indicates Aquadopp site, line width indicates data type (i.e. simulation and measurement)..... 89

Figure 36: A) Measured Aquadopp significant wave heights from sites C1 and D1 compared with model predicted significant wave heights at the same locations. B) Measured Aquadopp wave peak periods from sites C1 and D1 compared with model predicted wave peak periods at the same locations. C) Measured Aquadopp mean wave directions from sites C1 and D1 compared with model predicted mean wave directions at the same locations. Color indicates Aquadopp site, line width indicates data type (i.e. simulation and measurement)..... 91

Figure 37: A) Measured Aquadopp significant wave heights from sites A2 and B2 compared with model predicted significant wave heights at the same locations. B) Measured Aquadopp wave peak periods from sites A2 and B2 compared with model predicted wave peak periods at the same locations. C) Measured Aquadopp mean wave directions from sites A2 and B2 compared with model predicted mean wave directions at the same locations. Color indicates Aquadopp site, line width indicates data type (i.e. simulation and measurement)..... 92

Figure 38: A) Measured Aquadopp significant wave heights A4, B4, C4, D4, and E4 compared with model predicted significant wave heights at the same locations. B) Measured Aquadopp wave peak periods from sites A4, B4, C4, D4, and E4 compared with model predicted wave peak periods at the same locations. C) Measured Aquadopp mean wave directions from sites A4, B4, C4, D4, and E4 compared with model predicted mean wave directions at the same locations. Color indicates Aquadopp site, line width indicates data type (i.e. simulation and measurement). ..... 93

Figure 37: Simulated passive tracer paths over 30 minutes representing drifter track predictions plotted over bathymetry. Release points are presented as dots..... 95

Figure 38: A) Simulated water level within the inlet during the first experiment. Six release times are indicated with ‘o’ markers and vertical lines. Times are presented in EDT. B,C,D,E,F,G) Simulated (white) and observed (red) drifter releases during the first field experiment. Simulated (black) and observed (magenta) release locations indicated as dots. Simulated drifter release and collection times were 30 minutes apart. Sufficiently long observed drifter tracks were separated into 30 minute segments. .... 97

Figure 39: A) Simulated water level in the inlet during the second experiment. Six release times are indicated with ‘o’ markers and vertical lines. Times are presented in EDT. B,C,D,E,F,G) Simulated (white) and observed (red) drifter releases during the second field experiment. Simulated (black) and observed (magenta) release locations indicated as dots. Simulated drifter release and collection times were 30 minutes apart. Sufficiently long observed drifter tracks were separated into 30 minute segments. .... 100

Figure 40:	A) Simulated water level within the inlet during the third experiment. Six release times are indicated with ‘o’ markers and vertical lines. Times are presented in EDT. B,C,D,E,F,G) Simulated (white) and observed (red) drifter releases during the third field experiment. Simulated (black) and observed (magenta) release locations indicated as dots. Simulated drifter release and collection times were 30 minutes apart. Sufficiently long observed drifter tracks were separated into 30 minute segments. ....	102
Figure 41:	A) A selection of model input elevation generated using bathymetry option one near the Indian River Inlet, generated entirely from the NOAA post-sandy DEM. Color indicates elevation. B) Model input elevation near the Indian River Inlet using elevation data compiled for the modelling effort of Keshtpoor et al. (2015). C) Elevation differences between bathymetry options one and two near the Indian River Inlet. Color indicates elevation difference, with positive values indicating higher elevations in bathymetry option one. ....	104
Figure 42:	A,C,E,G,I,K) Simulated drifter tracks from model simulations using bathymetry option one, released at the beginning of the $\pi/6$ , $3\pi/6$ , $5\pi/6$ , $7\pi/6$ , $9\pi/6$ , and $11\pi/6$ tidal phases. B,D,F,H,J,L) Simulated drifter tracks from model simulations using bathymetry option two. ....	106
Figure 43:	Model drifter tracks using tidal and wave forcing (white) at various phases of the tidal cycle compared with model drifter tracks using tidal forcing only (red). Release points are presented as dots. Simulated drifter release and collection times were separated by 30 minutes. ....	110

## ABSTRACT

Current patterns were investigated to the north of the stabilized lower-mesotidal Indian River Inlet located on the Delaware Atlantic Coast with Lagrangian drifter measurements and numerical model simulations. A suite of GPS-tracked current-following drifters were deployed north of the Indian River Inlet, near the site of severe and chronic downdrift erosion and numerous sediment nourishments. Over four field experiments drifters measured flow patterns to the north of the Indian River Inlet, collectively spanning the semi-diurnal tidal cycle. Current patterns sufficiently before or after flow reversal within the inlet were found to vary with tidal phase. Hydrodynamics near the inlet were simulated during drifter field experiments and the Eulerian current meter deployments of a previous study using a 2D dynamically coupled Delft3D-FLOW and DELFT3D-WAVE model of the Delaware Atlantic Coast and Delaware Bay. Simulation water levels, velocities, significant wave heights, peak periods, and wave directions were validated with data collected near the inlet, yielding validations of mean Willmott score  $0.54 \pm 0.25$ . Simulated flow patterns were assessed through qualitative comparison with observed drifter tracks to indicate reasonable agreement in the falling tide and conditional agreement during the middle of the rising tide. Numerical simulations indicated that tidal forcing dominates current patterns over the study area. Accurate bathymetry was also determined to be important to hydrodynamic predictions in the area.

## **Chapter 1**

### **INTRODUCTION**

Tidal inlets connect the open sea to back-barrier system and have substantial ecological and socioeconomic impacts. Waterways through inlets provide a route for economic and recreational navigation as well as fish and larvae migration, and maintain water quality and salinity levels in back-barrier systems. Tidal inlet shape can differ widely as the result of various hydrodynamic-morphodynamic interactions. On alluvial coasts, tidal inlets may generally be considered in three parts: an ocean (ebb) section, a bay (flood) section, and a gorge section connecting the two (Figure 1; Bruun, 1995). Sediment deposits in the form of shoals or bars are often located in the ebb or flood sections of inlets (Fitzgerald, 1996). Tidally forced flows through inlets often transport large quantities of sediment and have major influences on the surrounding morphology. The maintenance of inlets must often address the stability of navigation channels and the adjacent shorelines. Due to wave and tidal forcing, inlets are often ephemeral and can migrate. The unique hydrodynamics, wave-current interaction, and sediment transport at tidal inlets are among the many aspects of inlets studied. Topics in tidal inlet hydrodynamics include the current patterns (e.g., Davis and Fox, 1981; Dissanayake et al., 2009), current impacts on waves (e.g., Olabarrieta et al., 2011; Dodet et al., 2013; Chen et al., 2015), and wave impacts on currents (e.g., Shi et al., 2011; Orescanin et al., 2014; Wargula et al., 2014; Keshtpoor et al., 2015) in and around tidal inlets. Subjects contained within the study of sediment transport patterns around inlets include inlet stability (e.g., Bruun and Gerritsen, 1960; O'Brien,

1967 ; Bertin et al., 2009) and coastal morphology in the vicinity of inlets (e.g., Bruun, 1995; Galgano, 2009). Substantial research has been and is continuing to be done on the physical processes related to tidal inlets.

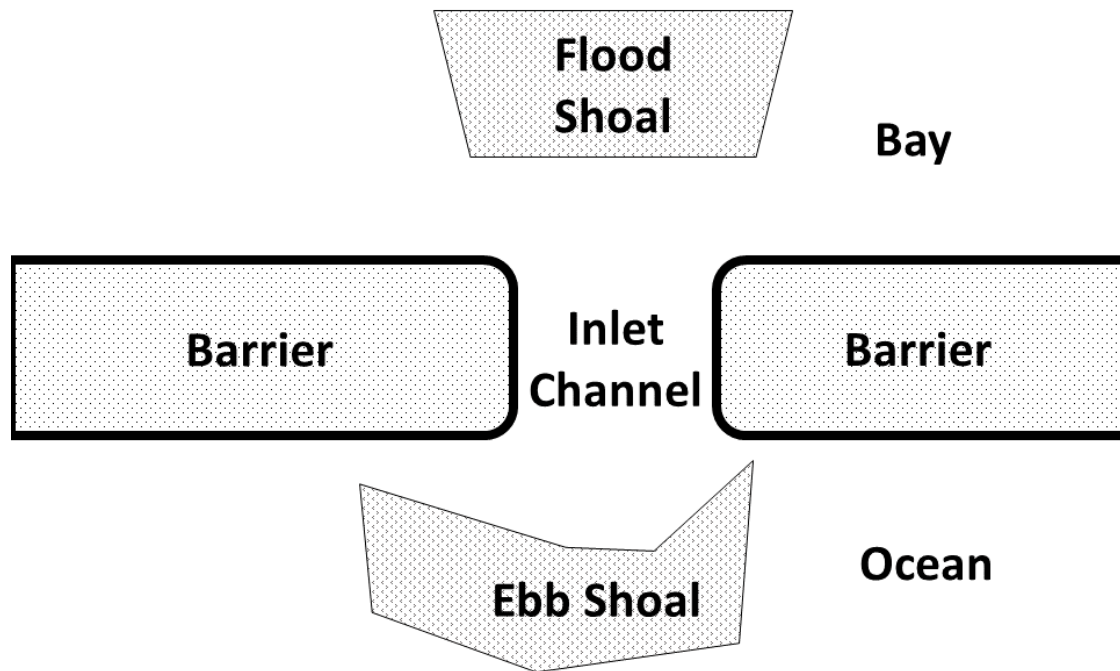


Figure 1: Schematized inlet, separated into morphologic features.

## **1.1 Hydrodynamics Associated with Inlets**

The complexities of current patterns and wave-current interactions at tidal inlets are two well researched topics among the many within the subject of hydrodynamics associated with inlets. Flow characteristics around inlets are complicated, often containing unique patterns controlled by local hydro-geological interactions with large spatial and temporal variability. Field measurements of wave parameters and currents in and around the Matanzas River Inlet, Fl., have suggested that hydrodynamic impacts of tidal inlets are complicated but diminish substantially over distance, with negligible effects on currents more than 0.5 km from a microtidal inlet (Davis and Fox, 1981). Model simulations have also demonstrated the complexities of inlet circulation patterns in showing that they should be considered as no simpler than two-dimensional transient non-linear systems (Hench and Luettich, 2003). Unique circulation patterns, sometimes similar to eddies, are not uncommon at tidal inlets. Two-dimensional horizontal process-based model simulations of the schematized area around the Ameland inlet, in the Netherlands, contain mobile flow divergence and convergence areas and a rotational current field which varies with tidal cycle (Dissanayake et al., 2009). Simulated hydrodynamics near the New River Inlet, NC, also include “eddy-like circulation patterns” with flow speeds partially controlled by wave height (Chen et al., 2015). It has been well established through a variety of studies that current patterns in the vicinity of tidal inlets frequently include unique localized current patterns.

Wave-current interactions form another commonly studied topic in the subject of hydrodynamics around inlets. Wave-current interactions may be divided into two categories: the impact of currents on wave properties and the impact of waves on currents. Currents in areas surrounding many tidal inlets have been found to be

relevant to simulated wave processes such as refraction, wave breaking and turbulence. Three-dimensional Coupled Ocean-Atmosphere-Wave-Sediment Transport (COAWST) model simulations of Willapa Bay, Washington, suggest that tidal currents play an important role in wave refraction (Olabarrieta et al., 2011). Tidal current-induced refraction is also observed to decrease wave heights by up to 10% in coupled wave circulation model simulations of the Albuferia Lagoon, on the southern coast of Portugal, and the nearby barrier beach-inlet-lagoon system (Dodet et al., 2013). At the New River Inlet, North Carolina, NearCoM-TVD simulated hydrodynamics revealed local wave height modulation with tidal forcing to be influenced substantially more by changes in water level than tidal currents (Chen et al., 2015). Currents were also found to impact wave breaking and turbulence in an inlet through comparison between existing wave dissipation models and energy flux gradients measured with SWIFT wave following buoys in the New River Inlet (Zippel and Thomson, 2015). Currents have been found to influence a variety of wave processes with relative impacts varying between the diverse hydro-morphologic interactions at different inlets.

The importance of the effect of wave-current interactions on currents generally varies less by location than the importance of impact of wave-current interactions on waves. Wave-current interactions often greatly impact currents near inlets, but the dominant wave processes influencing currents vary substantially between inlets and between inlet components. Alongshore gradients in wave setup, wave-breaking induced acceleration, wave radiation stress and nonlinear current interactions near inlets vary in importance by location. Addressing the impact of waves on currents generally, the inclusion of wave forcing is found to reduce errors in inlet current

predictions in Katama Bay, Massachusetts, by approximately 50% (Orescanin et al., 2014). Near the mouth of the San Francisco Bay, California, NearCoM simulations have shown one of the dominant forces driving local nearshore circulation to be the pressure gradient from ebb shoal refraction and wave focusing induced alongshore variation in wave setup (Shi et al., 2011; Hansen et al., 2013). Near the Indian River Inlet, DE, NearCoM simulations also predicted an alongshore significant wave height gradient and a wave focal point to drive flows (Keshtpoor et al., 2015). At the Willapa Bay entrance wave-breaking-induced acceleration has also been determined to be a leading order term in horizontal momentum balances near the inlet based on 3D fully coupled COAWST model simulations (Olabarrieta et al., 2011). Tide, wave, and current data from the New River Inlet, NC, indicated wave radiation stresses were equal to pressure gradient forcing on the shallower shoals, but only important within the main channel during storms (Wargula et al., 2014). Near the New River Inlet, NC, simulated hydrodynamics indicated that the nonlinear wave current interactions were also important, particularly to residual (tidally averaged) flows (Chen et al., 2015). The results of numerous studies indicate that near tidal inlets waves impact currents through processes including alongshore setup gradients, wave-breaking induced acceleration, wave radiation stress, and nonlinear wave interactions with large variability between inlets in relative influence on currents.

## **1.2 Morphology Associated with Inlets**

Tidal inlets often induce dynamic and complicated morphological responses to wave and tidal forcing in inlet channels and adjacent shorelines, often with direct socioeconomic impacts. Shoal and delta morphology are commonly investigated near inlets. One approach to a standardized model of ebb-tidal delta morphology was

developed largely based on detailed bedform measurements and velocities (Hayes, 1980). Inlet channel and ebb delta morphology have been found to be tidally driven with sizes dependent on tidal asymmetry based on two-dimensional horizontal (2Dh) Delft3D model simulations of the Ameland inlet (Dissanayake et al., 2009). Inlet stability is another topic of interest within the subject of tidal inlet morphology. Tidal inlet stability on alluvial coasts may be defined as the maintenance of navigable depths along a stationary channel. An approximation for relative inlet stability may be expressed as a function of three variables: the ratio of tidal prism to total littoral drift, the ratio of maximum discharge rate through the inlet gorge to total littoral drift, and stability shear stress (Bruun and Gerritsen, 1960). Inlet tidal prism has been suggested to control equilibrium minimum flow as the result of comparisons between spring diurnal tidal prism and minimum entrance channel area at 28 inlets with and without jetties (O'Brien, 1967). Inlet infilling has also been attributed to wave radiation stress gradients, wave refraction around ebb deltas, and lateral free surface gradients based on residual sand transport and hydrodynamics determined from Coastal Area Morphodynamic Modeling System (MORSYS2D) simulations coupled with SWAN and ELCIRC near Óbidos inlet, Portugal (Bertin et al., 2009). Inlet stability has often been addressed by stabilization with jetties and dredging.

The addition of jetties to tidal inlets often provides stabilization and aids in maintaining channels of navigable depth, however, stabilized inlets on littoral drift shores often have a detrimental effect on the nearby shores. Stabilized inlets present a barrier to alongshore transport. Sediment accumulates on the updrift side of the inlet and erodes on the downdrift as a result of the local impediment to sediment transport. The erosion of shorelines downdrift of littoral drift barriers often follow a similar

pattern (Bruun, 1995). A continuously expanding eroding front defines the leading edge of the typical pattern of downdrift erosion because the downdrift littoral sediment transport rates are often greater than natural bypassing mechanisms (e.g., tidal-flow bypassing, bar bypassing). Terms for the cause of long distance downdrift erosion, or the far arc of erosion, include “sediment starvation” and an “imbalance in the littoral drift budget” (Bruun, 2001; Galgano, 2009). The near arc of erosion is characterized by a small area of accretion at the drift barrier and a point which matches the pre-existing erosion, with the greatest rates of shoreline change between the two (Bruun, 1995; Galgano, 2009). In this model, wave refraction from the barrier induces littoral drift towards the inlet for the closer part of the near arc and away from the inlet for the farther part (Bruun, 1995).

### **1.3 Study Motivation and Approach**

Accurate predictions of hydrodynamics and sediment transport are important given the variety of ecological and socioeconomic functions tidal inlets serve, the complicated hydrodynamics surrounding inlets, and the often costly and severe erosion which inlet stabilization can cause. The complexity of hydrodynamics around inlets indicate the possible benefit of a variety of validation techniques. The Indian River Inlet and surrounding shoreline have experienced substantial morphologic rates of change and are described by complicated and highly variable hydrodynamic fields. The downdrift shoreline at the Indian River Inlet, Delaware has been observed to experience severe and chronic erosion and the nearby current patterns have been shown to exhibit high spatial variability (Keshtpoor et al., 2015). Lagrangian drifters yield fine spatial resolutions and have been previously used in tidal inlets, making them applicable the study of the current patterns around the Indian River Inlet.

Lagrangian velocity information is generally determined by recording the difference in position of an object over time. Drifters are intended to be advected with the flow field while acting as a passive tracer. The spatial variety permitted by Lagrangian drifter velocities enables detailed measurements of an area with large horizontal variations in flow velocity.

Lagrangian drifters have been selected repeatedly to investigate surf zone and rip current hydrodynamics (e.g., Schmidt et al., 2003; MacMahan et al., 2009; Austin et al., 2012; Scott et al., 2015). Velocity data from surf zone and rip current Lagrangian drifters have been used in comparisons with various prediction techniques including a nonlinear shallow water equation based numerical model (Schmidt et al., 2005), coupled 2DH XBeach simulations (Scott et al., 2015), and an operational rip current prediction tool on a macrotidal beach in the southwest UK (Austin et al., 2012). Lagrangian drifter velocity information has also proven adequate to calculate dispersion in oceanic (e.g., Molinari and Kirwan, 1975; Okubo and Ebbesmeyer, 1976), estuarine (e.g., Spencer et al., 2014), and surf zone applications (e.g., Johnson and Pattiaratchi, 2004; Spydell et al., 2007; Spydell et al., 2009). Lagrangian velocity techniques have also been applied at tidal inlets. Inlet channel streamline patterns between current meters were obtained with Lagrangian drifters in the field study of the Matanzas River Inlet, Fl. (Davis and Fox, 1981) Drifters were also deployed at the mouth of Beaufort Inlet, NC, to determine nearby flood tide current patterns which indicated features important to larval transport (Churchill et al., 1999). Lagrangian drifters have also been used to study tidal inlet mouth current patterns and lateral cluster spreading rate prediction in 2DH simulated hydrodynamics at the New River Inlet, NC (Spydell et al., 2015).

## Chapter 2

### STUDY AREA

The Delaware Atlantic coast spans the approximately 40 km between Fenwick Island and Cape Henlopen (Figure 2). General shoreline angle is approximately 0.09 radians ( $5^\circ$ ) west of north. The coastal plain geology is constituted of unconsolidated to semi-consolidated Pleistocene and Holocene sands and gravels (Galgano, 2008). Native sediment is defined as well to very well sorted coarse to medium sand with a mean grain diameter ( $d_{50}$ ) of  $0.418 \cdot 10^{-3}$  m and a one standard deviation  $d_{50}$  range between  $0.347 \cdot 10^{-3}$  m and  $0.504 \cdot 10^{-3}$  m (Ramsay, 1999). Delaware beaches are relatively steep with foreshore slopes of 1:5 to 1:15 (Puleo, 2015). Sandbars are not present along the Delaware coast. Post-storm cross-shore profiles and sediment samples have indicated the lack of sandbar forming sediment deposition patterns (Roberts et al., 2013).

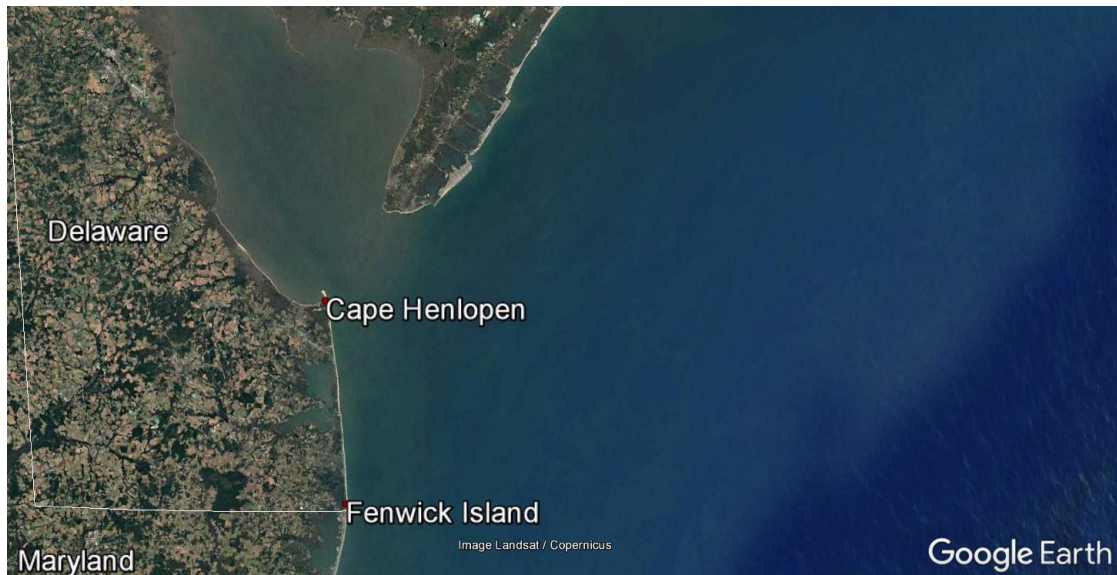


Figure 2: Delaware Atlantic Coast (Google Earth).

The Indian River Inlet forms the only direct connection from the ocean to the Indian River and Rehoboth Bays near the midpoint of the Delaware Atlantic coast (Figure 3). The Indian River Inlet is a stabilized lower mesotidal inlet (Hayes, 1980). The shoreline east of the bays forms a baymouth barrier system (Galgano, 2009). Approximate combined bay surface areas are 35 km<sup>2</sup> with mean low water depths of 1.5 m (Moffatt and Nichol, 2007). Average combined freshwater discharge into the bays has been estimated as 0.92 m<sup>3</sup> s<sup>-1</sup> and is not of major hydrodynamic importance at the inlet (Andres, 1987). The Indian River Inlet was stabilized in 1940 by two 460 m jetties at an approximate width of 150 m in response to migration and episodic closure (Gebert et al., 1992). Several unsuccessful attempts to open the ephemeral inlet between 1928 and 1937 preceded jetty construction. Armoring covers the 365 m of interior shoreline as a result of tidal current induced interior shoreline erosion (Gebert et al., 1992). This study focuses on the circulation and forcing conditions north of the Indian River Inlet, where chronic and severe erosion has occurred.



Figure 3: The Indian River Inlet and surrounding shoreline on 7/9/2015 (Google Earth).

### 2.1.1 Study Area Generalized Hydrodynamic Forcing Conditions

Tides along the Delaware Atlantic coast are mixed semi-diurnal. Typical tidal cycle durations are approximated as 12.42 hours near the Indian River Inlet (DiCosmo, 2015). Mean National Ocean and Atmospheric Administration (NOAA) predicted tidal range at the US Coast Guard Station near the inlet is 0.80 m with a standard deviation of 0.17 m (NOAA Station 8558690). Mean United States Geological Survey (USGS) measured tidal ranges 13 km into the Indian River Bay are 0.80 m with a standard deviation of 0.13 m (USGS Gage 01484540). Mean USGS measured tidal ranges at the far end of Rehoboth Bay, 10 km from the inlet, are 0.49 m with a standard deviation of 0.09 m (USGS Gage 01484670). Mean NOAA predicted tidal range at Rehoboth beach, 12.5 km up the coast from the inlet which here represents oceanic tidal conditions, is 1.2 m with a standard deviation of 0.3 m (NOAA Station 8557863).

Significant wave heights ( $H_s$ ), determined as the highest third of wave heights, and peak periods ( $T_p$ ) near the inlet were 0.5 m and 9.0 s during 80 days of non-storm conditions (DiCosmo, 2015). Storm average  $H_s$  and  $T_p$ , measured over 20 days near the inlet, were 1.3 m and 7 s respectively (DiCosmo, 2015). Mean significant wave height ( $H_{1/3}$ ), measured approximately 30 km from the Delaware coast, is 1.2 m with an average wave period of 5 s and mean dominant period of 7 s (NOAA Station 4409). Hindcast waves at the US Army Corps of Engineers (USACE) Coastal Ocean Data System (CODS) Wave Information Study (WIS) station 63158, 13 km from the Indian River Inlet in 18 m water depth, are predominantly from the east to southeast with mean significant wave heights ( $H_{mo}$ ) between 0.9 and 1.3 m, as estimated from wave spectral information, and a maximum  $H_{mo}$  of 6 m.

### **2.1.2 Indian River Inlet Area Morphology**

General wave-driven alongshore sediment transport is to the north at the Indian River Inlet as a result of the prevalence of waves from the southeast on the Delaware Atlantic coast. Alongshore sediment transport is approximately proportional to the sine of twice the angle of incidence with a direction determined by the alongshore component of wave direction (Dean and Dalrymple, 2002). Alongshore sediment transport rates on the Delaware Atlantic coast have been estimated using radiation stress-conserving angle calculations on 20 years of hindcast frequency-direction wave spectra data from WISWAVE 2.0 as varying spatially from  $320 \cdot 10^3$  to  $517 \cdot 10^3 \text{ m}^3 \text{ y}^{-1}$  to the north with standard deviations between  $173 \cdot 10^3$  and  $241 \cdot 10^3 \text{ m}^3 \text{ y}^{-1}$  (Puleo, 2010). Yearly net directions were calculated as to the north in all years for all sections. Alongshore sediment transport rate over the 7.6 km south of the Indian River Inlet have been estimated as  $373 \cdot 10^3 \text{ m}^3 \text{ y}^{-1}$  with a standard deviation of  $196 \cdot 10^3 \text{ m}^3 \text{ y}^{-1}$  and

as  $384 \cdot 10^3 \text{ m}^3 \text{ y}^{-1}$  with a standard deviation of  $189 \cdot 10^3 \text{ m}^3 \text{ y}^{-1}$  over the 11.5 km north of the inlet (Puleo, 2010). While a variety of estimates have been made for alongshore sediment transport rate on the Delaware Atlantic Coast, the conclusions may generally be made that net direction has been to the north and inter-annual variability is large, with standard deviations approaching or exceeding half of the mean. Accretion has been observed at the southern jetty of the Indian River Inlet with erosion to the north of the inlet, consistent with littoral drift to the north.

The shoreline on the north side of the Indian River Inlet has suffered severe and chronic downdrift erosion following the model of a near and far arc (Bruun, 1995; Galgano, 2009). Eight beach nourishment projects, between 1957 and 1990, deposited approximately  $2,800,000 \text{ m}^3$  of sediment on the downdrift beach in response to the severe shoreline erosion (Keshtpoor et al., 2013). A mechanical bypassing system was installed at the Indian River Inlet in 1990 to bring sediment to the downdrift side of the inlet and limit shoreline change, protecting the nearby road. Coastal Highway, Delaware Route 1 is both the main route of transportation along the Delaware Atlantic Coast and at the nearest approximately 100 m from the shoreline. The sediment bypassing system transported approximately  $1,314,000 \text{ m}^3$  to the downdrift side of the inlet between 1990 and 2010. Empirical Orthogonal Function (EOF) analysis of beach profile data has indicated that downdrift erosion was mitigated through bypassing between 1991 and 2000 with an increase in downdrift erosion between 2000 and 2007 (Keshtpoor et al., 2013). DE Route 1 was blocked by Hurricane Sandy in 2012, closing the only evacuation route in the area. Downdrift erosion has been a persistent problem at the Indian River Inlet and has required continual maintenance.

## **2.2 Previous Hydrodynamic Studies near the Indian River Inlet**

The history of erosion around the inlet and previously determined local data motivate the study of current patterns and hydrodynamics to the north of the Indian River Inlet. NearCoM simulations and Nortek Aquadopp Acoustic Doppler Currents Profiler (ADCP) measurements suggest complex hydrodynamics to the north of the inlet. NearCoM simulations of the area surrounding the Indian River Inlet predicted a gradient in significant wave height, mobile areas of flow divergence, and velocities opposing the direction of alongshore sediment transport in the area north of the inlet. ADCP measured hydrodynamic data north of the inlet imply similar flow features. Both Eulerian measurements and depth averaged model simulation results indicate a substantial spatial variation in the flow field to the north of the inlet.

### **2.2.1 NearCoM Simulations of Hydrodynamics to the North of the Indian River Inlet**

Depth-averaged wave and tide driven hydrodynamics were simulated with NearCoM as part of a previous Delaware Department of Natural Resources and Environmental Control (DNREC) supported project. Simulated wave and tide driven velocities and wave information between 10 km south of the Indian River Inlet and 17 km north of Cape May indicate that within 1000 m north of the Indian River Inlet a pressure gradient and wave focal point drive inlet-directed flow (Keshtpoor et al., 2015). Grid spacing in the NearCoM simulation varied between 20 m in the Indian River Inlet and 300 m at the offshore boundary and mouth of the Delaware Bay. Previous model forcing consisted of the six leading ADCIRC tidal constituents and significant wave height, period, and direction for 16 days. Wave forcing conditions of offshore significant wave height ( $H_s$ ), wave period, and wave direction were between the six conditions which accounted for more than 5% of the data at NOAA NDBC

buoy 44009 between 1994 and 1998 (Table 1). Validation was addressed through the Comparison of NearCoM simulated results and bottom mounted ADCP measurements near the inlet. Simulated hydrodynamics achieved Willmott skill scores of 0.97 for water level, 0.68 for peak ebb velocities, 0.78 for peak flood velocities, 0.74 for significant wave height, and 0.73 for wave direction near the jetty tip. Hydrodynamic predictions from the NearCoM modelling effort of Keshtpoor et al. (2015) indicated an alongshore wave height gradient, driving flows to the south in offshore significant wave heights ( $H_s$ ) of 1.4 m during the falling tide. NearCoM simulations also predicted a flow divergence point approximately 300 m north of the inlet with flows to the south within a larger scale flow to the north, coinciding with maximum predicted flood velocities (Keshtpoor et al., 2015).

Table 1: Wave characteristics for NearCoM simulations of hydrodynamics near the Indian River Inlet.

Wave Case	$H_s$ (m)	$T$ (s)	$\theta$ ( $^\circ$ )	Occurrence (%)
1	0.68	8.79	120.46	13.26
2	0.72	7.09	149.25	9.83
3	0.71	9.69	91.32	9.64
4	1.42	9.53	89.98	8.51
5	1.41	8.05	150.55	7.69
6	1.40	9.37	119.95	5.87

### 2.2.2 Eulerian Measurements to the North of the Indian River Inlet

Wave and current measurements from bottom mounted ADCP arrays also indicate a potential circulation cell and divergence point in the vicinity of the north jetty at the Indian River Inlet (DiCosmo, 2015). Wave and current ADCP data were collected from two cross-shore and two alongshore arrays within 1,400 m north of the inlet as part of a previous DNREC supported project. Sensor deployments were

separated by array and each had a duration of approximately one month. Analysis of the cross-shore ADCP arrays across deployments revealed that currents within 100 m north of the inlet generally had southerly alongshore components and may have formed a circulation cell which was dominated by flow into and out of the inlet (DiCosmo, 2015). Alongshore ADCP array velocities indicate a mobile divergence point north of the inlet. The alongshore ADCP array also measured smaller velocities more than 100 m from the inlet ADCP data suggesting a complicated flow field with substantial spatial variations.

Flow velocities within 100 m of the Indian River Inlet were investigated with two cross-shore arrays of ADCPs, each deployed for one month in water depths between 5.1 to 8.8 m. All cross-shore ADCP array positions were located outside of the surf zone. Vertical profiles of ADCP flow velocities were depth averaged, ensemble averaged according to location within the approximately 12.5 hour tidal cycle, and phase averaged across the approximately 2 hour tidal phase during non-storm conditions to determine typical vectors. The alongshore component of depth, ensemble, and phase averaged velocities were to the south for all cross-shore array ADCPs landward of the jetty tip, regardless of tidal phase. The ADCP within 100 m of the inlet and seaward of the jetty tip measured alongshore components of typical velocities generally to the south with a typical velocity to the north west from approximately 2 to 4 hours after low tide. Directional variability in depth, ensemble, and phase averaged velocity with tidal phase was greatest for the most seaward cross-shore ADCP. The two tidal phases with the greatest averaged velocities in the cross-shore array were before and after high tide, regardless of position. The ADCP velocity

data collected from cross-shore arrays may suggest that the exchange of water into and out of the inlet induced the typical velocity variability within 100 m north of the inlet.

Flow velocities within 1,400 m north of the inlet were investigated with two alongshore arrays of ADCPs, each deployed for one month in 3.3 to 4.5 m deep water. All ADCP locations were outside of the surf zone during non-storm conditions. Non-storm vertical profiles of velocity were depth and ensemble averaged by the procedure used for the data from the cross-shore arrays. The first alongshore array of ADCPs, sites A3 to D3, measured the smallest velocities. In the second alongshore array of ADCPs, sites A4 to D4, velocities were smaller than in any of the cross-shore arrays but larger than in the first alongshore array. The variation in mean velocity magnitude in the alongshore demonstrates that flow velocities were fastest within 100 m north of the inlet but did not decrease with northing. Temporal location of depth, ensemble, and phase averaged velocity maxima across the alongshore arrays of ADCPs do not follow a consistent trend with northing. Averaged velocity maxima in the alongshore arrays varied in tidal phase across the arrays. Depth, ensemble, and tidal phase averaged velocity and flow direction variation between tidal phases was not consistent between sites within the alongshore arrays of ADCPs. While velocities were at a maximum within 100 m of the inlet during the phase before high tide, flow directions farther away varied from southerly to northwesterly across the alongshore arrays. The averaged velocities from the alongshore ADCP arrays also indicate a possible mobile divergence point (DiCosmo, 2015).

Eulerian hydrodynamic measurements within 1,400 m north of the Indian River Inlet indicate a complex current pattern in the vicinity of the inlet. The presence of net southerly velocities, a circulation cell, and a divergence point within the flow

field to the north of the inlet could all be supported by ADCP data. The net alongshore current which drives littoral transport to the north would produce a strong horizontal shear with an area of net flows to the south. The complexities in the flow field which Eulerian hydrodynamic measurements and NearCoM simulations imply may suggest that a finer spatial resolution in hydrodynamic measurements could improve predictions of current patterns to the north of the Indian River Inlet.

### **2.3 Project Objectives and Overview**

The area downdrift of the Indian River Inlet has experienced serious and chronic erosion. The interruption of the littoral drift along the generally continuous and sandy Delaware shoreline with a predominant alongshore component of wave direction from the south has induced a downdrift arc of erosion north of the inlet. To maintain leeside beach width a sediment bypassing system deposits sediment north of the inlet. The closure of a major evacuation in the area by overwash during Hurricane Sandy highlights the importance of downdrift erosion at the Indian River Inlet. Eulerian current and wave measurements and NearCoM model simulations with Eulerian validations indicate a complex flow field near the inlet. Predictions of current patterns and forcing conditions north of the inlet are important because the bypassing system deposits sediment in that area. The spatial variability of the flow field implies the benefit of spatially dense hydrodynamic measurements such as Lagrangian drifter tracks towards improving the validation of predictions at the inlet.

The aim of this project was to study the current patterns within approximately 1200 m north of the Indian River Inlet through Lagrangian drifter measurements and Delft3D simulations. Lagrangian drifters have been deployed in four field tests north of the inlet over the entire tidal cycle (Figure 4). Delft3D simulations of the area have

been validated with previously determined Eulerian measurements and compared to drifter tracks. Delft3D simulations have been extended with additional passive tracers to infer circulation patterns under different tidal and wave forcing conditions.



Figure 4: Lagrangian drifters following currents to the north of the Indian River Inlet in Delaware.

## **Chapter 3**

### **INSTRUMENTATION**

#### **3.1 Lagrangian Drifters**

Tracking objects entrained in a current has a long history of use in flow studies, dating as far back as 1553 (Monahan and Monahan, 1973). Neutrally buoyant drifters obstruct flow at a certain depth and are thus advected by a current. Drifters are assumed to act as passive tracers and have minimal impact on the flow which they measure at a certain scale. Estimates of the current in which drifters are entrained represent an average over a volume related to the volume occupied by the drifter. Vertical positions of flow velocity estimates are specified by the water depth of the flow obstruction. Processes studied dictate drifter size and depth dimensions. In this experiment, a drifter was designed to study flows not far from the surf zone based on the GPS-tracked surf zone drifters of Schmidt et al. (2003). Drifter design was more closely related to the designs presented in MacMahan et al. (2009), Austin et al. (2012), and Scott et al. (2016). Drifter tracks display the fate of a fluid parcel in the study area and may be time-differenced to obtain velocity information. GPS-tracked drifters enable the determination of position data at a frequency of 1 HZ, providing spatially dense velocity estimates and are thus well suited for studying currents with large horizontal flow variability.

### 3.1.1 Lagrangian Drifter Design

A suite of current-following, GPS-tracked, Lagrangian drifters were designed and constructed to quantify spatial variations in the current patterns to the north of the Indian River Inlet. Nearshore drifters are typically designed to resist impact, wind slippage, and vertical motion with a relatively shallow draft; as a result, they often have similar designs (Schmidt et al., 2003; Spydell et al., 2007; MacMahan et al., 2009; Austin et al., 2012; Scott et al., 2016). Schmidt et al. (2003) introduced a design for GPS-tracked nearshore drifters which has influenced many subsequent drifter designs. Drifter design was altered in MacMahan et al. (2009) with the addition of vertical fins, and modulated to reduce cost in Austin et al. (2012) and Scott et al. (2016). The primary contribution of the design developed in this project is the robust watertight electronics case equipped with a bulkhead, which substantially reduces the risk of flooding.

Drifter design consisted of a cylindrical body with fins and a damping plate supporting an IP68 waterproof electronics box and mast with a GPS antenna (Figure 5). Overall drifter height was approximately 1.4 m with an approximate mass of 8.1 kg (80 N). A 0.765 m mast of schedule 40 1- $\frac{3}{4}$ " PVC pipe elevated the GPS antenna above the water. GPS antennas were made water resistant with casting resin and molds. Masts were supported by drifter bodies composed of 0.6 m of schedule 40 4" PVC pipe, inside of which a closed cell foam cylinder of similar dimensions improved buoyancy. Drifters were equipped with three equally spaced fins of dimensions 0.3 by 0.08 by 0.006 m to increase submerged surface area. Concurrent dye and drifter releases have indicated the benefits of drifter fins (MacMahan et al. 2009). Fins were positioned normal to the PVC drifter body, with angles ensured by use of polycarbonate mounts fabricated by CHPT Manufacturing Inc. At the base of the

drifter a 0.025 m<sup>2</sup> wooden disk damped vertical motion and a 0.018 m<sup>2</sup> steel ballast plate lowered the center of gravity. Components of the drifter were bound by compression with a ¼” threaded steel rod passing through the entire assembly. The drifter was compressed between a steel antenna ground plane welded to the top of the rod and a nylon-insert nut fastened at the base of the rod.

Buoyancy and stability testing and calculations were conducted with stationary non-saline water assuming a vertically upright drifter. Stability calculations were one dimensional and thus unable to account for the asymmetry of displaced volume. While all other elements of the drifter were designed symmetrically, the brackets on the electronics box necessitated a vertical placement with both ends on the 4” PVC drifter body. The electronics box contributed approximately 22% of the buoyant force acting at a distance estimated as 0.115 m from the central vertical axis. The resulting asymmetry necessitated an external foam ring. A 0.42 x 0.09 x 0.05 m block of closed cell foam was positioned level with the electronics box and bent into a ‘U-shape’ spanning the exposed perimeter to balance the drifter.

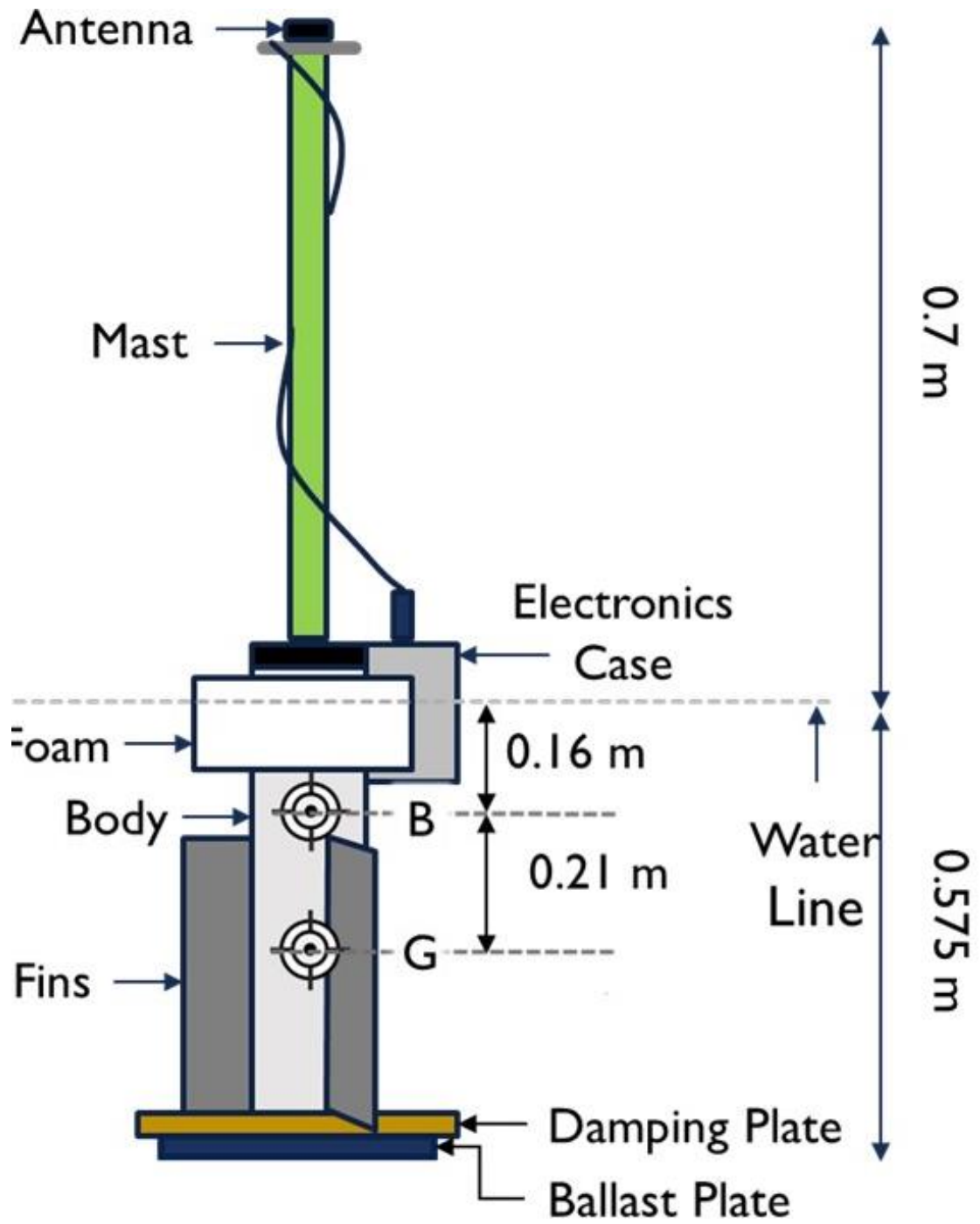


Figure 5: Schematic of drifter components indicating vertical dimensions and the location of the computed water line, estimated center of buoyancy (B), and estimated center of gravity (G).

Buoyancy calculations initially assumed the entire mast would remain above the free surface, which would correspond to a 0.6 m draft. The related buoyant force may be calculated as 98 N, on the assumption of a fully submerged drifter body. Preliminary testing of submerged volume indicated an overestimation of displaced volume on the order of  $0.5 \times 10^{-3} \text{ m}^3$ , which reduced the calculated buoyant force to 91 N. The corresponding force difference may be calculated as 11 N after applying the volume correction. Assuming a level drifter, the height of the displaced volume corresponding to the difference between the preliminary buoyant force and weight may be estimated as 0.025 m from the cross-sectional area of three components: the drifter body, electronics box, and external foam ring. Subtracting the height calculated from the extraneous buoyant force from the initially assumed draft yields a draft of 0.575 m. The center of gravity may be calculated as 0.37 m beneath the water line. The center of buoyancy may be calculated with the metacentric height equation as 0.16 m beneath the water line. Center of buoyancy and gravity calculations included masses accounting for 95% of the total. Testing additionally confirmed drifters to be buoyant and stable.

### **3.1.2 Wind Slippage**

An important element of drifter design is the minimization of wind slippage, defined here as a wind induced difference between the velocity of the drifter and that of the surrounding flow. Severe wind slippage effects reduce the certainty that differenced drifter positions accurately reflect general current patterns. Drifter studies often provide some estimate of the magnitude of the wind slippage effect of a particular design (Murray, 1975; Schmidt et al., 2003; MacMahan et al., 2009; Spydell et al., 2015; Scott et al., 2016). As the scope of this study did not involve wind testing,

the effects of wind slippage on drifter motion were approximated through comparison with a previously determined curve (Figure 6) as in MacMahan et al. (2009) and Scott et al. (2016).

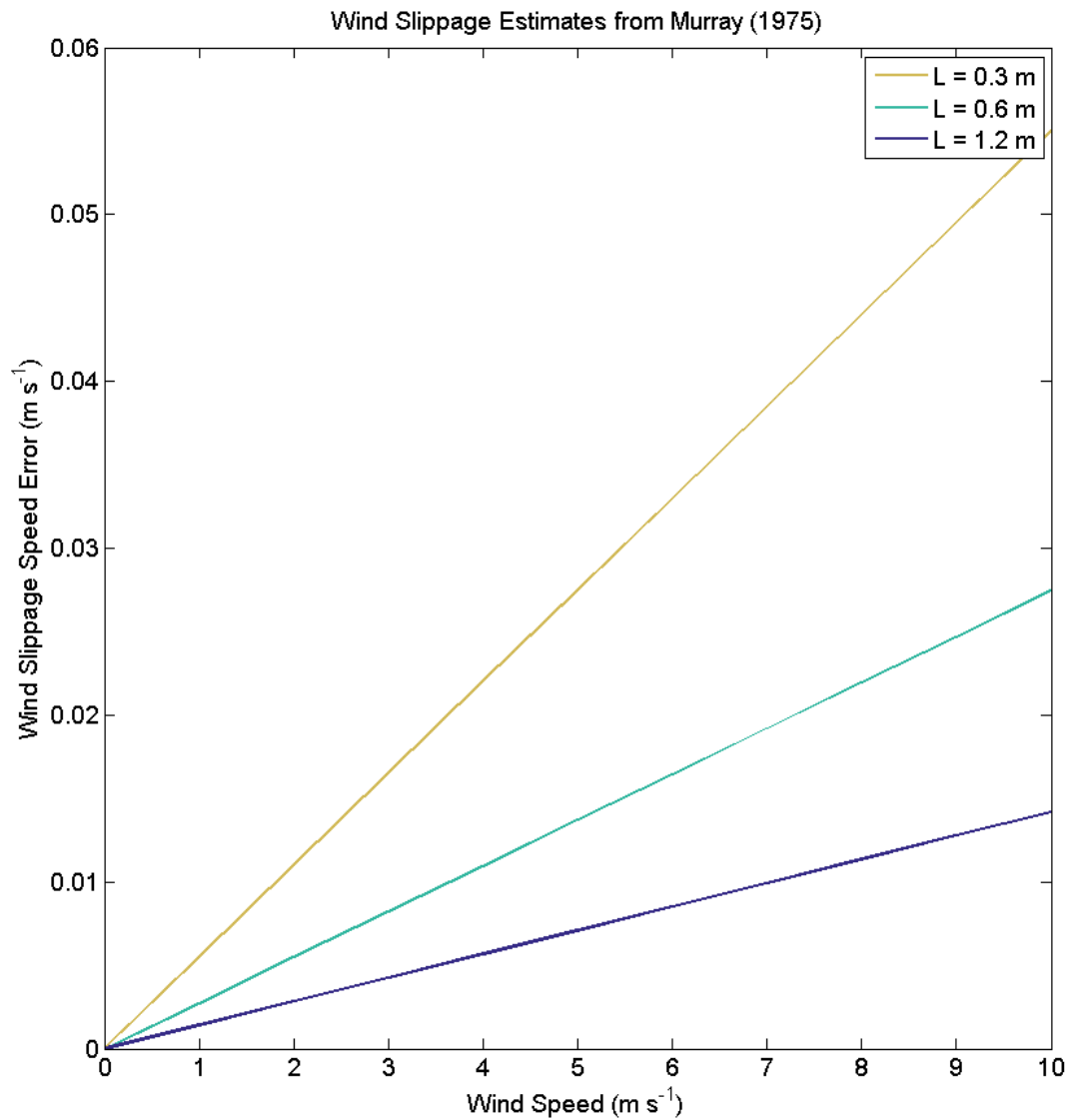


Figure 6: Wind slippage induced velocity as a function of windspeed for drogues with rectangular cross-sections and subaerial cylindrical poles of approximate projected area  $0.045 \text{ m}^2$  (Murray, 1975). Lines for various typical drogue dimensions  $L$  are presented.

Using the data presented in Murray 1975, the drifter submerged projected area estimate of  $0.078 \text{ m}^2$  corresponds most nearly to the curve provided for a drogue width of 0.3 m (projected submerged area estimate of  $0.09 \text{ m}^2$ ). Maximum wind slippage velocity for wind velocities up to  $6 \text{ m s}^{-1}$  may be estimated as less than  $0.07 \text{ m s}^{-1}$  (Figure 7; Murray, 1975). Concurrent velocities from drifters, dye, and filled balloons indicated that the curves of Murray, (1975) over-estimated wind slippage effects on the drifter design of Schmidt et al., (2003). Error is also introduced by the rectification of oscillatory wave motions, in which drifters behave as a damped, nonlinear oscillator responding to three factors: buoyancy, flow drag forces, and pressure gradients (Davis, 1985). For similar designs in waves of 0.3 m height, 10 s period, 1 m depth, and oscillatory velocity of  $0.35 \text{ m s}^{-1}$  wave rectification velocities were less than  $0.01 \text{ m s}^{-1}$  (Schmidt et al., 2003).

### **3.1.2.1 Wind Slippage Resistant Drifter**

An alternate wind slippage resistant drifter was designed to address the impacts of wind slippage on recorded tracks in a more localized approach than the plot from Murray (1975). The goal in designing the wind slippage resistant drifter was to increase the ratio of submerged surface area to exposed surface area to qualitatively estimate the impact of wind slippage on the drifters based on Schmidt et al. (2003). The wind slippage resistant drifter was deployed concurrently with the drifter modified from Schmidt et al. (2003). The wind slippage resistant drifter consisted of a schedule 40 1" PVC body with eight 0.35 m arms on two levels supporting four sails and a mast with an antenna and circular steel ground plane (Figure 7). PVC drifter arms were attached by 'five-way cross' PVC connectors with a 1 m schedule 40 1" PVC stem connecting the two sets of four arms. Sails were constructed from rip-stop

nylon. Four 5” by 9” polyethylene oval floats were fixed to each arm of the upper cross to provide buoyancy. The wind slippage resistant drifter had a draft of 1.1 m, a mast height of 0.7, and a combined sail width of 0.7 m. Sail dimensions of 1.1 by 0.7 m correspond to a typical drogue dimension  $L$  somewhere between the two dimensions. Using the plot from Murray (1975) wind slippage velocity of the new drifter may be estimated as approximately  $0.035 \text{ m s}^{-1}$  for wind velocities of  $6 \text{ m s}^{-1}$  (Figure 6).



Figure 7: Wind slippage resistant drifter designed and constructed to investigate the impact of wind slippage on tracks from the primary drifters.

### 3.1.3 Depth-Dependent Wave Impacts on Drifter Velocities

In this study, the general hydrodynamics near the Indian River Inlet are investigated through a depth-independent approach. Previous flow velocity measurements in the area indicate that, below 1 m depth, standard deviations in vertical profiles of velocity are generally small, on the order of between  $0.01 \text{ m s}^{-1}$  and  $0.05 \text{ m s}^{-1}$  (DiCosmo, 2015). In addition to the small velocity variations with depth, the scope of this project, availability of data, and size of the domain justify the use of 2D model simulations to extend results. Velocities induced by non-linear wave processes are depth-dependent and thereby potential sources of error between drifter measurements and general depth-averaged hydrodynamic conditions. Drogue depths were limited to approximately 0.6 m to maximize the number of drifters by facilitating deployment and retrieval. The shallow drogue depth had the potential to exacerbate the impact of Stokes drift on drifter velocities. To estimate the magnitude of Stokes drift during the field experiments, a simplified equation from Chang et al. (1969) was applied to extremes of typical data. The equation for the mass transport velocity ( $\bar{U}$ ) may expressed as,

$$\bar{U} = \frac{a^2 \omega k \cosh 2k(z - h)}{2 \sinh^2 kh} + C, \quad (1)$$

where  $a$  represents amplitude,  $k$  is wave number,  $\omega$  is the angular frequency,  $h$  is the water depth,  $z$  is a variable elevation in the water column, and  $C$  is an arbitrary constant (Chang et al., 1969). Setting net horizontal mass transport to zero,  $C$  may be determined to be,

$$C = -\left(\frac{a^2 \omega}{2h}\right) \coth kh \quad (2)$$

Errors noted in this estimation of mass transport velocity are generally lower in the water column (Chang et al., 1969). As the approximations were all at elevations in the top 5<sup>th</sup> of the water column, the presented equation was taken as an acceptable estimate of Stokes drift.

Wave data were obtained from the US Army Corps of Engineers station DWG-BB03 in a nominal water depth of 11 m offshore of Bethany Beach and approximately 8 km from the Indian River Inlet. During the drifter deployment on 05/26/2016 the maximum hourly  $H_{mo}$  recorded at the DWG-BB03 gauge was 0.503 m with a corresponding period of 8.2 s. Minimum water depth, determined as the model bathymetry value for recorded drifter positions, was 2.5 m. The resulting Stokes drift velocity estimates may be computed as  $0.0062 \text{ m s}^{-1}$ . Alternatively, using the minimum period recorded during the 05/26/2016 drifter deployment, 7.9 s, with a corresponding  $H_{mo}$  of 0.49 m, the Stokes drift velocity estimate becomes  $0.0065 \text{ m s}^{-1}$ . The average drifter speeds were  $0.05 \text{ m s}^{-1}$  along an easting axis and  $0.11 \text{ m s}^{-1}$  along a northing axis. Stokes drift contributions may be estimated as a maximum of 13% in the easting and 6% in the northing. During the 10/20/2016 drifter deployment the maximum  $H_{mo}$  was 0.53 m with a corresponding period of 12 s and a minimum depth estimate of 3.3 m, yielding an estimated Stokes drift velocity of  $0.0028 \text{ m s}^{-1}$ . During the 10/20/16 field test the average drifter velocity in the study area was  $0.095 \text{ m s}^{-1}$  along a northing axis and  $0.15 \text{ m s}^{-1}$  along an easting axis. Maximum Stokes drift contributions may be estimated as a maximum of 3% of the northing and 2% of the easting velocities. During the 05/30/2017 drifter deployment the maximum  $H_{m0}$  was 1.02 m with a corresponding period of 8.6 s and a minimum depth estimate greater than 5 m, yielding an estimated Stokes drift velocity of  $0.0164 \text{ m s}^{-1}$ . Stokes drift

estimates are small, thus indicating depth-dependent net wave velocities had a small impact on observed drifter motion.

### **3.2 Drifter Tracking System**

Lagrangian drifter studies rely on tracking objects entrained in the current of interest. Flow velocity estimation capabilities relate closely to position accuracy and sampling frequency. While a variety of techniques have been used to track Lagrangian drifters, the advent of publicly available satellite positioning at sub 100 m accuracy introduced GPS as one of the most common positioning techniques in Lagrangian drifter studies (Johnson et al., 2003). Drifter design involved a GPS receiver connected to an external antenna recording satellite information on a logger, both contained within an electronics box. The drifter positioning system was developed to determine accurate velocities at relatively accurate positions with a low-cost system. Raw L1 carrier-phase data were recorded by each drifter and by a nearby base station to determine post-processed position information.

### **3.2.1 Drifter GPS System**

The GPS tracking system on each drifter consisted of a GPS receiver which obtained satellite signals from an external antenna and logged raw L1 GPS carrier-phase information on an internal logger. The Novatel OEMStar Single-Frequency, Multi-Constellation, GNSS Receiver was selected to determine satellite information based on cost and power consumption considerations. OEMStar power consumption was listed as typically 600 mW, which allowed more flexibility in battery choice. GPS receivers were powered by Trakpower 2 cell Lithium Iron Phosphate (LiFe, LiFePO<sub>4</sub>) 1900 mAh, 6.6 volt batteries, wired to the receiver through an ST low-dropout 5V voltage regulator to avoid shocking the receiver while ensuring a supply exceeding the minimum voltage required. Carrier-phase data were recorded at 1 Hz onto an SD card in a Photologic RX Dual Channel RS232 Serial Recorder, via physical connection to the receiver. Data loggers were powered by 9 volt batteries. Satellite signals were received by HQRP patch antennas on the top of drifter mast. Relative positions have been shown to be acceptable for low cost antennas when post-processed with base station corrections (Schmidt et al. 2003). A concurrently recording Leica Viva GS15 GNSS antenna provided high accuracy raw L1 GPS carrier-phase information for post-processing corrections within Novatel Waypoint GrafNav software. GPS receivers, data loggers, and batteries were contained within waterproof electronics boxes, attached to each drifter (Figure 8). The GPS tracking system cost for each drifter was approximately \$400. Each electronics box contained an IP68 waterproof bulkhead for the antenna cable. Cost requirements and signal wiring limitations necessitated a transition from MCX cable leaving the antenna to unshielded wire to and from the bulkhead. Preliminary testing indicated that neither shielding nor braiding the wire sections leaving the bulkhead had a substantial impact.

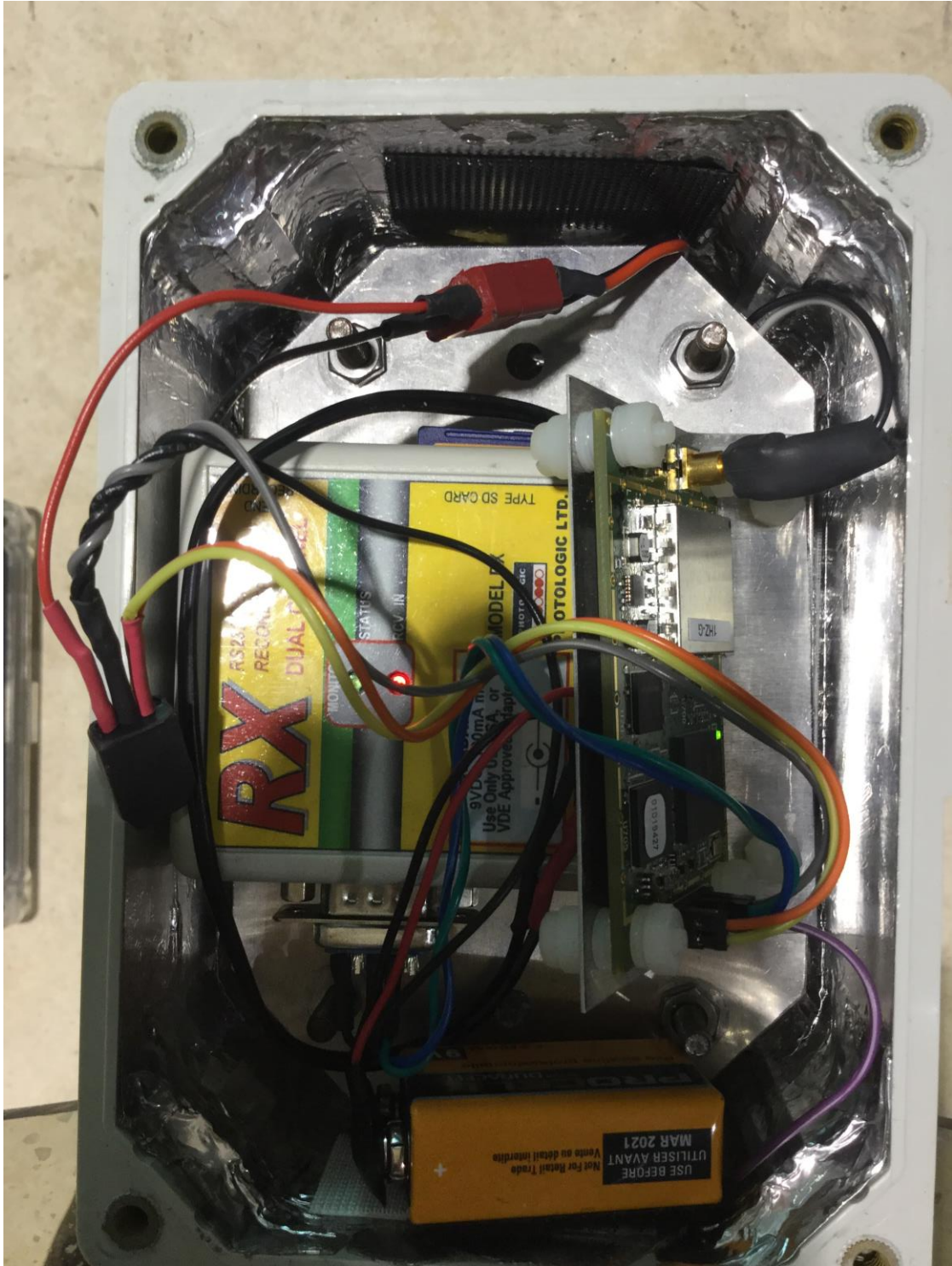


Figure 8: Drifter IP68 waterproof electronics box containing GPS system (i.e. GPS receiver, antenna cable, and data logger).

### 3.2.2 GPS System Post-Processed Accuracy

Given the nature of GPS error, the determination of GPS accuracy contains an important distinction. Without considering the individual processes which cause GPS inaccuracies, error may be divided into two categories: absolute and relative. Absolute error is the difference between a measured position and the corresponding true position. Relative error is the difference between a measured position and the corresponding true position relative to the absolute error of the previous data point. Relative error provides a measure of the variation in absolute error over a time step, which is related to velocity estimation accuracy. While absolute accuracy is important, the interest in this and a number of other studies is generally in relative accuracy. Accurate velocity estimates, which correspond to small relative errors, were given a higher priority than accurate positions, which are related to small absolute errors. The post-processing software provides an estimate of absolute position accuracy, which for the drifter GPS system was on the order of 4 m after applying base station corrections. Position errors on the order of 4 m were deemed acceptable. An adequate estimate of relative position accuracy was not provided in the post-processing software and thus needed to be determined by alternate means.

A test was devised to determine an estimate of relative position accuracy in which a Leica Viva GS15 GNSS antenna and the drifter antenna were both fixed atop an approximately 2 m tall survey cart. On 10/13/15, the survey cart was pushed along an arbitrary path in an open space with minimal horizon obstruction angles (Figure 9). A steel plate separated the antennas so that the relative errors between the two antennas could be computed by comparing the difference between positions of the two antennas as functions of time. Comparing data after a 14 second running average yields an  $r^2$  statistic of 0.94 and a root mean square error (rmse) of  $0.080 \text{ m s}^{-1}$ . Before

applying a running average, the comparison yields an  $r^2$  of 0.62 and an rmse of 0.22 m  $s^{-1}$  (Figure 10). Measuring longer tracks with shallower turns, like those collected *in situ*, might correspond to a higher maximum  $r^2$  at a longer smoothing window size. Typical absolute and relative error magnitudes of the drifter GPS System were determined to be adequate.

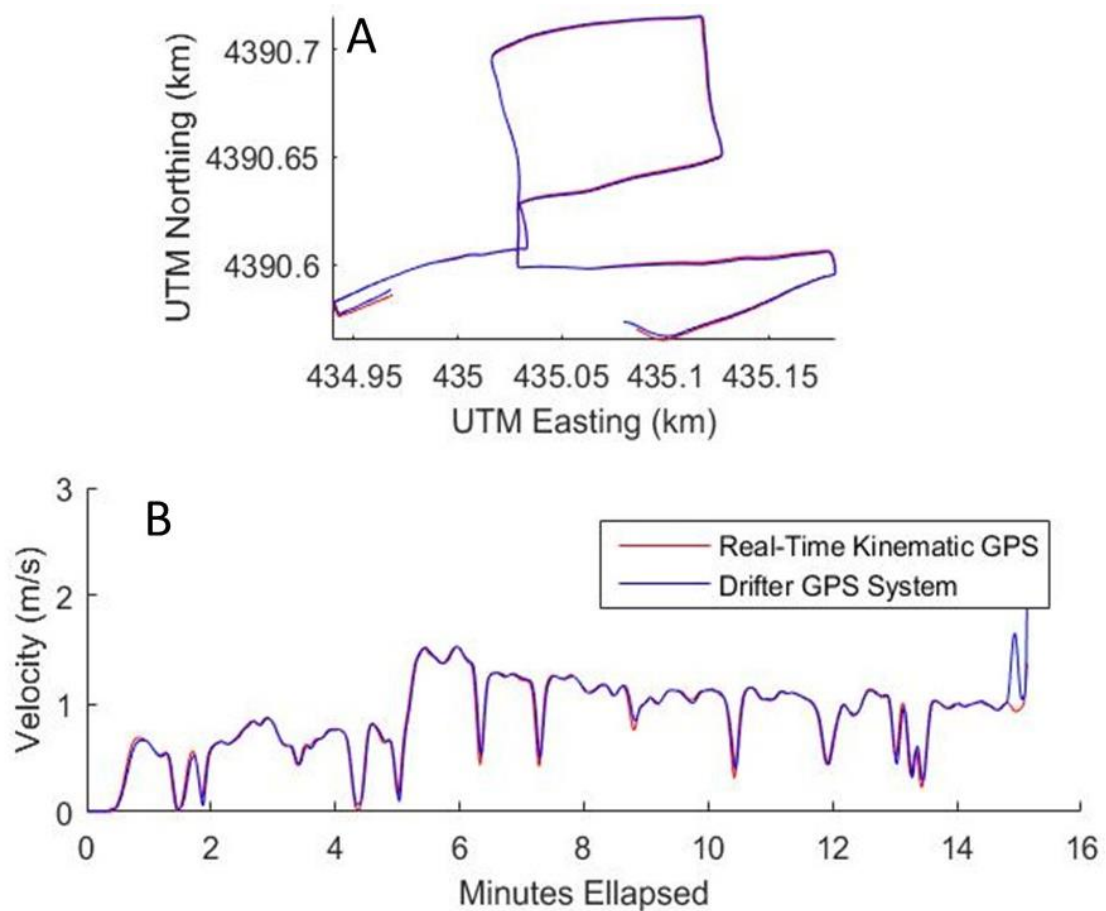


Figure 9: Results from the 10/13/15 accuracy test A) Leica GS15 GNSS data with RTK corrections and the drifter GPS system as paths followed by the cart. B) Cart velocity as determined by time differencing running averaged antenna positions.

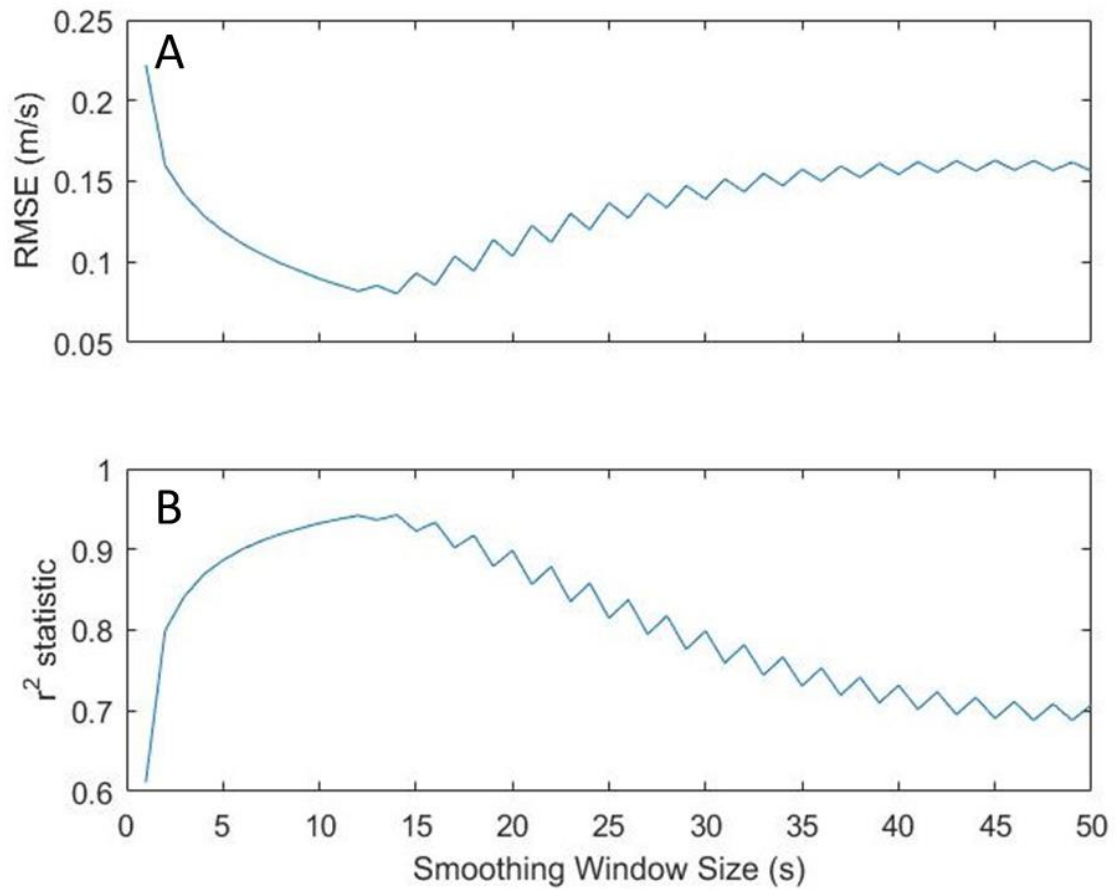


Figure 10: (A) plot of drifter GPS system RMSE in  $\text{m s}^{-1}$  as a function of running average window size in s. (B) plot of  $r^2$  between drifter GPS system and RTK corrected Leica GS15 GNSS as a function of running average window size in s.

### 3.3 Drifter Deployment Strategy

The procedure for data collection consisted of the repeated release and collection of drifters by boat. The research vessel transported drifters to release points and retrieved them when deemed appropriate (Figure 11). Drifters were grouped into three clusters with five drifters in each group. Cluster placement within a specific release varied in either cross-shore or alongshore position. Release locations were entirely to the north of the inlet and seaward of the surf zone. A specific placement scheme was not adhered to, improving study feasibility and permitting the flexibility to adjust based on previous results. Local and design constraints made the retrieval of beached drifters difficult, leading to a preference for locations of adequate depth for the research vessel. Drifters were collected when they exited the study area or approached less accessible areas (i.e. shallow water or the inlet channel).



Figure 11: Drifters as transported by research vessel within the Indian River Inlet. The DE Route 1 bridge at the Indian River Inlet visible in background.

## Chapter 4

### DRIFTER FIELD DATA

Drifter data collection occurred over four full scale field experiments between 11/24/15 and 05/30/17 with a combined duration spanning the entire semi-diurnal tidal cycle. The semi-diurnal tidal cycle in the study area is here defined as between low tides within the inlet. Each semi-diurnal tidal cycle is considered to consist of twelve tidal phases which are expressed as fractions of  $\pi$ , such that low tide may be expressed as 0 and  $2\pi$ , corresponding to a negative cosine curve. Wind speed and significant wave height varied by more than  $5 \text{ m s}^{-1}$  and 0.5 m between the four field experiments. Tidal range varied by more than two standard deviations. Drifters were observed traveling north and south, entering the inlet channel, and being advected offshore in the ebb jet (Figure 12b). Drifter data were typically plotted over bathymetry taken from the model input described in chapter 5. Drifter data is presented after applying a running average of 120 s window size and separation into twelve tidal phases (Figure 12a; Figure 12b). Tidal phase separation of drifter tracks indicates that the flow field to the north of the inlet varies substantially with tidal phase, but also additional factors which are not well addressed by data collected. The lack of spatial overlap in tidal phases between conditions for much of the study area limits the ability to study current feature variation with characteristics other than tidal phase.

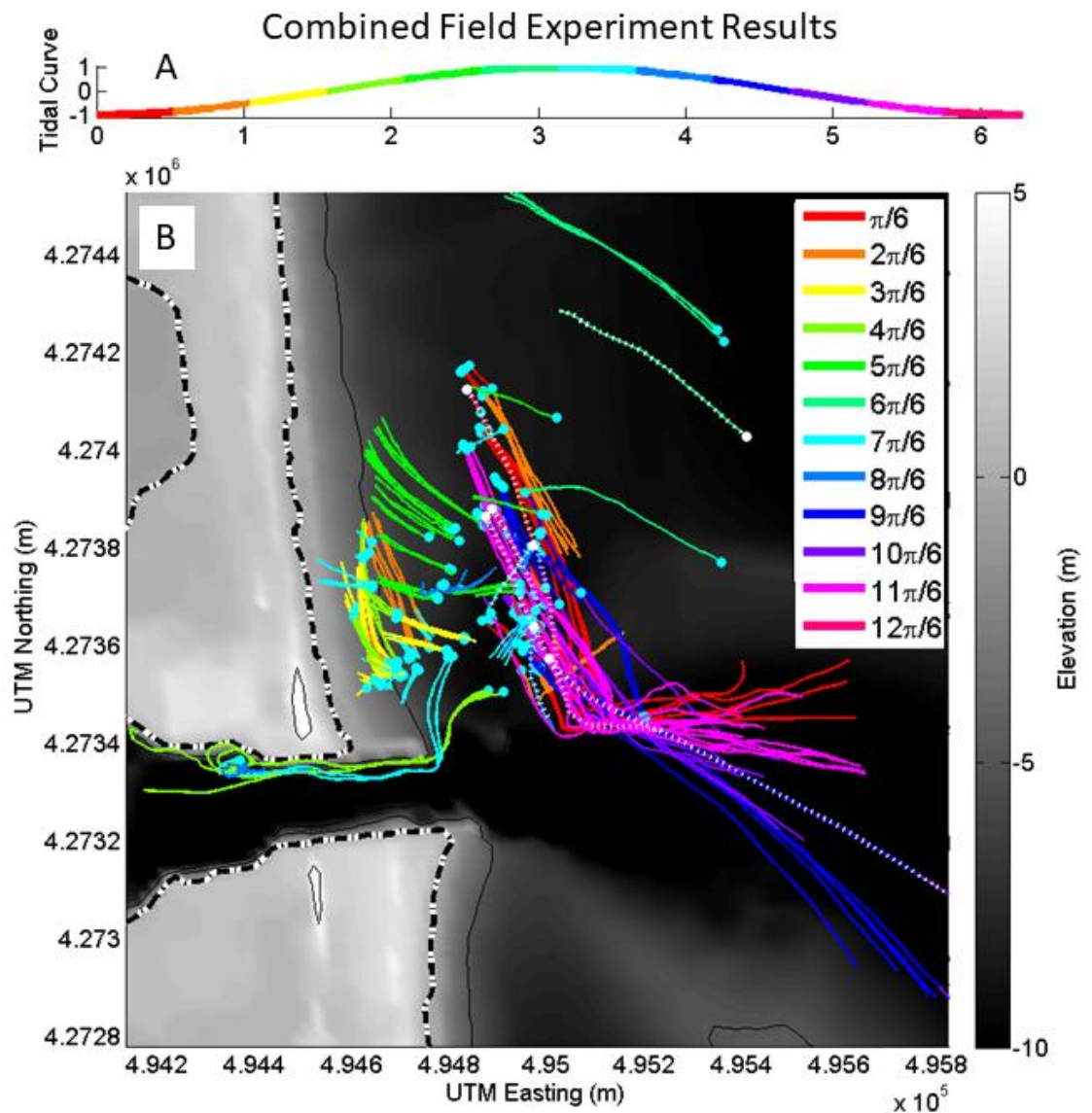


Figure 12: A) Idealized tidal curve divided into twelve phases. Color indicates tidal phase. B) Drifter tracks from all four field experiments plotted over bathymetry data. Drifter position time series have been filtered with a running average using a window size of 120 s. Line color indicates drifter track tidal phase. Release points are indicated in cyan. Dashed white overlays on plotted drifter tracks indicate wind slippage resistant drifter paths. A line at zero m in Mean Sea-Level (MSL) coordinates is plotted with increased thickness and varying black and white coloring.

#### 4.1 Field Experiment I

The first full scale drifter field experiment was conducted on 05/26/16 between 7:30 AM and 1:30 PM Eastern Daylight Time (EDT). Collected semidiurnal tidal phase information varied between 1.5 hours after low tide to 1.5 hours after high tide. In the first experiment drifters were generally released in the rising tide. Tidal range during the first field experiment was predicted to be 0.62 m within the inlet and 0.90 m at Rehoboth Beach, which is 12.5 km north of the Indian River Inlet, also on the Delaware Atlantic coast, and may be used to represent an oceanic tide. Tidal range in the first experiment was one standard deviation below the mean. Wind speeds were between  $0.5 \text{ m s}^{-1}$  and  $4 \text{ m s}^{-1}$  out of the north northwest and the south (Figure 14). Significant wave heights were between approximately 0.4 m and 0.5 m (Figure 15). Wave direction was out of the southeast to east with periods between 8 and 10 s.

Drifter path data display drifters traveling generally to the north in the first field experiment with varying degrees of onshore motion (Figure 13). In the  $2\pi/6$  and early  $3\pi/6$  tidal phases drifters more than 200 m north of the inlet traveled north northwest, with drifters closer than 200 m from the inlet traveling in varied directions with sharp turns. Drifters later in the  $3\pi/6$  phase traveled north northwest approaching a heading of due north more than 300 m from the inlet. In the  $4\pi/6$  tidal phase drifters traveled northwest, with drifters more than 50 m east of the north jetty tip maintaining a relatively constant heading and drifters fewer than 50 m east of the jetty tip turning to the north. Wind action could have pushed drifters to the northwest due to the wind directions between  $140^\circ$  and  $160^\circ$  in the  $4\pi/6$  phase, however, as velocities were between  $2 \text{ m s}^{-1}$  and  $3.5 \text{ m s}^{-1}$  wind slippage was likely small. The alongshore component of drifter tracks during the entire field experiment was to the north for all drifters more than 140 m north of the inlet. The single drifter within 140 m north of

the north jetty tip traveled west southwest. Although the drifter within 140 m of the north jetty traveled slowly, wind speeds were between  $1 \text{ m s}^{-1}$  and  $2 \text{ m s}^{-1}$  from the south which suggests that the measured flow direction in that area is accurate. Results from the first field experiment indicate a flow divergence point fewer than 150 m north of the inlet in slow winds, small to average waves, and a tidal range one standard deviation smaller than the mean.

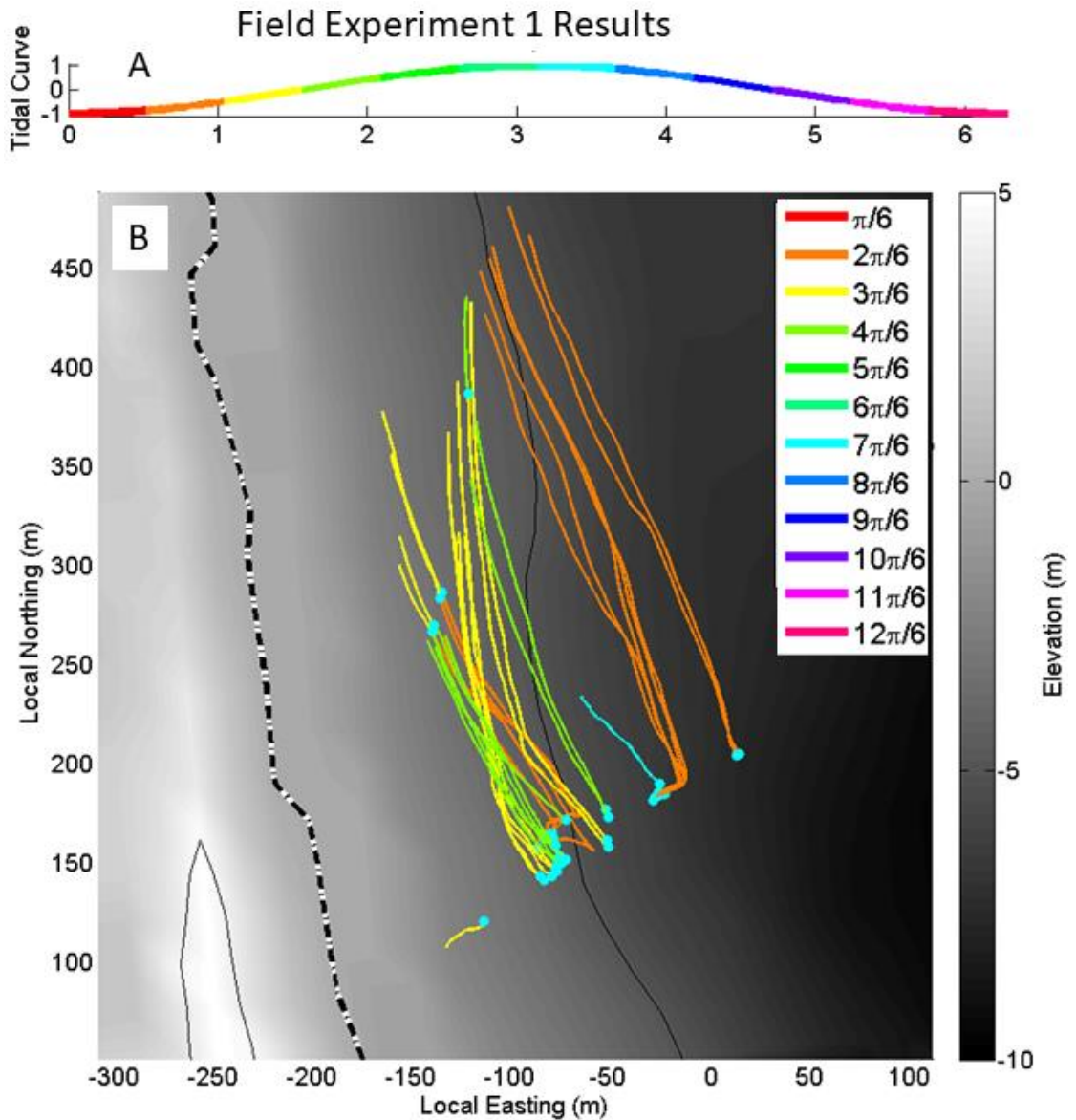


Figure 13: A) Idealized tidal curve divided into twelve phases. Color indicates tidal phase grouping. B) Drifter tracks collected in the first field experiment on 05/26/2016 plotted over model input bathymetry. Color indicates tidal phase. Release points are indicated in cyan. Drifter position time series have been filtered with a running average using a window size of 120 s. Plot coordinates are referenced to a local northing and easting with an origin at the north jetty tip.

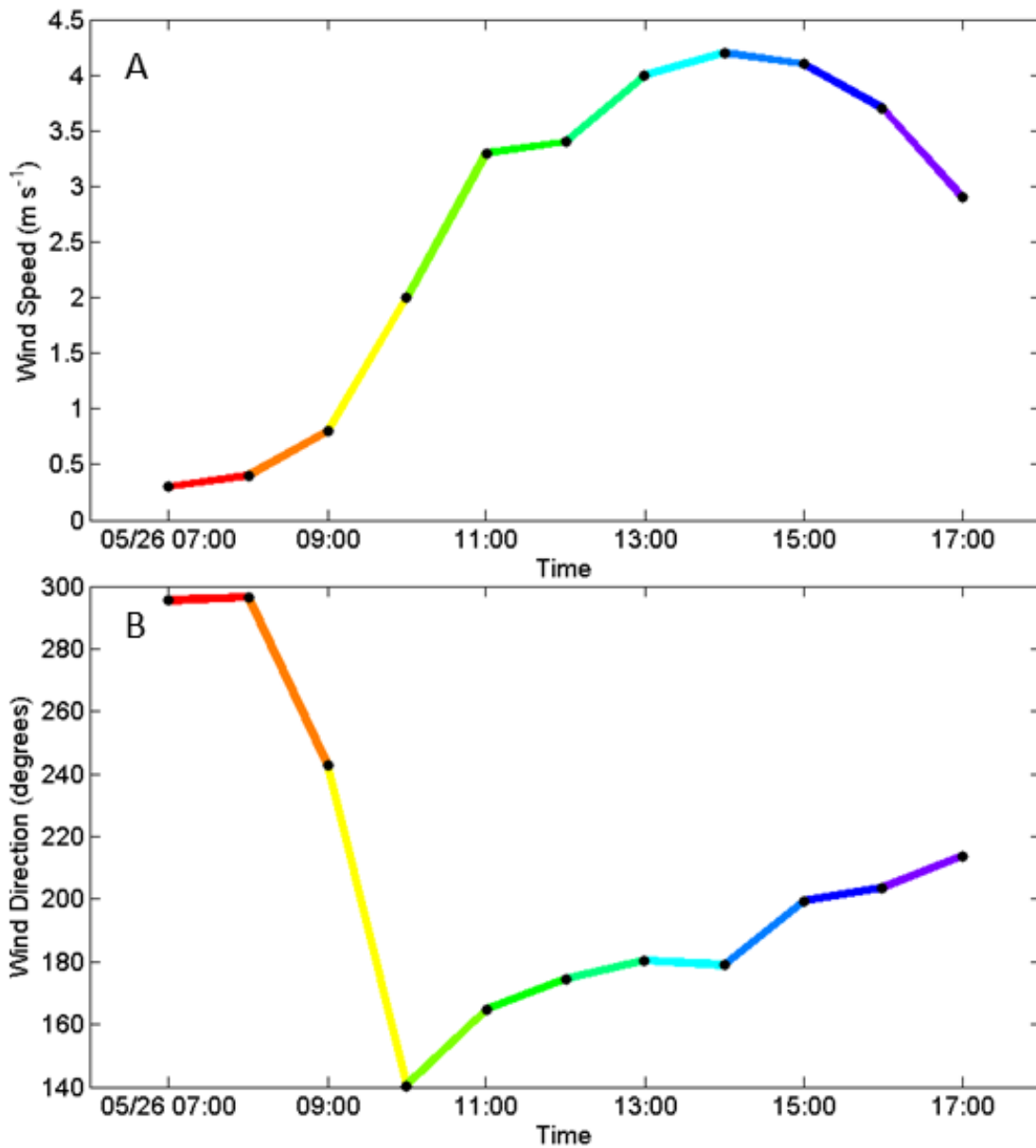


Figure 14: A) Measured wind speed during the observed tidal cycle at the Delaware Environmental Observing System (DEOS) station 2.7 km north of the Indian River Inlet in the first field experiment ([http://www.deos.udel.edu/data/daily\\_retrieval.php](http://www.deos.udel.edu/data/daily_retrieval.php)). Color indicates tidal phase, specified in Figure 13a. B) Measured wind direction during the observed tidal cycle at the DEOS station near the Indian River Inlet. Color indicates tidal phase.

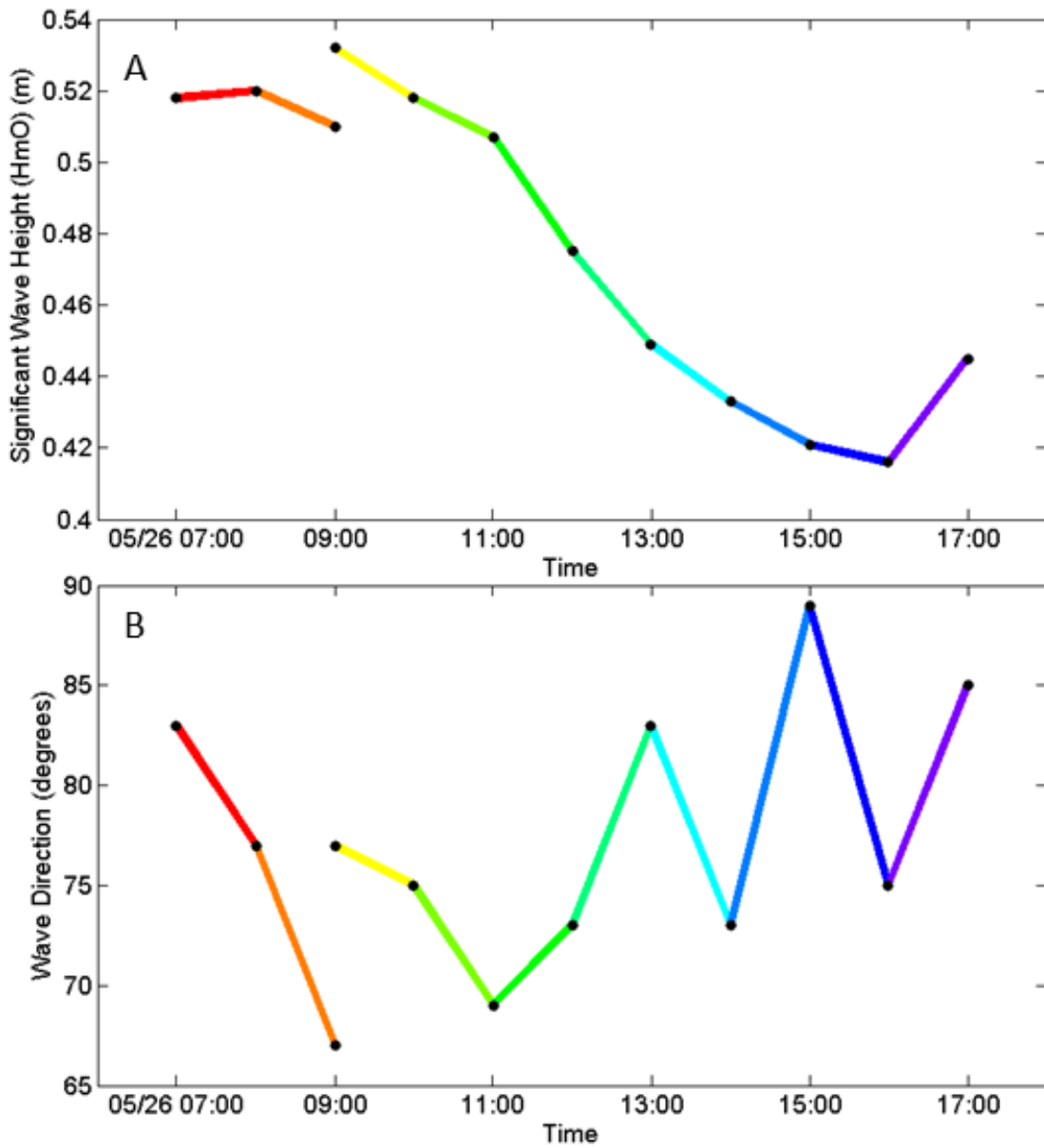


Figure 15: A) Significant wave height determined from measured wave spectra at the USACE wave gauge DE003 DWG-BB03 off of Bethany Beach during the first field experiment (<http://www.frf.usace.army.mil/bethanybeach/bb.shtml>). Color indicates tidal phase, specified in Figure 13a. B) Wave direction measured at the USACE wave gauge east of Bethany Beach. Color indicates tidal phase.

## 4.2 Field Experiment II

The second full scale field experiment was conducted on 10/20/16 between 8:30 AM and 2:30 PM EDT. Semidiurnal tidal phase information of collected data varied between three hours after low tide and two hours after high tide. Drifter releases occurred predominantly in the rising tide. Tidal range during the second field experiment was predicted to be 1.0 m within the inlet with an oceanic tidal range of 1.6 m. In the second field experiment, tidal range was more than one standard deviation above the mean. Wind speeds near the inlet were between  $2 \text{ m s}^{-1}$  and  $6.5 \text{ m s}^{-1}$  out of the east to south (Figure 17). As wind velocities exceeded  $6 \text{ m s}^{-1}$ , wind slippage may have had a substantial impact on drifter tracks, and is thus considered with tracks recorded in high winds. Significant wave heights were between 0.4 m and 0.55 m (Figure 18). Wave direction was out of the east and wave period was approximately 12 s.

Drifter position data show drifters generally heading onshore with spatial and temporal variability in the alongshore path components (Figure 16). Drifters in the  $3\pi/6$  and  $4\pi/6$  tidal phases traveled northwest more than 100 m from the jetty tip. In the  $4\pi/6$  tidal phase, drifters approximately 100 m north of the north jetty traveled southwest, and curved south entering the inlet channel. Drifters in the  $5\pi/6$  tidal phase moved northwest, though the minimum relative northing position recorded was approximately 300 m. Data from the  $7\pi/6$  tidal phase display varied alongshore motion. In the  $7\pi/6$  tidal phase drifters fewer than 200 m north of the inlet traveled southwest, with those not collected curling around the jetty and into the inlet. Several drifters more than 300 m from the inlet but fewer than 400 m traveled north northwest. Drifters at an approximate relative northing of 400 m moved in varied directions, similar to the drifters recorded in the  $7\pi/6$  phase at a relative northing of

approximately 300 m. Wind velocities were between  $5 \text{ m s}^{-1}$  and  $6.5 \text{ m s}^{-1}$  with a direction from the southeast between  $160^\circ$  and  $170^\circ$ . The combination of the wind speed and angle may have pushed drifters to the northwest in the  $7\pi/6$  and  $8\pi/6$  tidal phases with a wind slippage speed near  $0.06 \text{ m s}^{-1}$ . Although the wave directions in the  $7\pi/6$  and  $8\pi/6$  tidal phases were from the east northeast between  $70^\circ$  and  $90^\circ$ , which matches the drifter motion, significant wave height decreased to approximately 0.43 m and so Stokes drift is likely small. Drifters estimated velocities between  $0.1 \text{ m s}^{-1}$  and  $0.25 \text{ m s}^{-1}$  suggesting that the drifters may have been pushed by wind slippage, but the underlying currents were flowing a similar direction. Unless the estimates of wind slippage or Stokes drift underestimate these errors by a factor of two, the drifter tracks most probably display the direction of the current, though with a potentially erroneous speed. Drifters inside the inlet traveled west towards the inlet throat in the  $7\pi/6$  phase indicating that flow had reversed within the inlet, however, the prior entrainment in an eddy limits the ability to address when flow reversal occurred. Drifter tracks observed in the second field experiment also indicate flow divergence north of the inlet, with an area of southern velocities during the rising tide within a larger scale flow to the north in small to typical winds, average waves, and a tidal range more than one standard deviation above the mean.

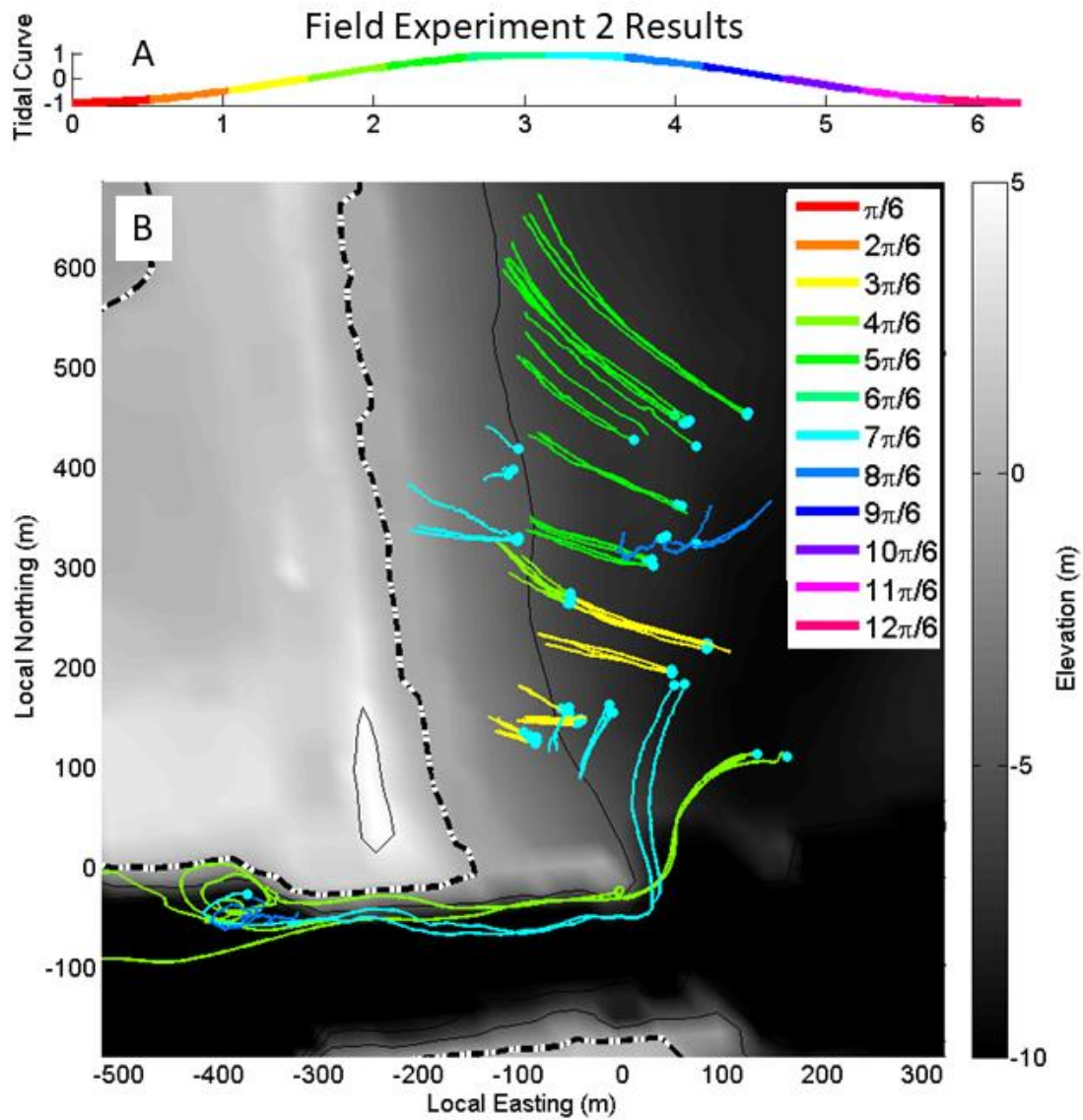


Figure 16: A) Idealized tidal curve divided into twelve phases. Color indicates tidal phase grouping. B) Drifter tracks collected in the second field experiment on 10/20/2016 plotted over bathymetry. Color indicates tidal phase. Release points are indicated in cyan. Drifter position time series have been filtered with a running average using a window size of 120 s. Plot coordinates are referenced to a local northing and easting with an origin at the north jetty tip.

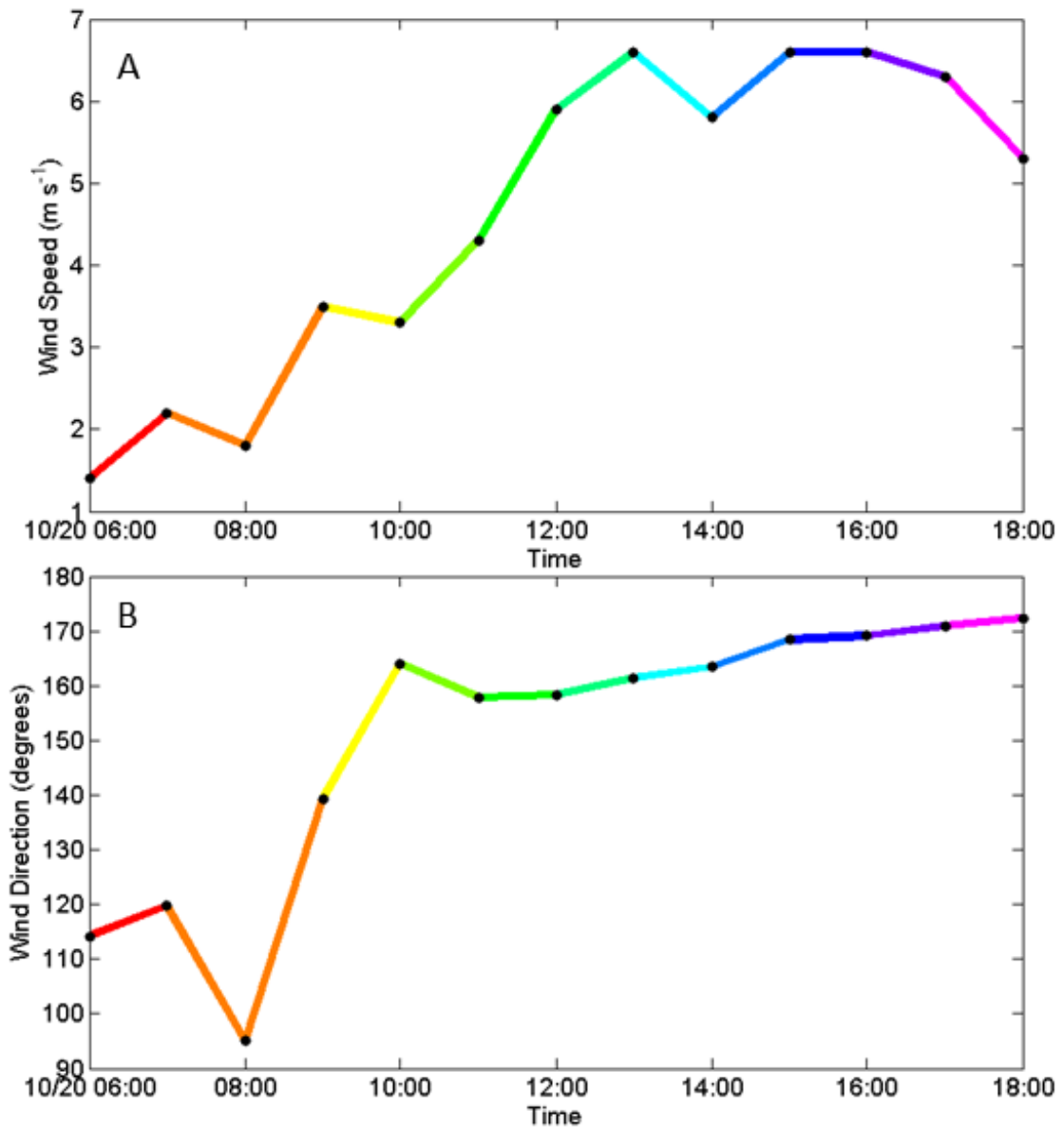


Figure 17: A) Measured wind speed during the observed tidal cycle north of the Indian River Inlet in the second field experiment ([http://www.deos.udel.edu/data/daily\\_retrieval.php](http://www.deos.udel.edu/data/daily_retrieval.php)). Color indicates tidal phase, specified in Figure 16a. B) Measured wind direction during the observed tidal cycle north of the Indian River Inlet. Color indicates tidal phase.

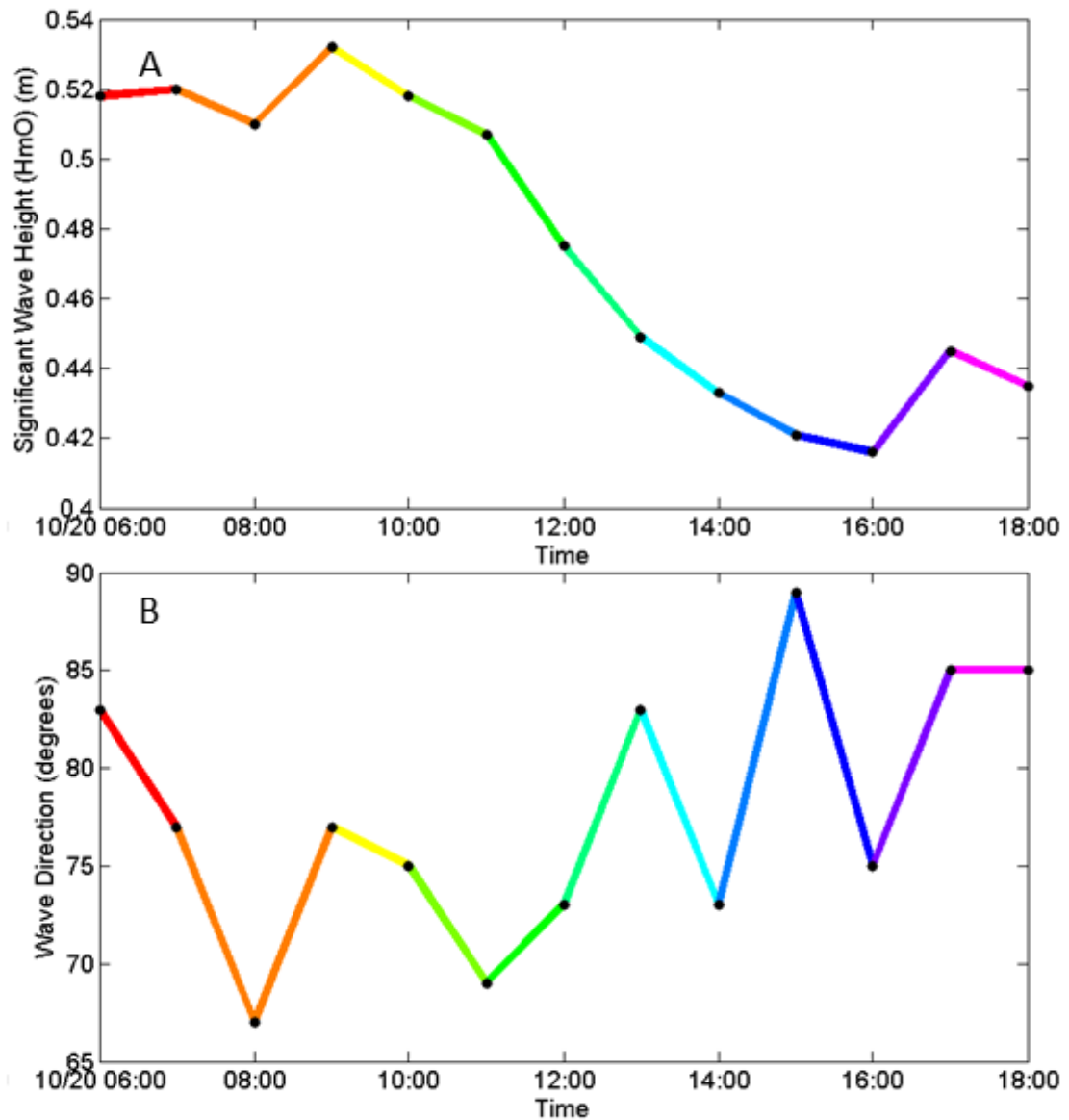


Figure 18: A) Significant wave height determined from measured wave spectra off of Bethany Beach during the second field experiment (<http://www.frf.usace.army.mil/bethanybeach/bb.shtml>). Color indicates tidal phase, specified in Figure 16a. B) Wave direction measured off of Bethany Beach. Color indicates tidal phase.

### 4.3 Field Experiment III

The third full scale field experiment was conducted on 05/08/17 between 9:00 AM and 2:30 PM EDT. Semidiurnal tidal phase information varied between one hour after high tide and one hour after low tide. Drifters were mostly released in the ebbing tide. Tidal range during the third field experiment was predicted as 0.78 m within the inlet with an oceanic tide of 1.10 m, which is well within one standard deviation of the mean. Wind speeds near the inlet were between  $5 \text{ m s}^{-1}$  and  $6 \text{ m s}^{-1}$  out of the west northwest (Figure 20). Significant wave heights were between approximately 0.45 m and 0.62 m (Figure 21). Wave direction was out of the southeast to east with wave periods of approximately 9 s.

Data collected in the third field experiment contain drifters traveling southeast and being advected offshore by the ebb jet with tidal variation in jet deflection (Figure 19). Data collection began in the  $9\pi/6$  tidal phase with drifters heading southeast, and entering the flow out of the inlet. Drifters moved southeast north of the ebb jet with relatively minor tidal variability. Wind speeds were between 5 and  $6 \text{ m s}^{-1}$  with directions between  $305^\circ$  and  $290^\circ$ , indicating that wind slippage was similar to drifter track angle, however, drifter velocities were between  $0.15 \text{ m s}^{-1}$  and  $0.3 \text{ m s}^{-1}$  north of the ebb jet and so, while velocities may have been increased by wind slippage, measurements are almost certainly reflective of underlying current directions. Considering the angle or deflection of the ebb jet as the angle formed between the appropriate drifter tracks and an axis pointing out of the inlet, ebb jet angle decreased through the  $10\pi/6$ ,  $11\pi/6$ , and  $\pi/6$  tidal phases. The ebb jet had taken a severe angle to the north in the  $2\pi/6$  tidal phase when drifters traveled southeast and near the jetty tip turned sharply and traveled northeast. Drifters tracks in the third field experiment indicate that in typical wind, wave, and tidal range conditions, the general flow pattern

north of the inlet was to the south through the latter half of the ebbing tide and the first two phases of the rising tide with ebb jet entrainment and a decreasing ebb jet deflection.

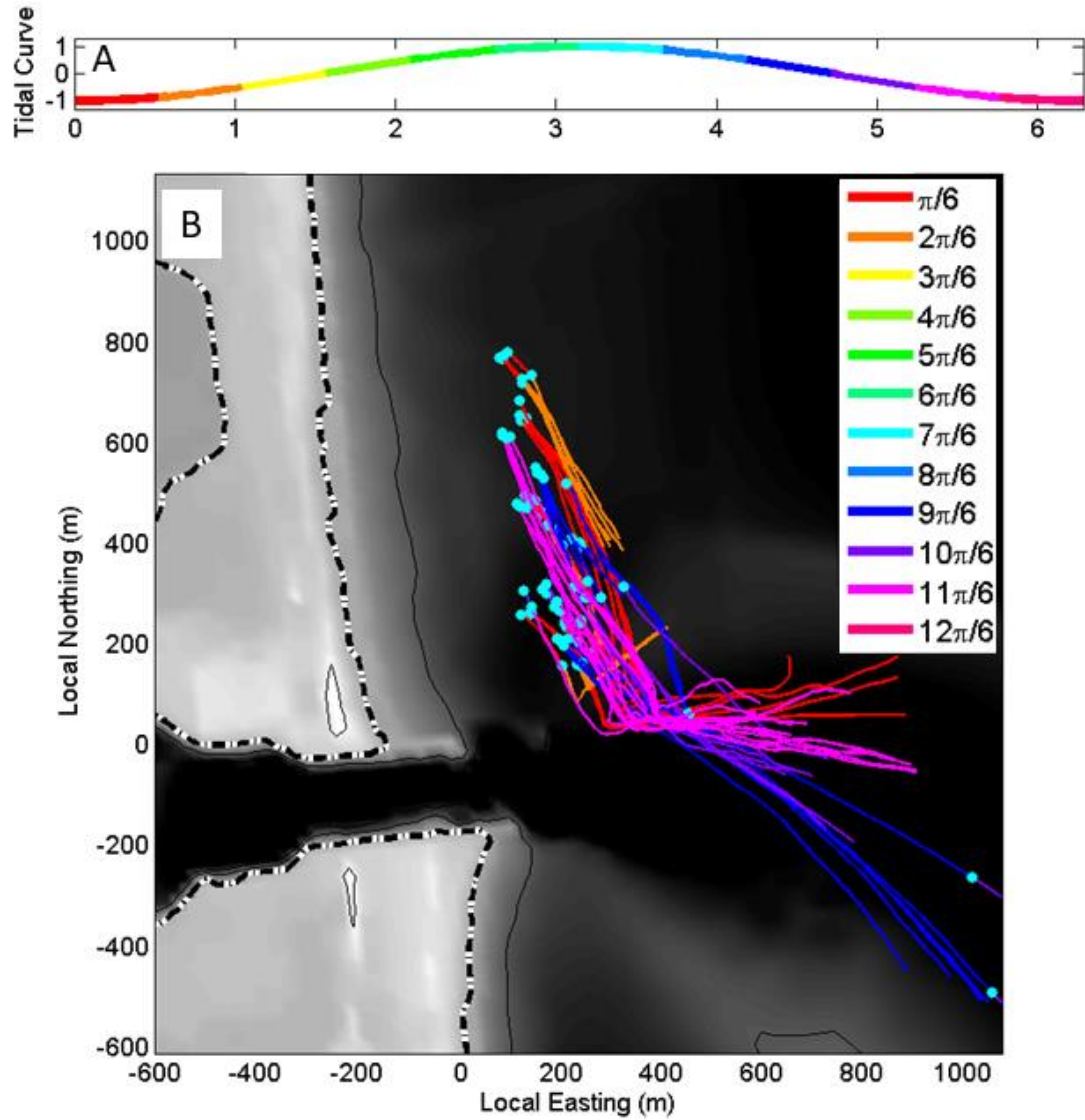


Figure 19: A) Idealized tidal curve divided into twelve phases. Color indicates tidal phase grouping. B) Drifter tracks collected in the third field experiment on 05/08/2017 plotted over bathymetry. Color indicates tidal phase. Release points are indicated in cyan. Drifter position time series have been filtered with a running average using a window size of 120 s. Plot coordinates are referenced to a local northing and easting with an origin at the north jetty tip.

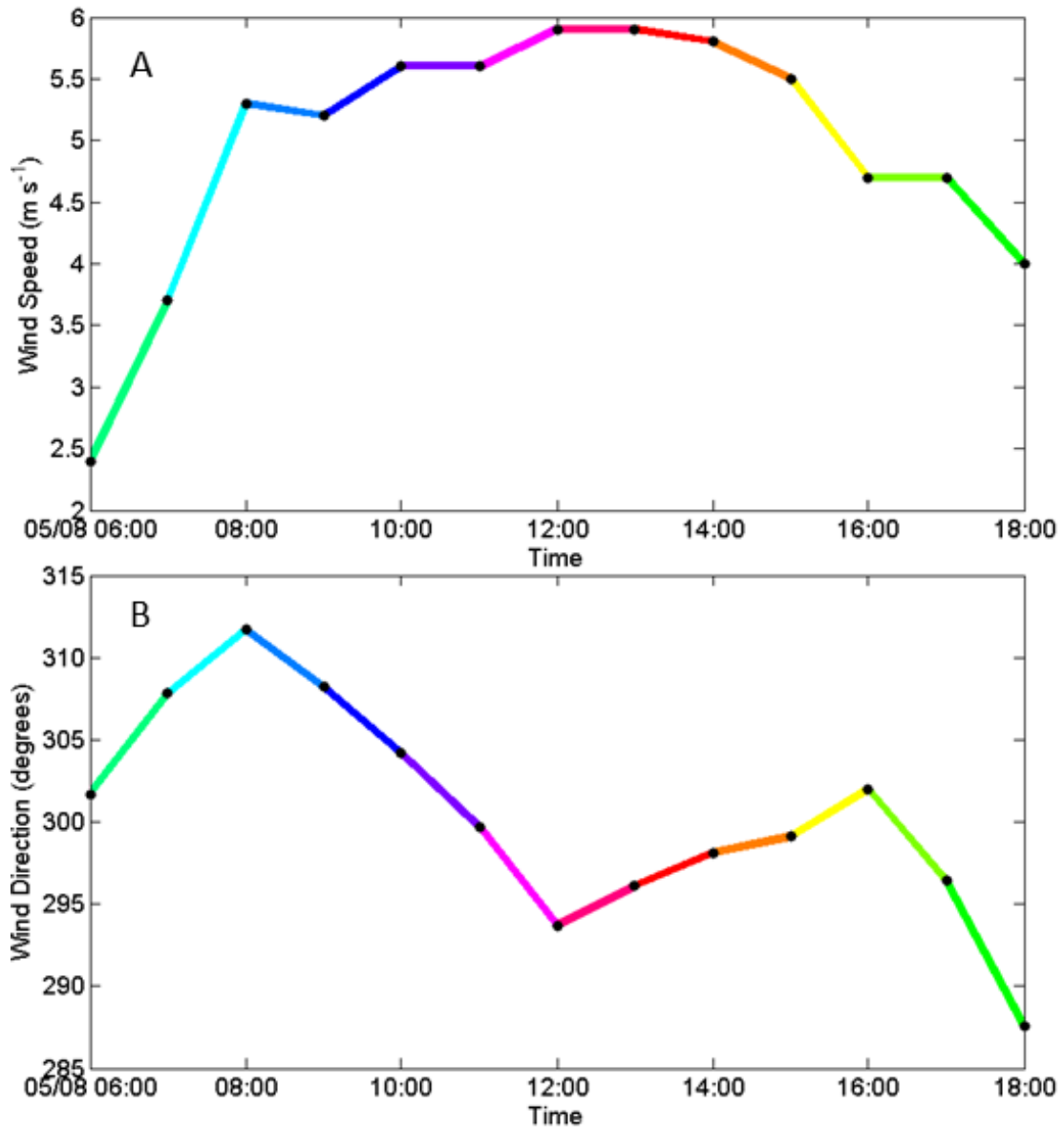


Figure 20: A) Measured wind speed during the observed tidal cycle north of the Indian River Inlet in the third field experiment ([http://www.deos.udel.edu/data/daily\\_retrieval.php](http://www.deos.udel.edu/data/daily_retrieval.php)). Color indicates tidal phase, specified in Figure 19a. B) Measured wind direction during the observed tidal cycle north of the Indian River Inlet. Color indicates tidal phase.

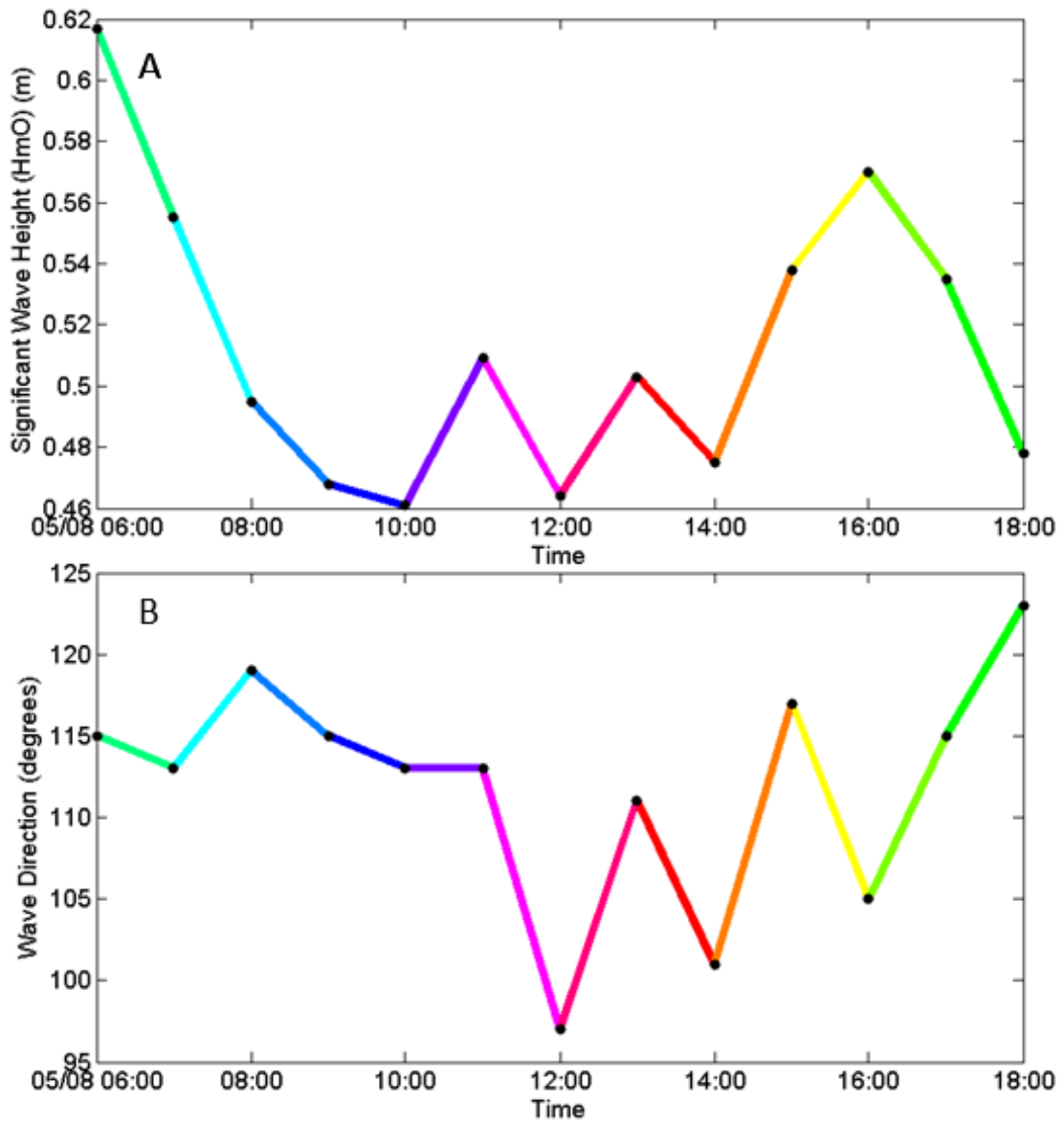


Figure 21: A) Significant wave height determined from measured wave spectra off of Bethany Beach during the third field experiment (<http://www.frf.usace.army.mil/bethanybeach/bb.shtml>). Color indicates tidal phase, specified in Figure 19a. B) Wave direction measured at the off of Bethany Beach. Color indicates tidal phase.

#### 4.4 Field Experiment IV

The fourth full scale field experiment was conducted on 05/30/17 between 10:30 AM and 3:00 PM EDT. Semidiurnal tidal phase information varied between three and a half hours after low tide to one and a half hours after high tide. Drifters were released in both the flooding and ebbing tides. Tidal range during the fourth field experiment was predicted as 0.9 m within the inlet and 1.1 m at Bethany Beach, which is well within one standard deviation of the mean. Wind speeds near the inlet were between  $3 \text{ m s}^{-1}$  and  $8 \text{ m s}^{-1}$  out of the southeast to east (Figure 23). Significant wave heights were between approximately 0.9 m and 1 m (Figure 24). Wave direction was out of the northeast with wave periods of approximately 11 s.

Data coverage during the fourth field experiment was poor. Although the fourth field experiment had a similar number of drifter releases, usable position data were limited. Various factors such as rough weather conditions during data collection resulted in GPS system errors such as connections shaking loose and the loss of satellite lock. Data were successfully recorded over the three hours around high tide (Figure 22). Drifter tracks in the  $5\pi/6$  tidal phase traveled onshore, with a small alongshore flow component changing direction between 300 m and 450 m north of the inlet. Winds in the  $5\pi/6$  tidal phase were between  $4$  and  $6 \text{ m s}^{-1}$ , out of the southeast at  $110^\circ$  to  $100^\circ$ , with associated wind slippage to the northwest, possibly being responsible for the northward component in observed drifter speeds. Waves from the northeast with significant wave heights of 0.9 could have also contributed to the flow to the west observed by all drifters, and the southerly component of the drifters within 300 m north of the inlet. Drifter speeds were between  $0.2 \text{ m s}^{-1}$  and  $0.25 \text{ m s}^{-1}$ , so, while potentially influenced by wind slippage and Stokes drift, drifters likely traveled with the underlying current pattern. Observed drifter tracks were to the northwest in

the  $6\pi/6$  tidal phase, with recorded data between 400 m and 1200 m north and 200 m and 800 m east of the north jetty tip. Drifters traveled west southwest to southwest in the  $7\pi/6$  tidal phase. Winds were from the southeast in the  $7\pi/6$  tidal phase at approximately  $3 \text{ m s}^{-1}$  and so could be reflected in the westerly component of the drifter tracks. Waves from the east northeast, with a significant wave height of approximately 0.95 m, may have also pushed drifters west. Drifter speeds smaller than  $0.15 \text{ m s}^{-1}$  do not indicate that wind and wave effects did not influence tracks substantially, however, the impacts of wind and waves may be further addressed when comparing results across all field experiments.

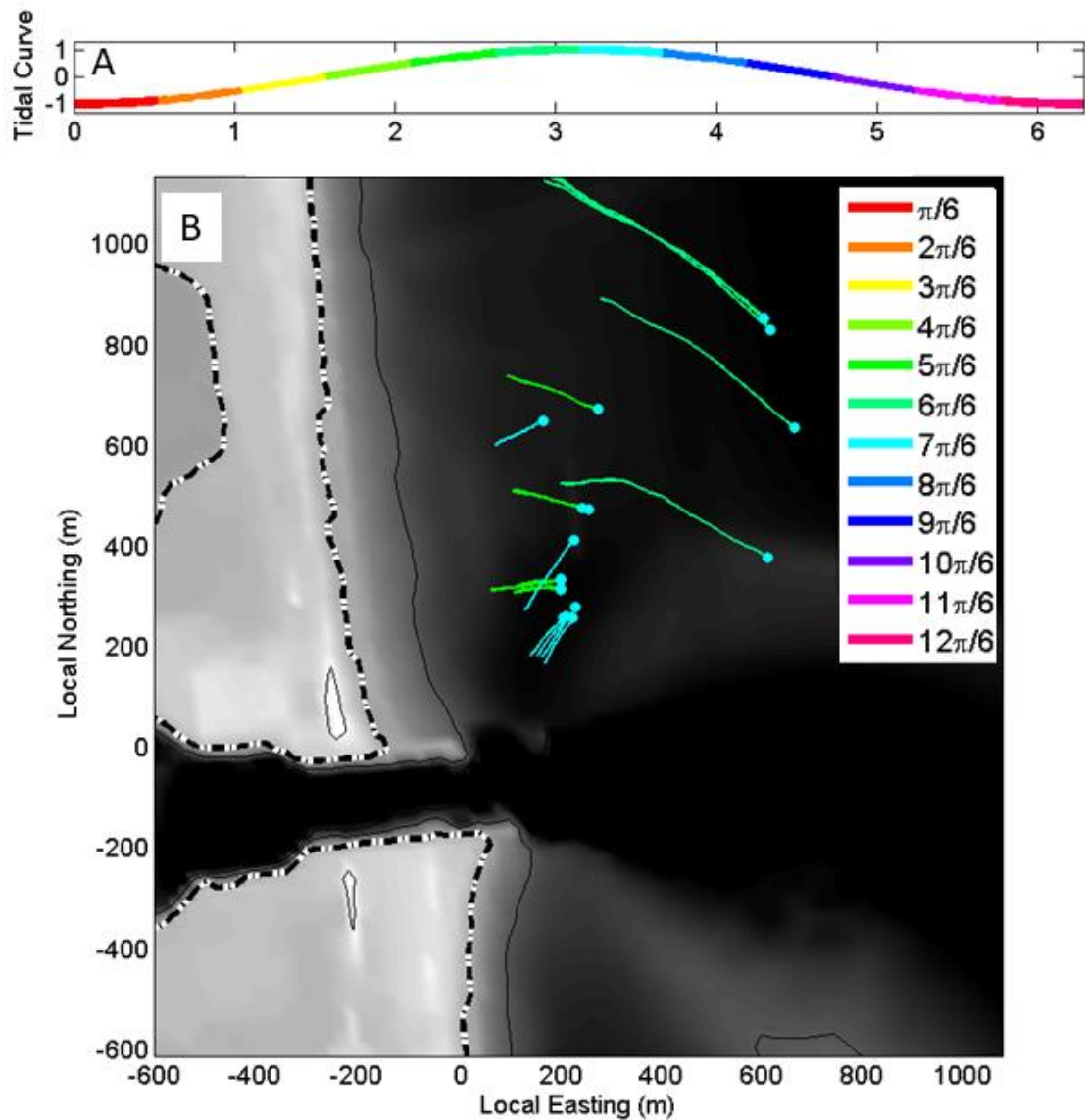


Figure 22: A) Idealized tidal curve divided into twelve phases. Color indicates tidal phase grouping. B) Drifter tracks collected in the fourth field experiment on 05/30/2017. Color indicates tidal phase. Drifter position time series have been filtered with a running average using a window size of 120 s. Plot coordinates are referenced to a local northing and easting with an origin at the north jetty tip.

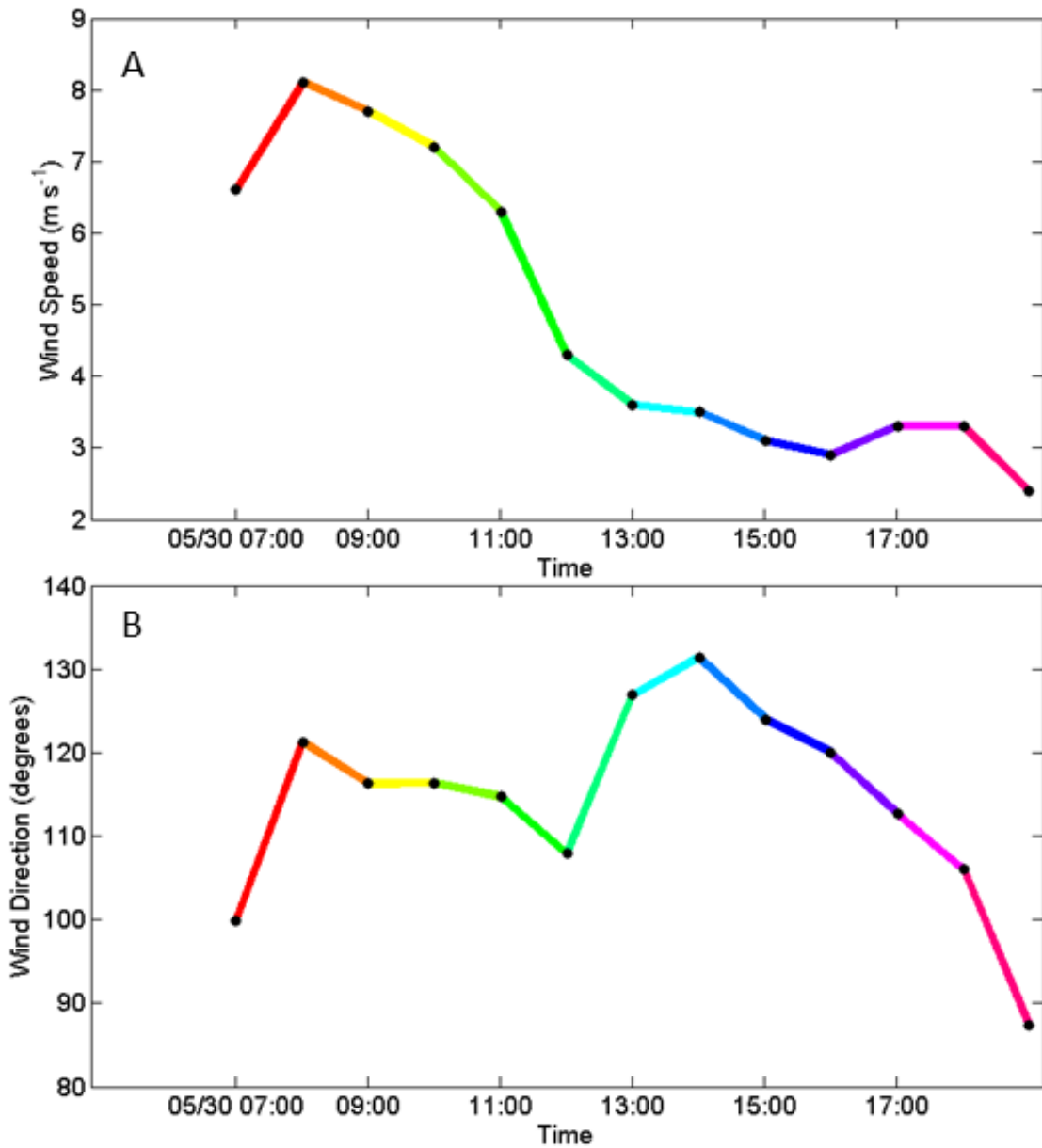


Figure 23: A) Measured wind speed during the observed tidal cycle north of the Indian River Inlet during the fourth field experiment ([http://www.deos.udel.edu/data/daily\\_retrieval.php](http://www.deos.udel.edu/data/daily_retrieval.php)). Color indicates tidal phase, specified in Figure 22a. B) Measured wind direction during the observed tidal cycle at the north of the Indian River Inlet. Color indicates tidal phase.

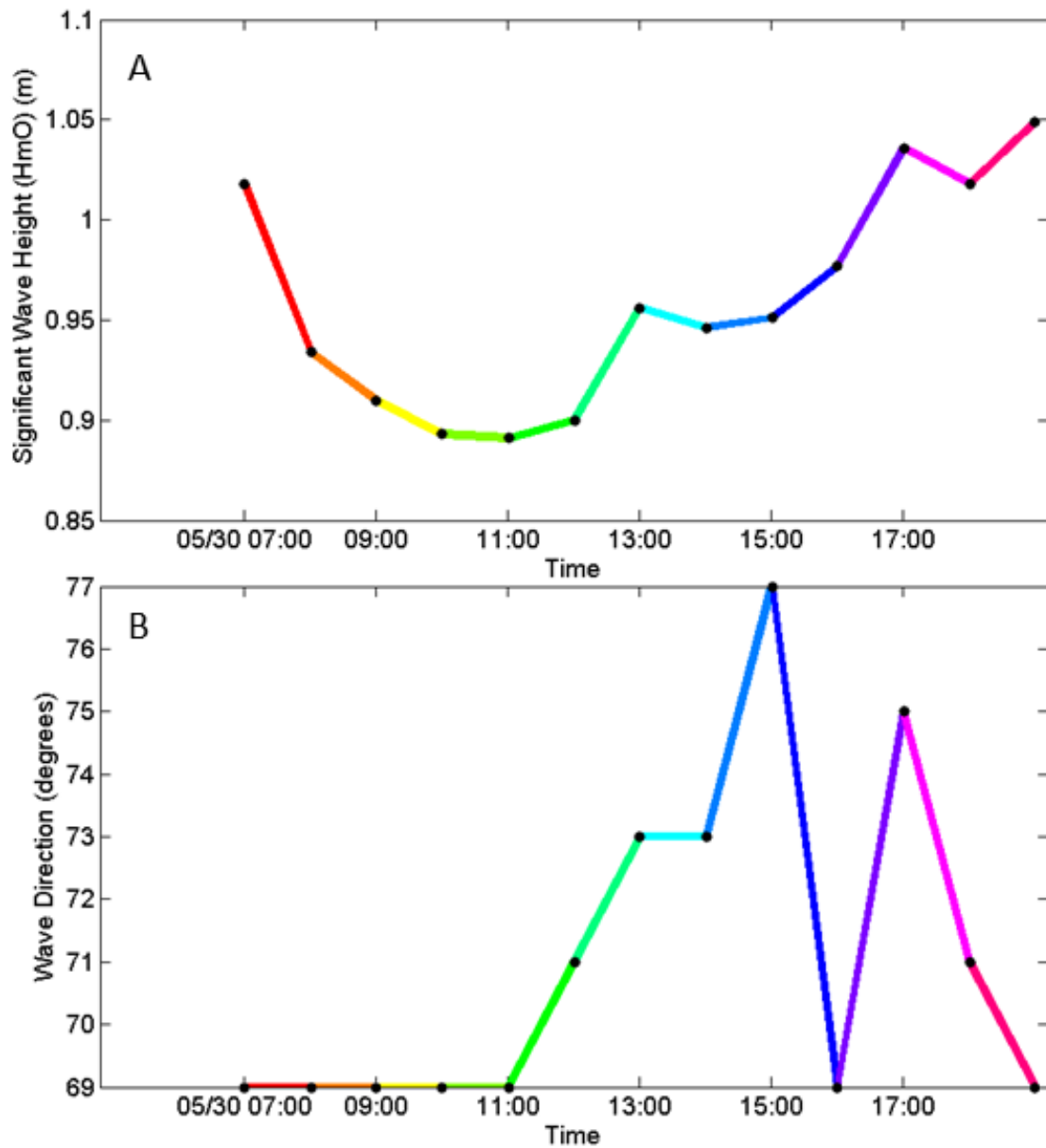


Figure 24: A) Significant wave height determined from measured wave spectra off of Bethany Beach during the third field experiment (<http://www.frf.usace.army.mil/bethanybeach/bb.shtml>). Color indicates tidal phase, specified in Figure 22a. B) Wave direction measured at the off of Bethany Beach. Color indicates tidal phase.

#### 4.5 Field Experiment Results Separated by Tidal Phase

Drifter track data are compared between experiments in tidal phase groupings. Data were separated into tidal phases in each experiment and combined in each tidal phase across all four field experiments. Combining data collected in the different experiments by tidal phase improves the spatial and temporal resolution of data available for comparisons of flow feature variation with tidal phase. Wind, wave, and tidal range are among the major factors not represented in a tidal phase grouped view. Drifter track data indicate substantial tidal phase dependence, though other factors may be observed to influence current patterns.

Data collected in the rising tide during the four field experiments varied with tidal phase including drifter paths to the southeast and into the ebb jet and paths to the northwest. Drifters sampling during the  $\pi/6$  and earlier  $2\pi/6$  tidal phases moved southeast and into the flow exiting the inlet (Figure 25a; Figure 25b). Drifter path direction in the  $2\pi/6$  tidal phase varied by approximately  $180^\circ$ , with tracks collected later in the  $2\pi/6$  tidal phase angled northwest (Figure 25b). The majority of drifter tracks observed between the  $3\pi/6$  and  $6\pi/6$  tidal phases were to the north or northwest suggesting a dominant alongshore component of flow to the north more than 200 m north of the inlet (Figure 25c; Figure 25d; Figure 25e). Drifters generally traveled to the northwest in the  $4\pi/6$  tidal phase, though limited data were collected (Figure 25f). Drifter tracks fewer than 140 m in the  $3\pi/6$  and 100 m in the  $4\pi/6$  tidal phases had alongshore flow components to the south (Figure 25d; Figure 25e). Several drifters at an approximate relative northing of 300 m traveled west southwest in the  $5\pi/6$  tidal phase, however, drifters at a similar northing, in the same phase, traveled northwest during a different field experiment. Drifter tracks collected in the  $3\pi/6$  to  $5\pi/6$  tidal

phases indicate a divergence point at variable locations in a larger scale flow to the north, but divergence point location appears to vary with factors other than tidal phase.

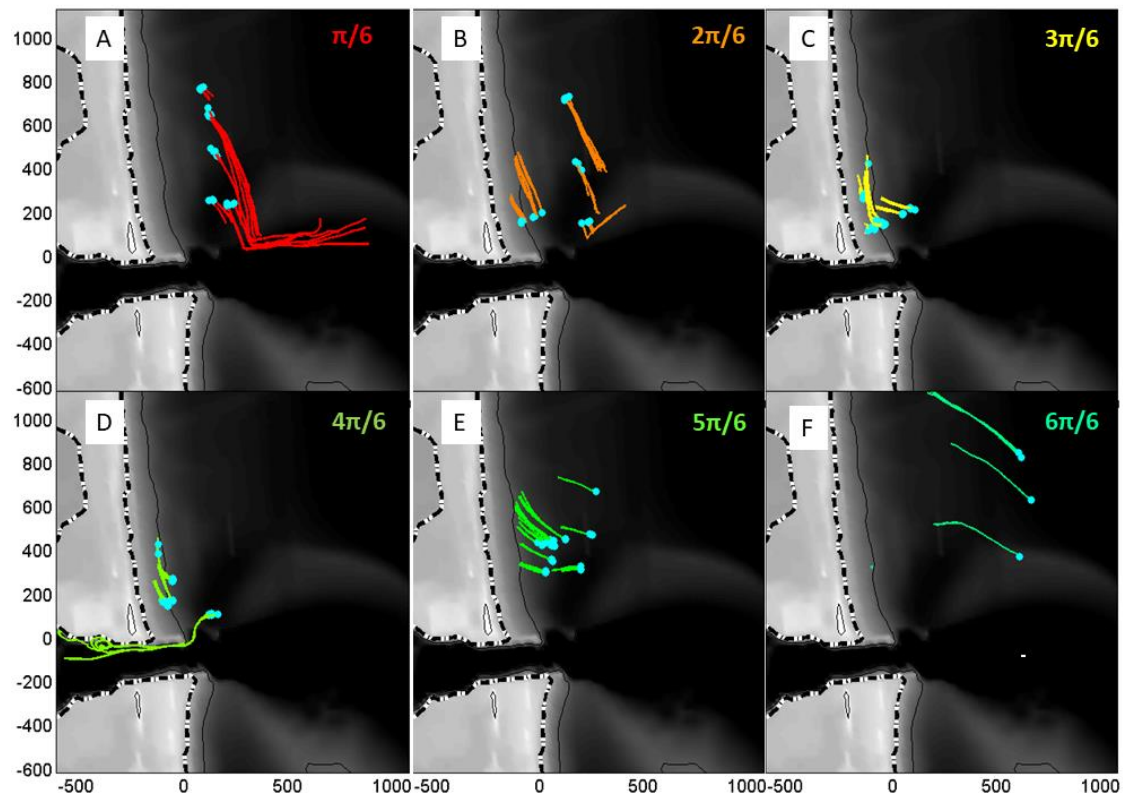


Figure 25: Drifter track data collected in the rising tide separated by tidal phase and plotted on bathymetry. Coordinates are relative to the north jetty tip. Line color indicates tidal phase as defined in Figure 22. Release points are indicated in cyan.

Drifter tracks collected in the falling tide during the four field experiments are generally to the south with cross-shore motion often related to the direction of flow within the inlet channel. Most drifters observed north of the inlet in the  $7\pi/6$  tidal

phase traveled southwest, with several drifters entering the inlet and an eddy at an angle in the shoreline armoring (Figure 26a). The inlet directed drifter paths in the  $4\pi/6$  and  $7\pi/6$  tidal phases would support the claim that a region of flow to the south is present throughout the rising tide. The  $7\pi/6$  tidal phase also contained drifters traveling onshore as well as drifters traveling to the northwest. Drifters in the  $8\pi/6$  tidal phase traveled in varied directions, though data were somewhat limited (Figure 26b). One of the drifters entrained in the eddy at the shoreline armoring angle exited the eddy and traveled east in the  $8\pi/6$  tidal phase, providing the earliest ebb jet measurement in the falling tide. Between the  $9\pi/6$  and  $12\pi/6$  tidal phases drifters traveled southeast and were entrained in the ebb jet (Figure 26c; Figure 26d; Figure 26e; Figure 26f). Drifter motion to the south in the ebb jet decreased with tidal phase, continuing into the  $\pi/6$  tidal phase, with an ebb jet angled to the north in the  $2\pi/6$  tidal phase.

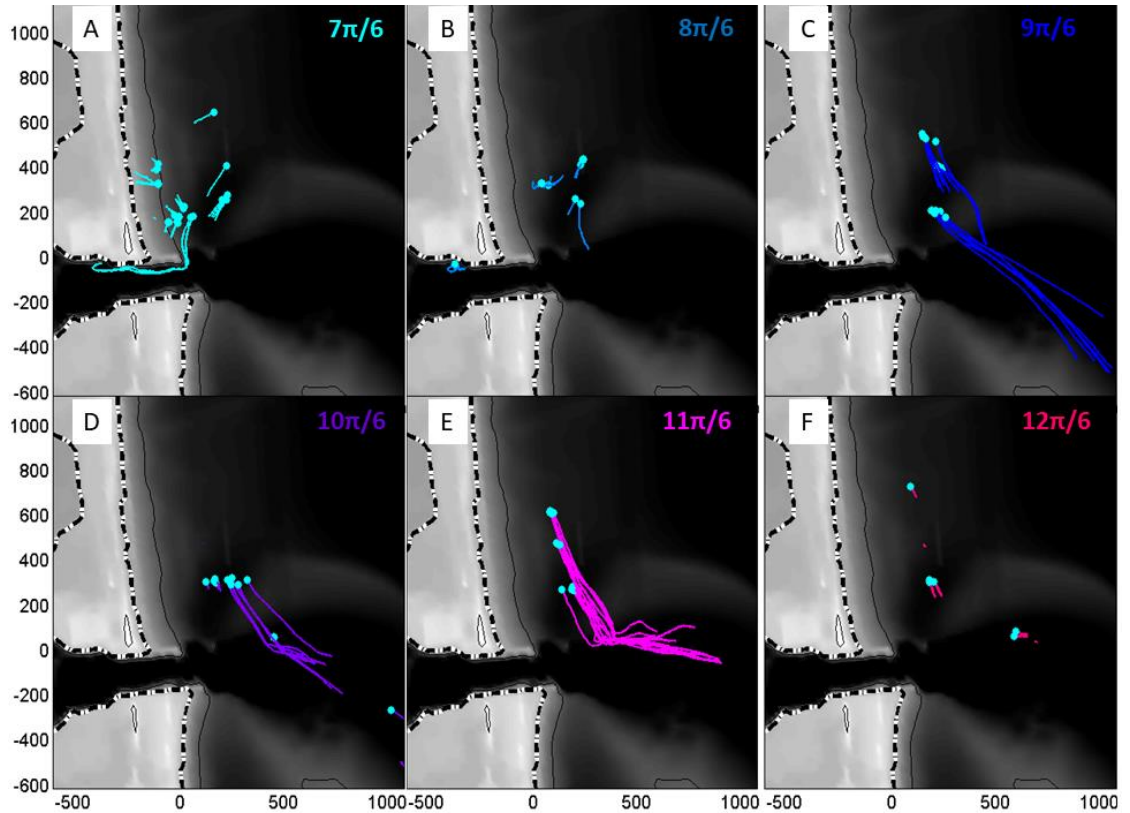


Figure 26: Drifter track data (line from cyan dot) collected in the falling tide separated by tidal phase and plotted on bathymetry. Coordinates are relative to the north jetty tip. Line color indicates tidal phase as defined in Figure 22. Drifter release points are indicated in cyan.

Flow speed information was determined by differencing the time series of position data recorded for each drifter. Tidal phase grouped drifter speeds display relatively consistent trends with tidal phase. The  $\pi/6$ ,  $9\pi/6$ ,  $10\pi/6$ , and  $11\pi/6$  tidal phases display similar spatial flow speed trends, as do the  $3\pi/6$ ,  $4\pi/6$ , and  $5\pi/6$  tidal phases. Drifter speeds north of the inlet were typically between  $0.1 \text{ m s}^{-1}$  and  $0.3 \text{ m s}^{-1}$  during the  $\pi/6$  and  $2\pi/6$  tidal phases (Figure 27a). Drifter speeds rapidly increased on entering the ebb jet in the  $\pi/6$  tidal phase, exceeding  $0.45 \text{ m s}^{-1}$ . Ebb jet sections with

drifter speeds below  $0.4 \text{ m s}^{-1}$ ,  $0.25 \text{ m s}^{-1}$ , and  $0.1 \text{ m s}^{-1}$  were observed in the  $\pi/6$  and  $2\pi/6$  tidal phases. In the  $3\pi/6$  and  $4\pi/6$  tidal phases drifter speeds decreased from greater than  $0.35 \text{ m s}^{-1}$  to less than  $0.2 \text{ m s}^{-1}$  traveling onshore and northwest, and increased from less than  $0.25 \text{ m s}^{-1}$  to greater than  $0.45 \text{ m s}^{-1}$  approximately 100 m before entering the inlet (Figure 27b). Drifter speeds in the  $3\pi/6$  and  $4\pi/6$  tidal phases which were fewer than 200 m offshore were typically between  $0.1 \text{ m s}^{-1}$  and  $0.2 \text{ m s}^{-1}$  despite the greater than two standard deviation tidal range difference between the two main data sources for the area. Drifter speeds within the inlet channel during the  $3\pi/6$  and  $4\pi/6$  tidal phases generally exceeded  $0.45 \text{ m s}^{-1}$ . During the  $5\pi/6$  and  $6\pi/6$  tidal phases drifter speeds often decreased with onshore motion (Figure 27c). Drifter speeds were relatively fast in the  $5\pi/6$  and  $6\pi/6$  tidal phases with values typically between  $0.2 \text{ m s}^{-1}$  and  $0.4 \text{ m s}^{-1}$ .

Drifter speeds were typically slow more than 50 m north of the inlet in the  $7\pi/6$  and  $8\pi/6$  tidal phases with numerous values less than  $0.1 \text{ m s}^{-1}$  and the fewest speeds greater than  $0.25 \text{ m s}^{-1}$  of any  $2\pi/6$  tidal phase grouping (Figure 27d). Drifters speeds fewer than 50 m from the inlet channel were typically greater than  $0.45 \text{ m s}^{-1}$  in the  $7\pi/6$  tidal phase. At a similar time to flow reversal within the inlet drifters decelerated from  $0.45 \text{ m s}^{-1}$  to less than  $0.1 \text{ m s}^{-1}$  within an eddy which formed at an angle in the shoreline armoring. During the  $9\pi/6$  and  $10\pi/6$  tidal phases drifter speeds were often between  $0.15 \text{ m s}^{-1}$  and  $0.3 \text{ m s}^{-1}$  to the north of the inlet with occasional speeds as slow as  $0.1 \text{ m s}^{-1}$  (Figure 27e). Drifters south of the north jetty tip observed speeds generally greater than  $0.3 \text{ m s}^{-1}$  and often exceeding  $0.45 \text{ m s}^{-1}$ . During the  $11\pi/6$  and  $12\pi/6$  tidal phases drifter speeds were generally between  $0.15 \text{ m s}^{-1}$  and  $0.3 \text{ m s}^{-1}$  more than 50 m north of the inlet, and generally between  $0.25 \text{ m s}^{-1}$  and  $0.45 \text{ m s}^{-1}$  in the ebb

jet (Figure 27f). Speeds of drifters entrained in the ebb jet did not follow a constant trend with easting during the  $11\pi/6$  tidal phase. During the first seven tidal phases drifter speeds within 100 m north of the inlet generally exceed  $0.45 \text{ m s}^{-1}$  while in the falling tide drifter speeds within 100 m north of the inlet were generally greater than  $0.3 \text{ m s}^{-1}$  with fewer speeds exceeding  $0.45 \text{ m s}^{-1}$ . Rising tide drifter speeds farther than 100 m north of the inlet often displayed a weak proportionality with easting within each  $2\pi/6$  tidal phase grouping.

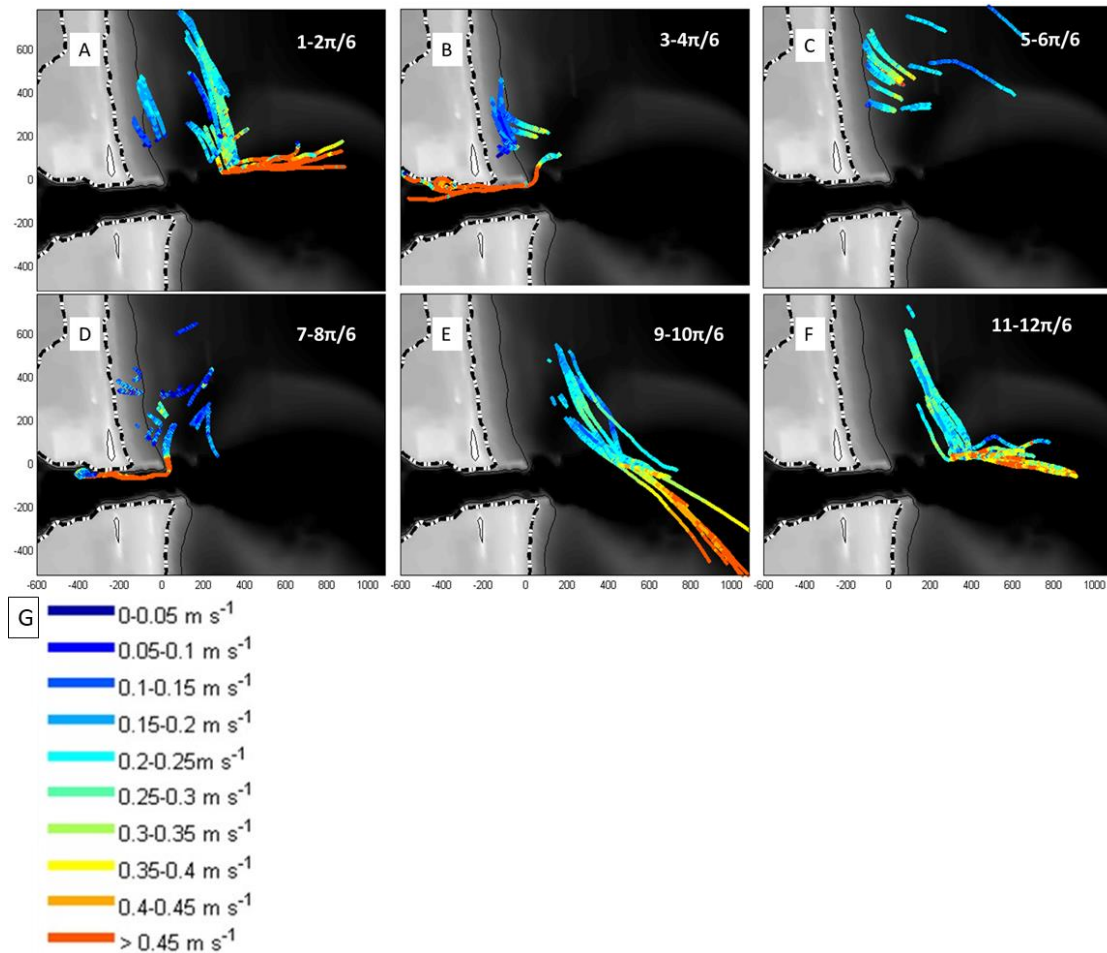


Figure 27: A-F) Drifter tracks from all field experiments separated into  $2\pi/6$  tidal phase groups and plotted over bathymetry. Color represents binned speed between  $0 \text{ m s}^{-1}$  and  $0.45 \text{ m s}^{-1}$ . G) Speed bins and corresponding colors used to plot drifter tracks as a function of speed.

Comparisons of drifter data grouped by tidal phase indicate similar flow features between tidal phases not involving flow reversal within the inlet. Drifter tracks collected in the  $3\pi/6$ ,  $4\pi/6$ , and  $5\pi/6$  tidal phases indicate larger scale flow to the north at speeds between  $0.15 \text{ m s}^{-1}$  and  $0.35 \text{ m s}^{-1}$ , and an area of flow to the south and into the inlet at similar speeds with rapid acceleration within 100 m of the inlet.

Drifter tracks collected north of the inlet in the  $9\pi/6$  to  $\pi/6$  tidal phases indicate flow to the southeast at speeds between  $0.15 \text{ m s}^{-1}$  and  $0.35 \text{ m s}^{-1}$  with drifters entrained in the ebb jet traveling at speeds typically between  $0.3 \text{ m s}^{-1}$  and  $0.45 \text{ m s}^{-1}$  with values occasionally exceeding  $0.45 \text{ m s}^{-1}$ . Drifter data from the  $2\pi/6$ ,  $7\pi/6$ , and  $8\pi/6$  tidal phases indicate substantial flow field variation with factors other than tidal phase. The direction of flow north of the inlet in the  $2\pi/6$  tidal phase varies by approximately  $180^\circ$  between the first and third field experiment, however, speeds were similar within  $0.1 \text{ m s}^{-1}$ . The flow fields indicated by drifter data from the  $7\pi/6$  and  $8\pi/6$  tidal phases display substantial directional variability to the north of the inlet with slow speeds, often less than  $0.1 \text{ m s}^{-1}$ , and the most speeds less than  $0.25 \text{ m s}^{-1}$ . Drifter data indicates that flow begins entering the inlet in the  $2\pi/6$  tidal phase and begins exiting the inlet between the  $7\pi/6$  or  $8\pi/6$ . The tidal phases in which flow reversed within the inlet correspond to the tidal phases without drifter tracks indicating distinct flow features varying with tidal phase.

## Chapter 5

### DELFT3D LARGE-SCALE 2D SIMULATION

Hydrodynamics in the vicinity of the Indian River Inlet were investigated with an online coupled large-scale 2D simulation in Delft3D Flow and Wave, forced with offshore wave and tidal water level information. Numerically simulated hydrodynamics were validated to the north of the inlet through quantitative comparison with previously collected Eulerian data from nine Aquadopps. Willmott scores and refined indices of agreement were calculated. Skill scores indicate that water level was predicted well, velocity was predicted with variable skill, and wave characteristics were not particularly well predicted. Simulated passive tracer paths were also compared to observed drifter tracks. Observed drifter tracks during the rising tide suggested partial agreement in simulated current patterns, with better agreement during the falling tide and particularly in the ebb jet. Accurate bathymetry is found to be important for hydrodynamic predictions near the Indian River Inlet through the comparison of simulations using bathymetry determined from different sources. The majority of the study area is found to be tidally dominated, based on Eulerian and Lagrangian comparisons of simulations using either both tide and wave or tide forcing only.

## 5.1 Tidal Forcing Simulations with Delft3D-Flow

Delft3D-FLOW simulates non-steady flows from phenomena forced by tidal and meteorological conditions with the capability of communication with a variety of other Delft3D modules (Delft Hydraulics, 2014a). Hydrodynamics are calculated with the incompressible Navier Stokes equations making use of the shallow water and Boussinesq assumptions and neglecting vertical accelerations in the vertical momentum equation (Delft Hydraulics, 2014a). In this study, the Delft3D-FLOW-model simulated the hydrodynamics associated with offshore tidal forcing as well as wave impacts from a coupling with Delft3D-WAVE.

Hydrodynamic modelling decisions were made by a combination of using default values, comparing results from various options, and applying knowledge of expectations. Parameters determined through the comparison of results included the bottom roughness value and the viscosities determined by the built in sub-grid scale Horizontal Large Eddy Simulation solver. The selection of advection term removal at the boundary, simulation duration, and timestep were based on knowledge of processes simulated. Tidally forced hydrodynamics were modeled over a simulation duration of sixteen days to capture the entire spring-neap tidal cycle. Simulations involving drifter tracks predicted sixteen days of hydrodynamics before the drifter releases, resulting in a seventeen day simulation. The simulation used a timestep of 1 minute. Bottom roughness was specified with the uniform default constant Chezy value of 65, as simulation comparisons indicated uniform Chezy bottom roughness value changes within 15 did not change validation scores by more than 0.05. The advection terms with normal gradients at the offshore boundary were removed with the additional parameter keyword  $Cstbnd = \#YES\#$ . Initial validations revealed that velocity validations improved substantially with the inclusion of the built in two-

dimensional sub-grid scale Horizontal Large Eddy Simulation (HLES) feature. The HLES feature used default parameters as the inclusion of a relaxation time between 5 and 45 minutes and exclusion of Elder's term did not impact validation scores by more than 0.05. Generally, numerical parameters and processes included followed the default or Delft3D tutorial setting, with the inclusion of the HLES solver as the most substantial exception.

### **5.1.1 Delft3D-FLOW Computational Grid**

The selected model domain began near the NOAA NDBC buoy 44009, and extended northwest to sufficiently upstream in the Delaware River and Bay (Figure 28a). Computational grid M axes were 5° west of north, to match the general shoreline trend of the DE Atlantic Coast. Computational grid N axes were 5° north of east to match the approximate angle of the Indian River Inlet and establish normal M and N axes. Tidally driven flow in and out of the Delaware Bay was considered to affect the hydrodynamics in vicinity of the Indian River Inlet, as preliminary testing indicated, motivating the northern extent of the FLOW domain. The use of buoy 44009 wave data for WAVE simulation boundary conditions motivated the eastward extent of the FLOW domain. Computational grid refinement was applied in bands along the M and N axes to limit computation time. Grid resolution studies were undertaken to determine the impact of grid resolution and the location of refinement bands on results. Water level and velocity data were quantitatively compared through Willmott skill score calculations with Eulerian ADCP data collected within 1,400 m of the Indian River Inlet. Willmott skill score differences greater than 0.05 for multiple measurements were considered as important. The grid resolution scheme selected

stepped between approximately 21 m by 21 m near the inlet to 367 m by 367 m in the corners (Figure 28b).

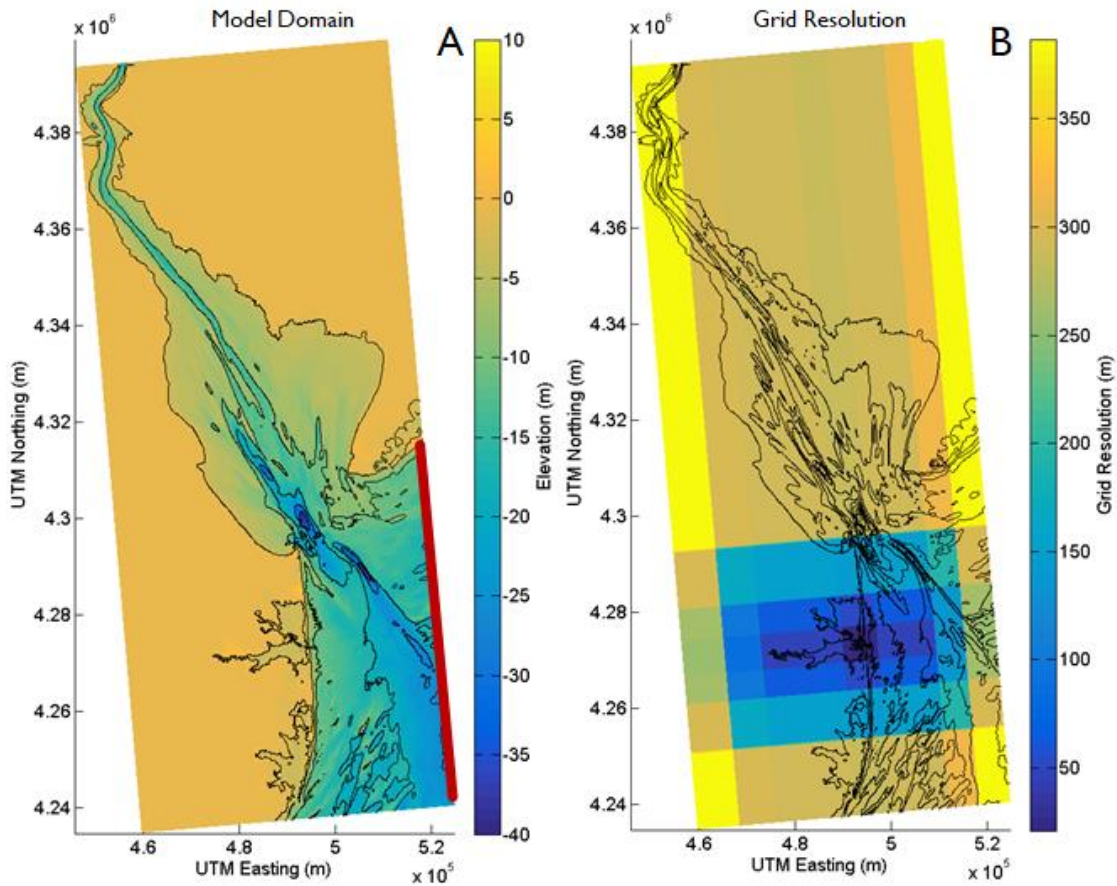


Figure 28: A) Model domain and bathymetry. Color displays elevation. The red edge indicates the location of the FLOW boundary conditions. B) Model computational grid resolution. Average M and N direction grid spacing is indicated by color.

Simulation input bathymetry was originally gathered from the NOAA Digital Elevation Model (DEM) compiled of the areas affected by Hurricane Sandy ([ngdc.noaa.gov/mgg/inundation/sandy/sandy\\_geoc.html](http://ngdc.noaa.gov/mgg/inundation/sandy/sandy_geoc.html)). Several errors in the

compilation of the NOAA DEM were discovered near the Indian River Inlet motivating the consideration of other bathymetry options. An insert along the Delaware Atlantic coast from the modelling effort of Keshtpoor et al. (2015) was found to better match elevation measurements in the study area. Validation scores near the shore clearly indicated that one of the new options was necessary however were similar between the two. Given the sharp discontinuity the LIDAR bathymetry introduced in the shoreline not far north of the study site, the insert which spanned the majority of the Delaware Atlantic coast from Keshtpoor et al. (2015) was selected.

### **5.1.2 Delft3D-FLOW Boundary Conditions**

Tidal hydrodynamics were simulated using water level boundary conditions at the offshore boundary. The offshore boundary water level was specified with an astronomic forcing type by providing tidal harmonic constituents. The five largest tidal harmonic constituents in the study area (M2, S2, N2, K1, and O1) were specified. Tested boundary condition options ranged between measured tidal harmonic constituents at one or two points and modeled tidal harmonic constituents at seven points specified along the offshore boundary. Tidal harmonic boundary condition segments interpolated data between the values at the end points, with single boundaries of measured data and multi-segmented boundaries of modeled data. Measured tidal harmonic constituents were taken from near the center of the southern end of the domain, at Ocean City, MD, and near the northeast corner at Wildwood, NJ. Tidal harmonic constituents at the two measurement locations are similar, yielding small differences in the hydrodynamic predictions between the one and two point options. Modeled tidal harmonic constituents, taken from the ADCIRC 2015 tidal

harmonic constituent database, were applied at seven points forming eight boundary sections (Table 2).

Table 2: Tidal harmonic constituents from ADCIRC 2015 database applied at boundary sections in Delft3D-FLOW simulations.

UTM Northing (m)	Trait	M2	S2	N2	K1	O1
4313248	Amplitude (m)	0.521	0.095	0.118	0.089	0.077
4313248	Phase (°)	0	0	340	179	185
4311228	Amplitude (m)	0.528	0.096	0.120	0.090	0.077
4311228	Phase (°)	0	0	341	179	185
4309206	Amplitude (m)	0.566	0.102	0.127	0.092	0.079
4309206	Phase (°)	0	0	341	180	183
4295359	Amplitude (m)	0.588	0.107	0.131	0.093	0.081
4295359	Phase (°)	358	0	340	180	182
4278582	Amplitude (m)	0.589	0.107	0.131	0.093	0.081
4278582	Phase (°)	358	0	339	180	181
4274763	Amplitude (m)	0.589	0.107	0.132	0.093	0.081
4274763	Phase (°)	357	0	338	180	181
4262208	Amplitude (m)	0.590	0.107	0.132	0.094	0.081
4262208	Phase (°)	357	0	338	180	180

Simulations using boundary measured tidal harmonic constituents at two points and modeled constituents at seven points yielded similar validation scores. While the one and eight segment boundary options had the similar results the inclusion of variation along the more than 70 km boundary was considered beneficial resulting in the selection of the more numerous modeled constituents. The ADCIRC database provided constituent phase information relative to Greenwich Mean Time (GMT), so the simulations were conducted at Coordinated Universal Time (UTC) 0. The southern boundary was not forced due to timing constraints, initial errors in the application of a Neumann condition, and the limited benefits expected more than 40 km from the boundary.

## 5.2 Wave Forcing Component of Simulations with Coupled Delft3D-FLOW/WAVE

Delft3D-Wave simulates the evolution of random, short-crested wind-generated waves primarily in locations such as estuaries, tidal inlets, and lakes (Delft Hydraulics, 2014b). Wave computations are performed with the third-generation Simulating WAVes Nearshore (SWAN) model using the discrete spectral action balance equation. The effect of flow on waves and of waves on flow are simulated through the online coupling of Delft3D-FLOW and Delft3D-WAVE. In this study, the Delft3D-WAVE simulations of waves, forced by offshore wave spectra, dynamically interacted with the hydrodynamics resulting from offshore tidal forcing in coupled online 2DH FLOW/WAVE simulations.

Wave module configuration decisions were generally made based on visual comparisons of results, expectations of the study site, and parameters dictated by the dynamic coupling with Delft3D-FLOW. Wave simulations received and modified water level and current data at 60 minute intervals. Wave computations were run in non-stationary mode, with a coupling interval of 60 minutes and a time step of 5 minutes. Simulations using the stationary computational mode severely underpredicted wave height near the coast which was likely a result of the large domain. Non-stationary computational mode time steps were varied between 1 and 10 minutes without a substantial change in wave property validation scores. Simulations also wrote and used 'hotstart' files to read conditions from the previous prediction, as the default option excluding 'hotstart' files severely underpredicted wave heights away from the boundary. Non-linear triad interactions (LTA) were applied due to the assumed complexity of the wave field in the vicinity of the inlet. The non-linear triad interactions (LTA) used default *Alpha* and *Beta* values.

### **5.2.1 Delft3D-WAVE Computational Grid**

The wave simulation domain spanned from near buoy 44009 to upstream in the Delaware River (Figure 29a). The southeast corner of the domain was specified by the location of buoy 44009. The northwestern corner of the domain was specified by a distance along the Delaware River at which erroneous wave reflections off of an artificial boundary were limited. The domains used in the FLOW and WAVE modules were similar, but not the same, with the most notable differences in the domain extent to the north. Wave boundary conditions were specified along the offshore boundary using conditions from the southeast corner of the domain. Wave simulations used a nested scheme of computational grids. A fairly narrow insert at a finer resolution along the coast on either side of the Indian River Inlet was nested within a coarser grid of the entire domain. Offshore boundary conditions were applied to the edge of the coarse grid and the predictions from the coarse grid along the edge of the insert provided boundary conditions for the finer grid. The nested insert included the shoreline more than 10 km north and 10 km south of the inlet and extended more than 6 km offshore (Figure 30a). Computational grids were angled such that M and N indices increased at 5° west of north and 5° north of east. Grids were refined in M and N index bands. Grid resolutions in the outer grid ranged from approximately 420 m by 420 m to 140 by 140 m near the inlet (Figure 29b). Grid resolutions in the nested grid ranged from approximately 50 m by 50 m to 13 m by 13 m (Figure 30b). Wave simulation bathymetry used the combination of NOAA DEM data and the Delaware Atlantic coast insert from the modelling effort of Keshtpoor et al. (2015).

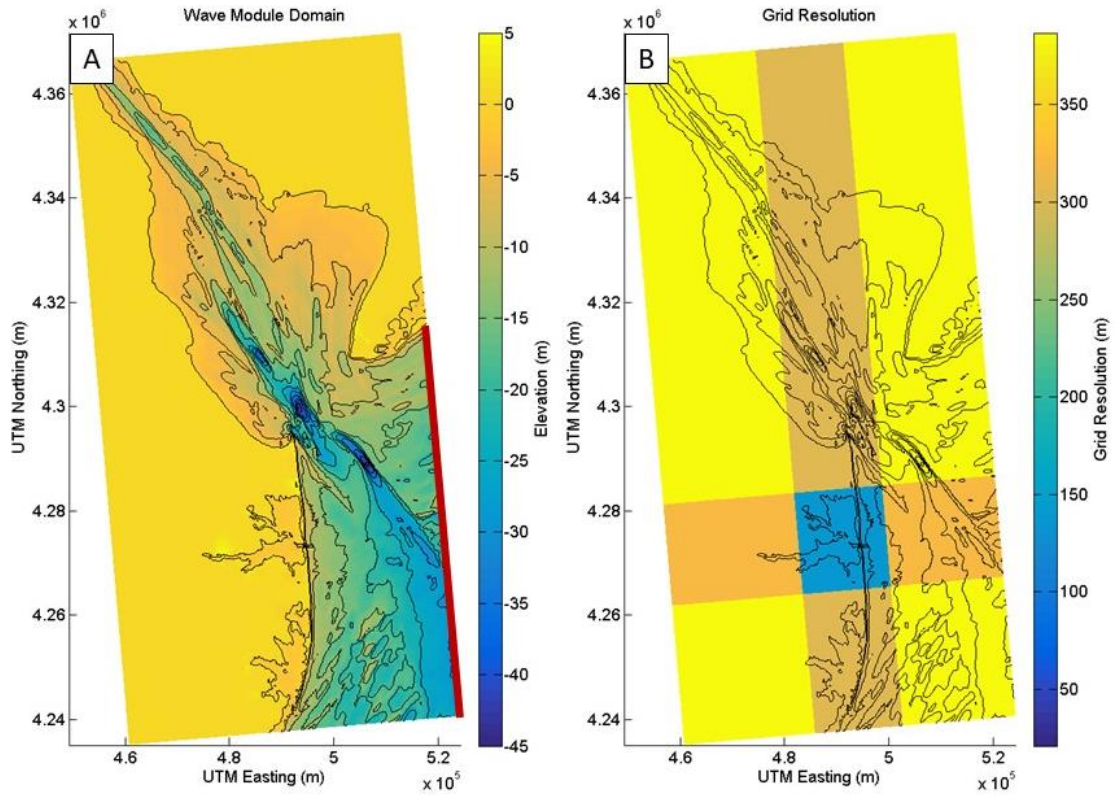


Figure 29: Wave module outer grid domain and bathymetry. Color displays elevation. The red edge indicates the location of the WAVE boundary conditions. B) Wave module outer computational grid resolution. Average M and N direction grid spacing is indicated by color.

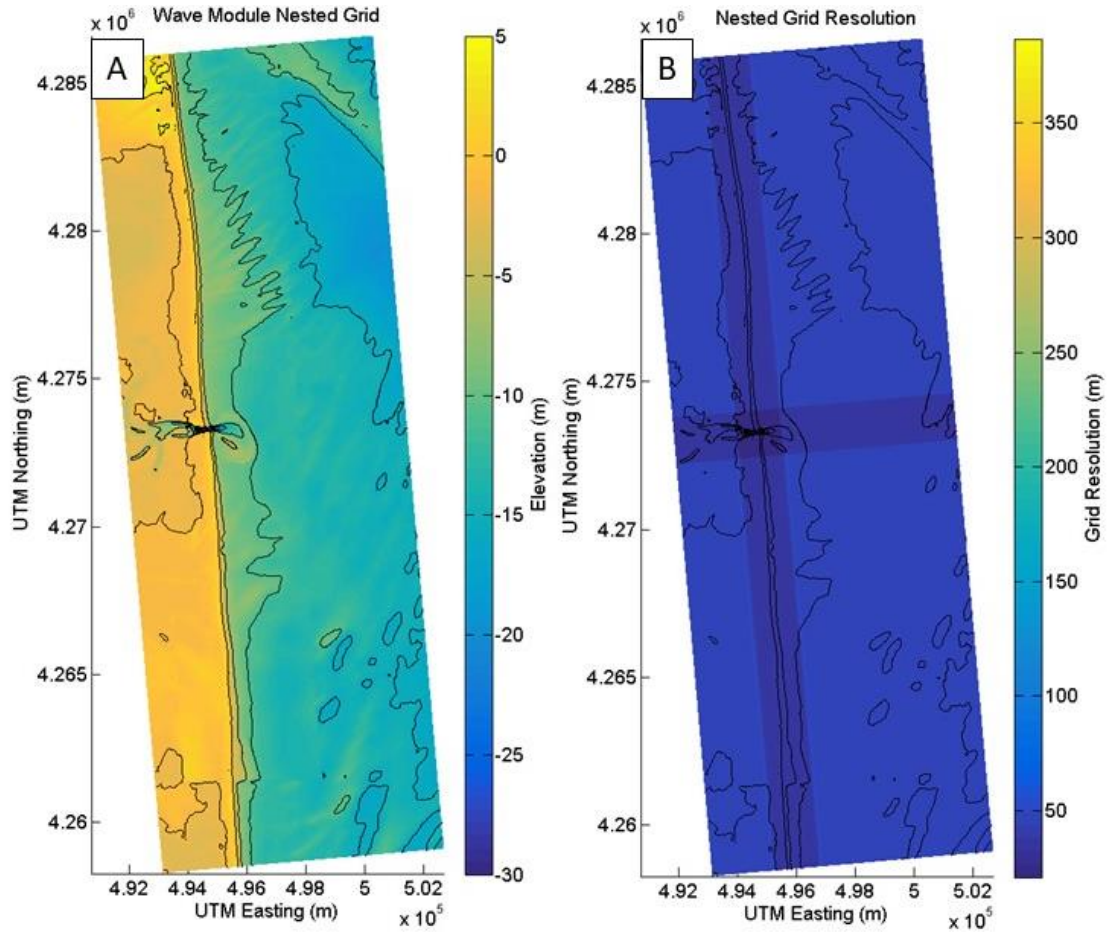


Figure 30: Wave module inner grid domain and bathymetry. Color displays elevation. B) Wave module insert computational grid resolution. Average M and N direction grid spacing is indicated by color.

### 5.2.2 Delft3D-WAVE Boundary Conditions

Wave simulations were forced with offshore wave spectra, specifying time series of significant wave height ( $H_s$ ), peak period ( $T_p$ ), and wave direction ( $\theta$ ) for a JONSWAP wave spectra. Boundary conditions were applied uniformly along the offshore boundary each hour. Wave spectral information was specified using data from the NOAA NBDC buoy 44009 located near the southeast corner of the domain. Boundary conditions for days without data from buoy 44009 were specified from

WAVEWATCH III simulated spectra at the same location. Boundary conditions were specified in ‘wavecon’ files with columns of  $H_s$ ,  $T_p$ , and  $\theta$ , written specifically for each simulation. The default directional spreading value of  $4^\circ$  was specified in the ‘wavecon’ file. Wind effects were not considered in these simulations, so wind speed and direction were specified as 0 in ‘wavecon’ files. Water level conditions were taken from the dynamically coupled Delft3D-FLOW simulations, so a value of 0 was used within ‘wavecon’ files.

### 5.3 Numerical Model Setup Validation

The validation of predicted hydrodynamics was undertaken through the quantitative comparison of data time series collected at nine sites within 1400 m north of the inlet. Simulated water level, easting velocity, northing velocity, significant wave height, peak period, and wave direction were compared with measured Aquadopp data to quantify model skill. Four months of Aquadopp data were collected between 10/26/2013 and 12/05/2014, which was approximately eighteen months before the first drifter field experiment. Predictions were validated by calculating Willmott skill scores between model simulated hydrodynamics and measurements at the same locations.

#### 5.3.1 Willmott Skill Score

Numerical model simulation skill may be quantitatively assessed by a variety of means including root mean square error, the coefficient of determination, and Willmott skill score. While root mean square errors are common indicators of prediction skill they are dimensioned and thus are only meaningful with additional information. Among the non-dimensional model skill indicators both the coefficient of determination ( $r^2$ ) and the original Willmott skill score ( $d$ ) range from 0 to 1, quantifying the relative importance of errors in model predictions. Willmott skill score is argued to better reflect changes in the mean values and certain changes in proportionality than the  $r^2$  statistic (Willmott, 1981). The Willmott skill score, or index of agreement, is defined as a relationship between predicted and observed individual values (i.e.  $P_i$  and  $O_i$ ) and the observed mean ( $\bar{O}$ ), and may be expressed as,

$$d = 1 - \frac{\sum_{i=1}^N (P_i - O_i)^2}{\sum_{i=1}^N (|P_i - \bar{O}| + |O_i - \bar{O}|)^2} \quad (3)$$

The coefficient of determination is composed of the same variables, varies over the same and range, and is also defined as by a subtraction from one. The  $r^2$  statistic may be expressed as,

$$r^2 = 1 - \frac{\sum_{i=1}^N (P_i - O_i)^2}{\sum_{i=1}^N (O_i - \bar{O})^2} \quad (4)$$

The Willmott skill score has a similar form to the  $r^2$  statistic, however includes an additional term for the difference between individual predictions ( $P_i$ ) and the observed mean ( $\bar{O}$ ) in the denominator. As the Willmott score contains an additional term which cannot be negative in the denominator it is necessarily smaller for non-trivial differences between predictions and observations. Updated indices of agreement have been published, to better address models that generally perform well (Willmott et al., 2012). The refined index of agreement ( $d_r$ ) is also a function of predicted and observed individual values ( $P_i$  and  $O_i$ ) and the observed mean ( $\bar{O}$ ), and may be expressed as,

$$d_r = \left\{ \begin{array}{l} 1 - \frac{\sum_{i=1}^N |P_i - O_i|}{2 \sum_{i=1}^N |O_i - \bar{O}|} \quad \text{when } \sum_{i=1}^N |P_i - O_i| \leq 2 \sum_{i=1}^N |O_i - \bar{O}| \\ \frac{2 \sum_{i=1}^N |O_i - \bar{O}|}{\sum_{i=1}^N |P_i - O_i|} - 1 \quad \text{when } \sum_{i=1}^N |P_i - O_i| > 2 \sum_{i=1}^N |O_i - \bar{O}| \end{array} \right\} \quad (5)$$

The coefficient of determination ( $r^2$ ) and index of agreement ( $d$ ) range between 0 and 1. The refined index of agreement ( $d_r$ ) varies over a larger range, spanning -1 to 1. While the subsequent indices of agreement approach 1 more slowly, the original index of agreement is more commonly cited, and may be more useful for comparisons with other modelling efforts. Validation of hydrodynamic predictions to the north of the Indian River Inlet was primarily addressed with the original Willmott skill score ( $d$ ) for the purposes of comparisons with other model simulations, however, the

refined index of agreement ( $d_r$ ) was also calculated to better compare results between hydrodynamic properties and locations within the study site.

### 5.3.2 Simulation Willmott Skill Scores

The hydrodynamics during four of the Aquadopp deployments presented in DiCosmo (2015) were predicted using a dynamically coupled Delft3D-FLOW/WAVE simulation. Willmott skill scores were calculated for water level ( $h$ ), easting velocity ( $u$ ), northing velocity ( $v$ ), significant wave height ( $H_s$ ), peak period ( $T_p$ ), and mean wave direction ( $\theta$ ) between simulation predictions and measurements (Table 3). The refined index of agreement was also computed between hydrodynamic predictions and measurements (Table 4). Water levels were predicted with a mean index of agreement of 0.937, and a mean refined index of agreement of 0.774. Easting and northing velocities were predicted with mean indices of agreement of 0.521 and 0.548, and mean refined indices of agreement of 0.216 and 0.337 respectively. Significant wave heights, peak period, and mean wave direction were predicted with mean indices of agreement of 0.488, 0.503, and 0.247 as well as mean refined indices of agreement of -0.119, 0.256, and -0.501. Numerical simulations generally predicted water level well, but velocities were predicted with a variety of skills. Wave characteristic predictions were typically worse than water level or velocity predictions, particularly significant wave height and peak period.

Table 3: Willmott skill scores, indices of agreement ( $d$ ), for all hydrodynamic properties and all Aquadopp locations considered.

Site	$h$	$u$	$v$	$H_s$	$T_p$	$\theta$
C1	0.986	0.726	0.731	0.262	0.446	0.517
D1	0.987	0.294	0.667	0.257	0.473	0.387
A2	0.962	0.896	0.736	0.392	0.740	0.246
B2	0.964	0.892	0.291	0.489	0.595	0.231
A4	0.838	0.384	0.336	0.581	0.473	0.080
B4	0.950	0.369	0.551	0.576	0.493	0.200
C4	0.951	0.263	0.362	0.629	0.390	0.174
D4	0.951	0.409	0.573	0.600	0.432	0.192
E4	0.840	0.452	0.688	0.606	0.485	0.194

Table 4: Refined Willmott skill scores, refined indices of agreement ( $d_r$ ), for all hydrodynamic properties and all Aquadopp locations considered.

Site	$h$	$u$	$v$	$H_s$	$T_p$	$\theta$
C1	0.882	0.281	0.357	-0.449	0.204	0.215
D1	0.888	-0.213	0.077	-0.427	0.415	-0.148
A2	0.811	0.521	0.816	0.122	0.643	-0.523
B2	0.816	0.695	-0.084	0.085	0.347	-0.234
A4	0.573	0.061	0.173	-0.124	0.204	-0.887
B4	0.806	-0.032	0.423	-0.149	0.215	-0.735
C4	0.807	0.304	0.205	0.080	-0.122	-0.779
D4	0.807	0.189	0.495	-0.105	0.133	-0.7191
E4	0.576	0.136	0.569	-0.105	0.269	-0.698

Water levels are generally predicted well. Skill variation by location was generally small, with the exceptions of sites A4 and E4. Within each Aquadopp array neither measurements nor model predictions varied substantially with location (Figure 31a, Figure 32a, Figure 33a). Simulated water levels typically reproduced phasing information well. Prediction errors were most often related to tidal range, with simulated tidal ranges tending to be larger. Water level refined indices of agreement were 0.102, 0.150, and 0.192 smaller than indices of agreement for Aquadopp arrays one, two, and four respectively. The relative similarity between the skill scores

considering the extended lower limit and more gradual approach to 1 indicates that water level is well predicted in the simulations of hydrodynamics near the Indian River Inlet.

Aquadopp array one predicted northing velocities reasonably well, with decent to poor easting velocity prediction skills. The first Aquadopp array was located between approximately 60 m and 100 m north, 50 m west, and 25 m east of the north jetty tip. Easting velocities were relatively well predicted at site C1 but were poorly predicted at site D1 (Figure 31b, Figure 31c). Model simulations of hydrodynamics during the deployment of Aquadopp array one generally overpredicted easting velocity magnitude. Between the early rising tide and early falling tide Site C1 predicted the sign of easting velocity well but overpredicted easting velocity magnitude. Measurements between the early rising and early falling tide indicate a substantial easting velocity gradient, over the approximately 86 m between sites C1 and D1 (Figure 31b). Measured velocities at site D1 were typically to the east between the middle of the rising tides and the early falling tides. The model predicted easting velocities at site D1 between the early rising and early falling tides to be similar to those at site C1, which were to the west. Between the early falling and early rising tides easting velocity was generally well predicted at both sites C1 and D1. Northing velocity  $d$  values were typically decent, however,  $d_r$  values were 0.445 and 0.507 lower at sites C1 and D1. Northing velocity predictions at sites C1 and D1 generally capture the flow direction however generally overestimate northing velocities between early rising and early falling tides (Figure 31c). Northing velocity magnitude at site D1 was overpredicted by a factor of two or three between the early rising and early falling tides.

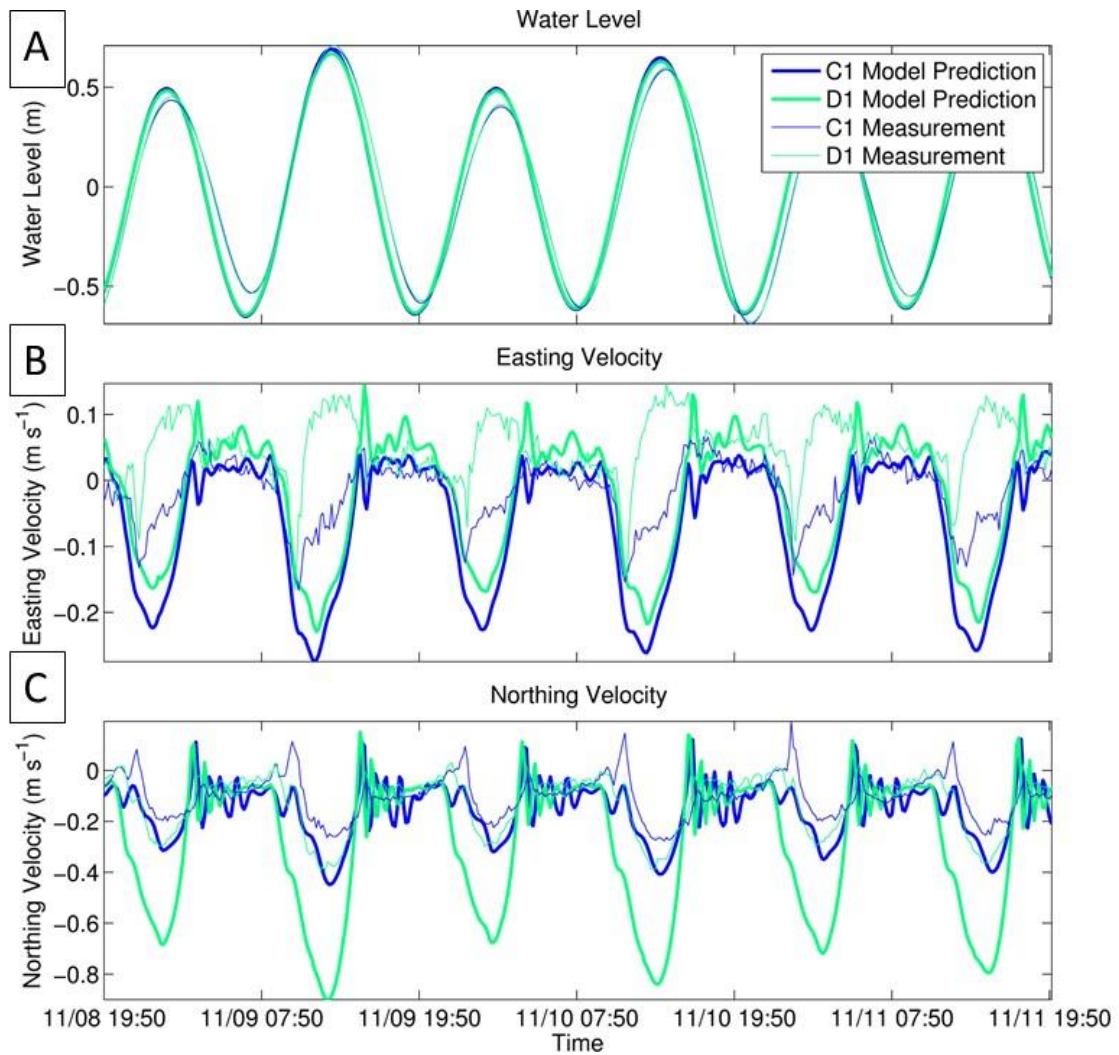


Figure 31: A) Measured Aquadopp water levels from sites C1 and D1 compared with model predicted water levels at the same locations. B) Measured Aquadopp easting velocities from sites C1 and D1 compared with model predicted easting velocities at the same locations. C) Measured Aquadopp northing velocities from sites C1 and D1 compared with model predicted easting velocities at the same locations. Color indicates Aquadopp site, line width indicates data type (i.e. simulation and measurement).

Velocities prediction skill scores for the second Aquadopp array varied substantially with direction and location. The second Aquadopp array was located

between approximately 60 m and 80 m north, 5 m west, and 180 m east of the north jetty tip. A2 predicts easting velocity well, though often overpredicts velocities in the latter half of the rising tide and under-predicts the rapid and shift east and back measured in the early ebbing tide (Figure 32b). Between the early rising and early falling tides Aquadopps measured a substantial easting velocity gradient over the approximately 187 m between sites A2 and B2. The easting velocity predictions at site B2 between the early rising and early falling tides were similar to those at A2 resulting in a substantially under-predicted easting velocity gradient between sites A2 and B2. The under-predicted easting velocity gradient were similar between both Aquadopp array one and two. Northing velocity was predicted with a decent skill score at both sites A2 and B2 (Figure 32c). The model severely overpredicts the northing velocity gradient between sites A2 and B2, with similar measurements at both sites but northing velocity magnitude overpredicted by at least a factor of two during the early rising to late falling tides at site B2. Velocity prediction errors were similar at sites D1 and B2. Sites C1 and A2 were approximately 25 m and 180 m east of the jetty tip, while site D1 and B2 were located approximately 50 m and 5 m west of the jetty tip. The failure to capture the large easting velocity gradient and the erroneous introduction of a large northing velocity gradient at the two sites landward of the north jetty tip and within 100 m of the inlet may be related to the representation of the jetty within the simulation.

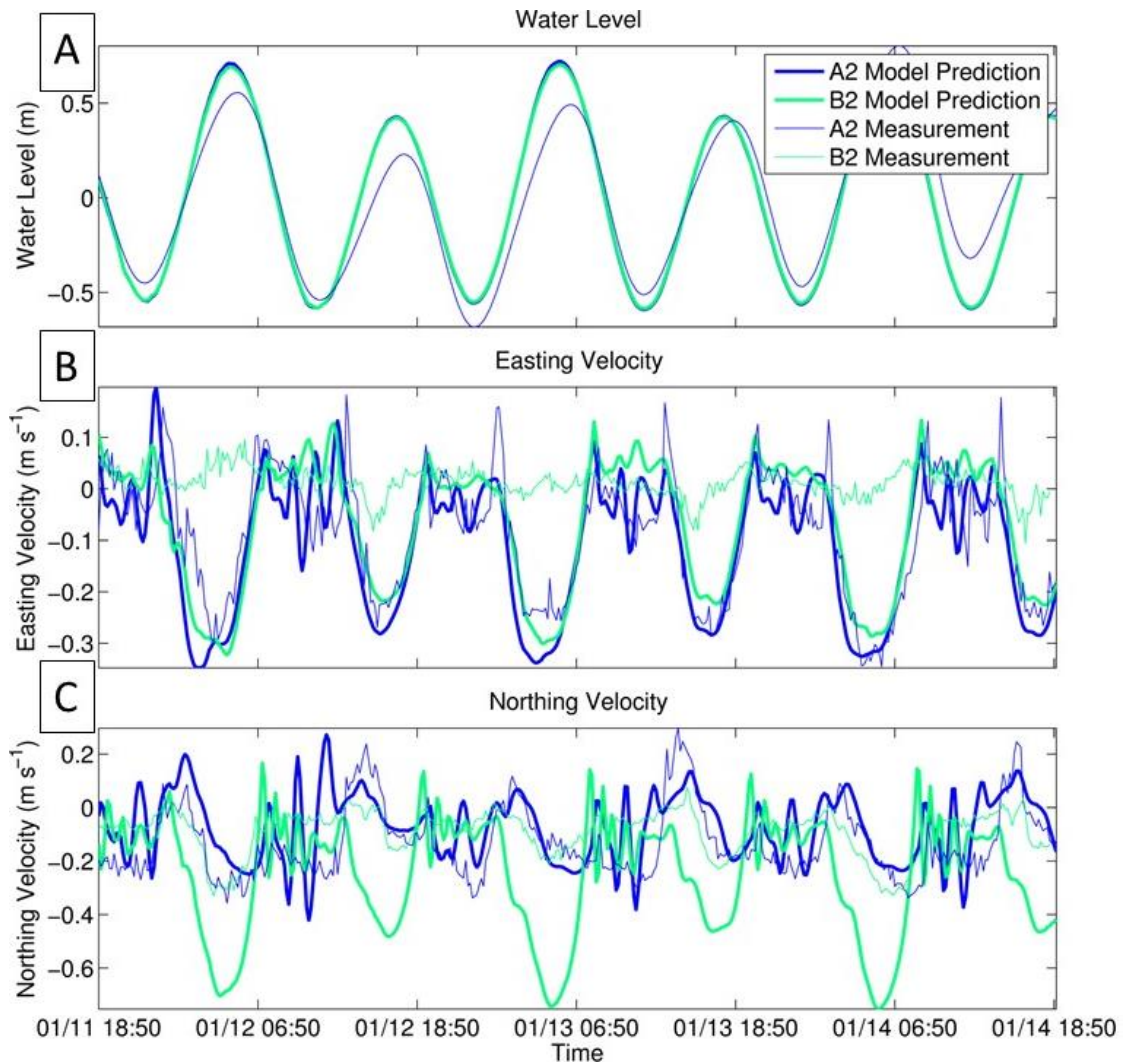


Figure 32: A) Measured Aquadopp water levels from sites A2 and B2 compared with model predicted water levels at the same locations. B) Measured Aquadopp easting velocities from sites A2 and B2 compared with model predicted easting velocities at the same locations. C) Measured Aquadopp northing velocities from sites A2 and B2 compared with model predicted northing velocities at the same locations. Color indicates Aquadopp site, line width indicates data type (i.e. simulation and measurement).

Prediction skill scores for the fourth Aquadopp array are generally poor for easting velocities, but improve for northing velocities. The fourth Aquadopp array, was located between approximately 400 m to 1400 m north, and 130 m to 260 m west, of the north jetty tip. Simulations predicted easting velocity poorly at all sites in Aquadopp array four. Easting velocity is generally underpredicted at all sites in Aquadopp array four, with predicted direction often incorrect at A4 and E4 near high tide (Figure 33b). Predictions did not capture the dominant timescale of variation for easting velocities in Aquadopp array four, with predictions generally varying at a tidal frequency and measurements fluctuating at substantially smaller timescales. Model simulated velocities at all Aquadopps tended to under-predict velocity fluctuations at brief timescales, yielding the poor easting velocity skill scores for Aquadopp array four in which easting velocities varied primarily at sub-tidal timescales. Skill scores for simulated northing velocities at Aquadopp array four were higher, with predictions often similar to measurements (Figure 33c). The largest source of error in northing velocity predictions at Aquadopp array four coincides with predicted significant wave heights greater than 1 m between 11/17 18:50 and 11/18 06:50. Following a sharp decline in predicted significant wave height values, predicted northing velocities were similar to measurements with little spatial variation in either.

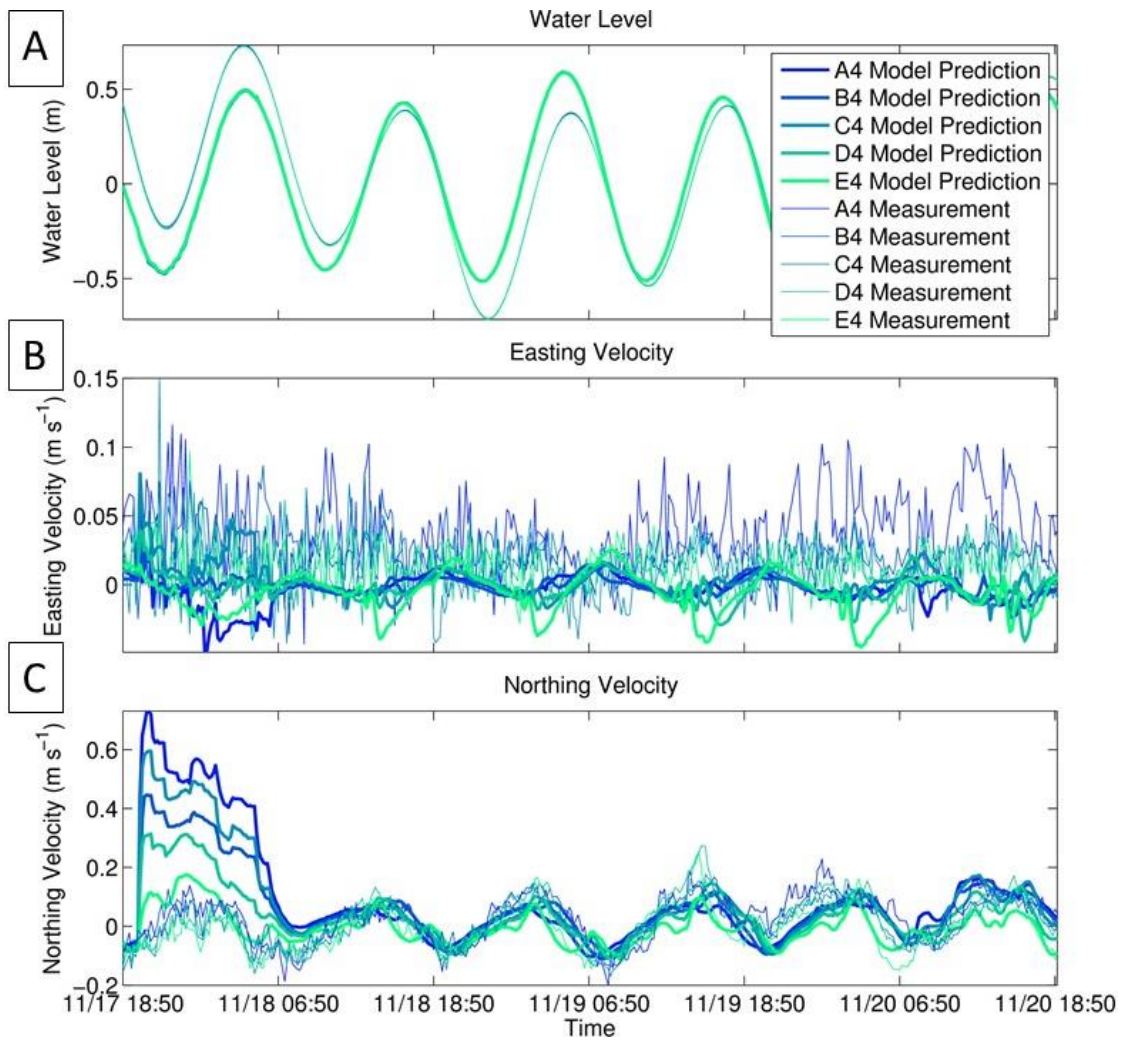


Figure 33: A) Measured Aquadopp water levels from sites A4, B4, C4, D4, and E4 compared with model predicted water levels at the same locations. B) Measured Aquadopp easting velocities from sites A4, B4, C4, D4, and E4 compared with model predicted easting velocities at the same locations. C) Measured Aquadopp northing velocities from sites A4, B4, C4, D4, and E4 compared with model predicted northing velocities at the same locations. Color indicates Aquadopp site, line width indicates data type (i.e. simulation and measurement).

Wave predictions generally did not match measured values well. While easting and northing velocity predictions have a combined mean index of agreement of 0.534,

wave characteristics only have a mean score of 0.413. The difference in velocity and wave prediction skill is more apparent in a refined index of agreement comparison. Mean northing and easting velocity refined indices of agreement are 0.276 while mean wave property refined indices of agreement are -0.121. The relatively poor predictive capabilities of the wave simulations are evident in time series comparisons of simulated and measured significant wave heights, wave peak periods, and mean wave directions (Figure 34, Figure 35, Figure 36). While not necessarily apparent in visual time series comparisons, peak period prediction skill scores were similar to easting velocity predictions, even achieving a greater mean refined index of agreement.

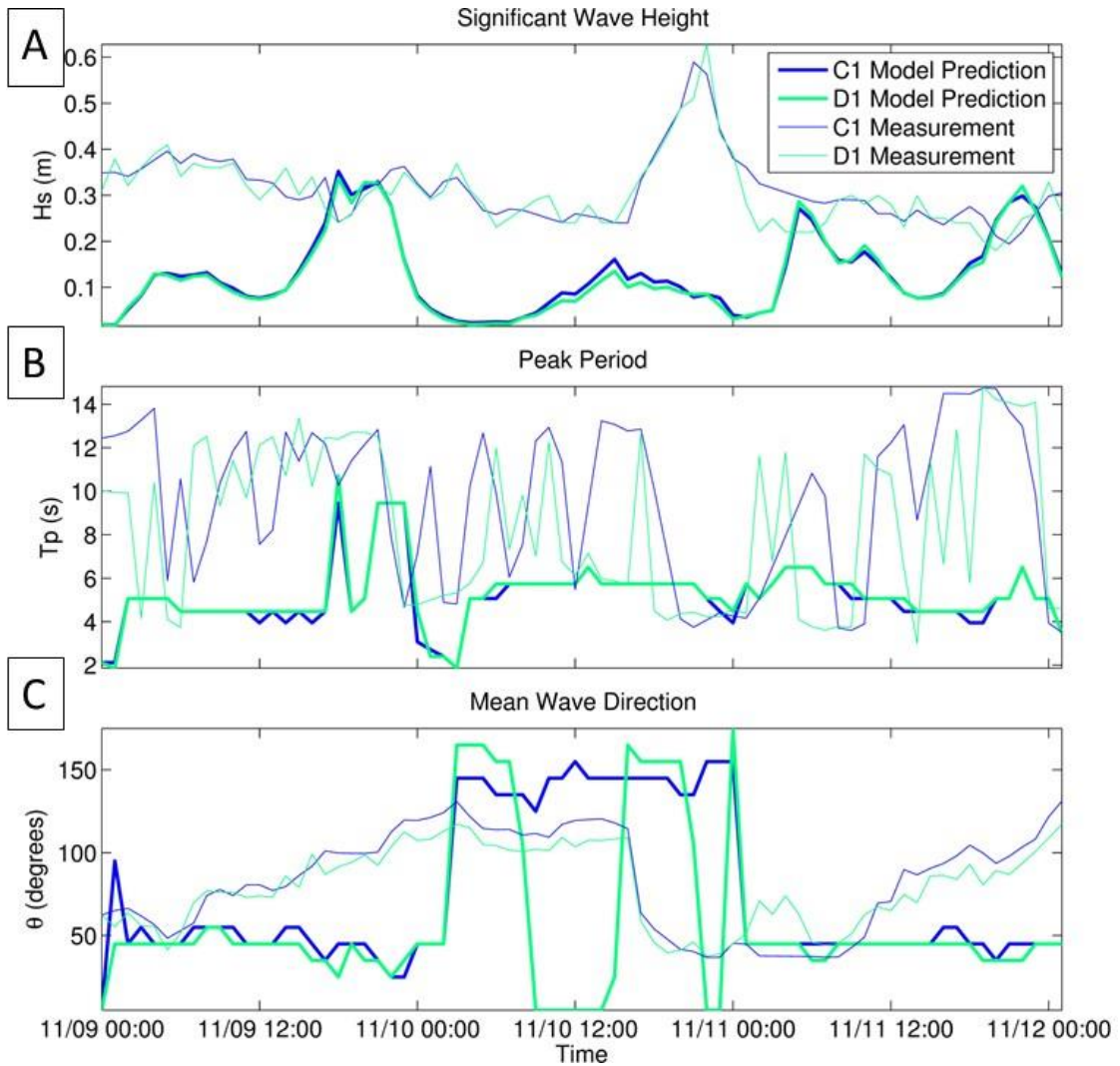


Figure 36: A) Measured Aquadopp significant wave heights from sites C1 and D1 compared with model predicted significant wave heights at the same locations. B) Measured Aquadopp wave peak periods from sites C1 and D1 compared with model predicted wave peak periods at the same locations. C) Measured Aquadopp mean wave directions from sites C1 and D1 compared with model predicted mean wave directions at the same locations. Color indicates Aquadopp site, line width indicates data type (i.e. simulation and measurement).

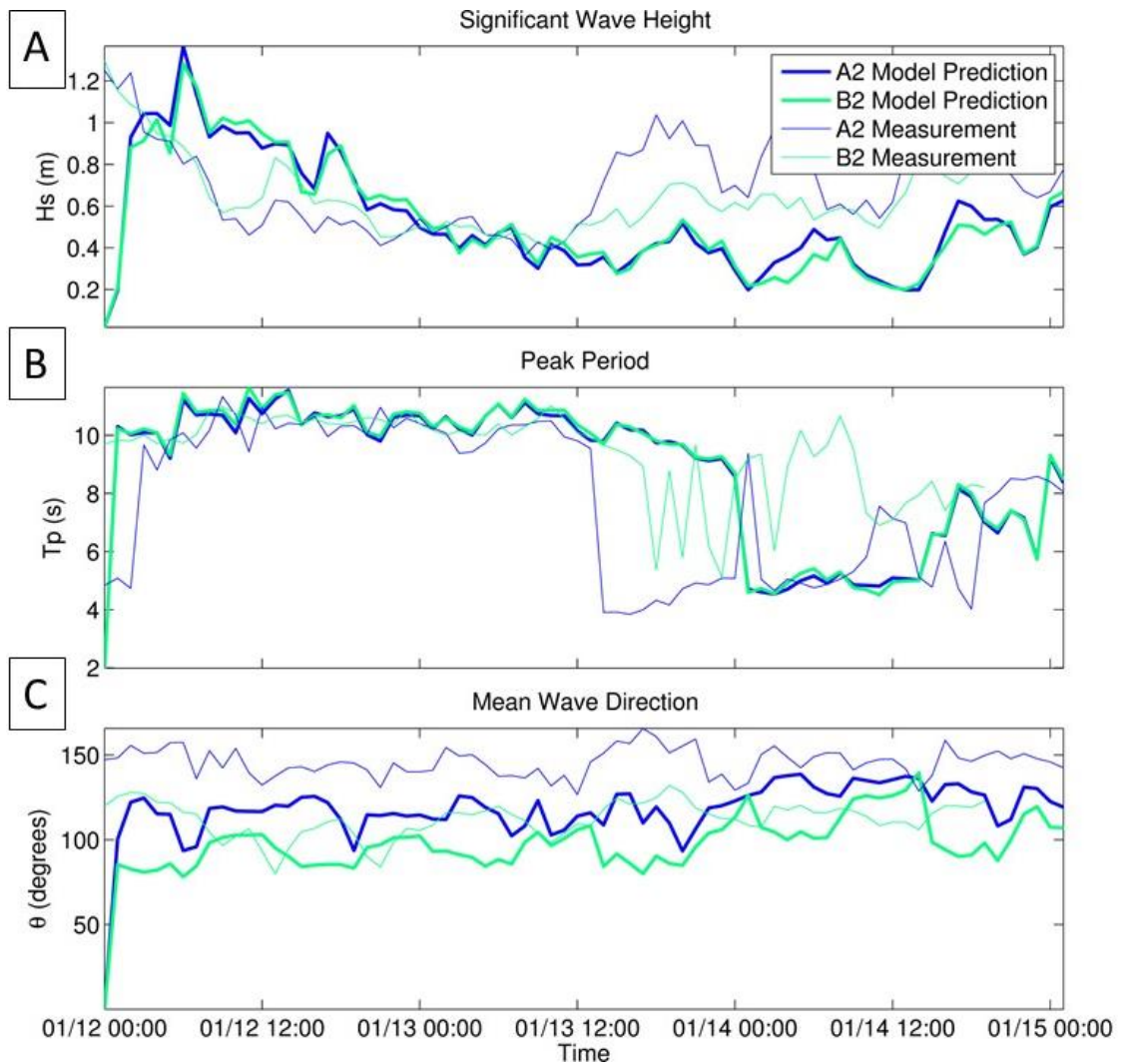


Figure 37: A) Measured Aquadopp significant wave heights from sites A2 and B2 compared with model predicted significant wave heights at the same locations. B) Measured Aquadopp wave peak periods from sites A2 and B2 compared with model predicted wave peak periods at the same locations. C) Measured Aquadopp mean wave directions from sites A2 and B2 compared with model predicted mean wave directions at the same locations. Color indicates Aquadopp site, line width indicates data type (i.e. simulation and measurement).

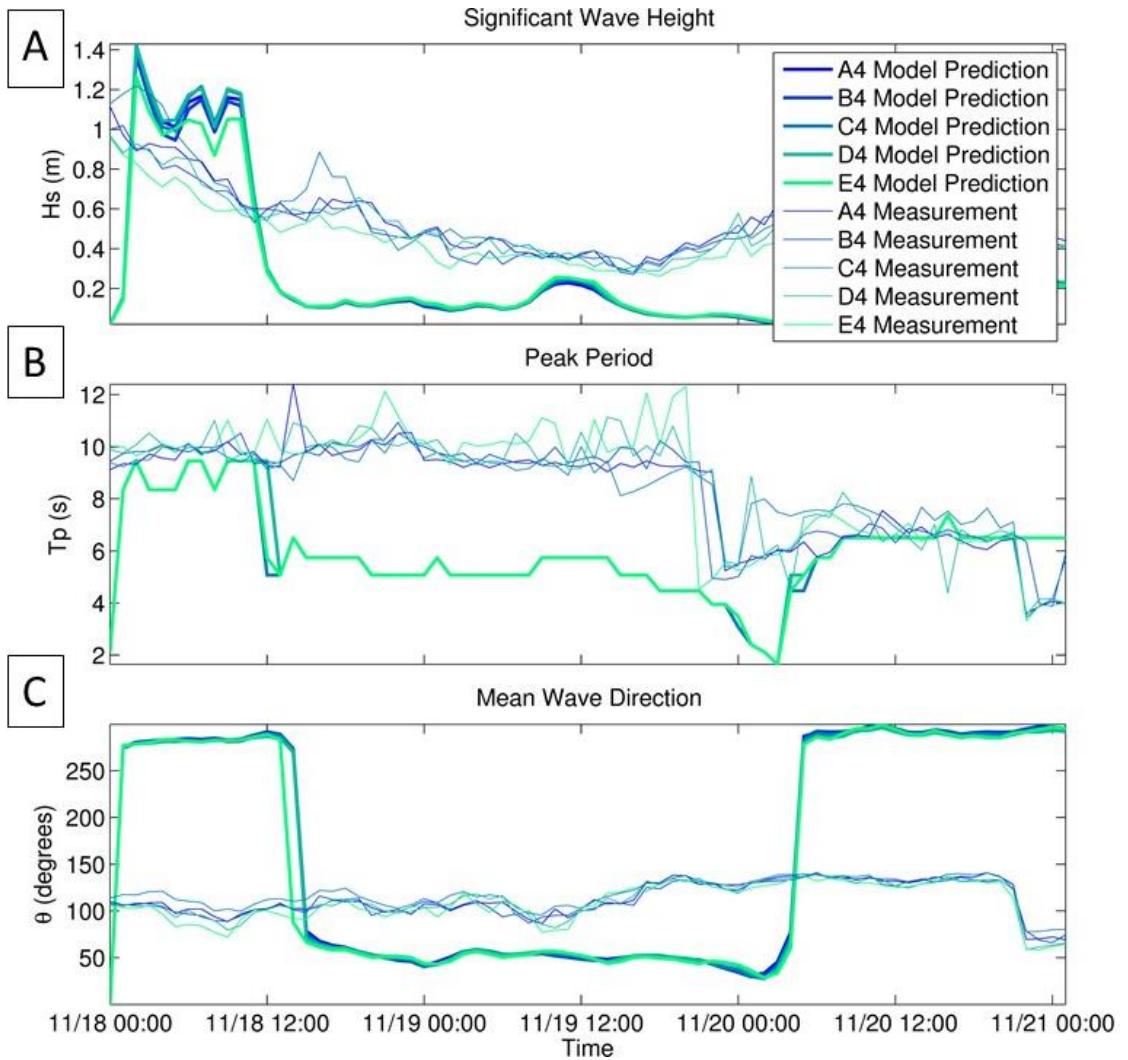


Figure 38: A) Measured Aquadopp significant wave heights A4, B4, C4, D4, and E4 compared with model predicted significant wave heights at the same locations. B) Measured Aquadopp wave peak periods from sites A4, B4, C4, D4, and E4 compared with model predicted wave peak periods at the same locations. C) Measured Aquadopp mean wave directions from sites A4, B4, C4, D4, and E4 compared with model predicted mean wave directions at the same locations. Color indicates Aquadopp site, line width indicates data type (i.e. simulation and measurement).

#### 5.4 Simulated Drifter Tracks

Model simulation velocity spatial variability and current pattern predictive abilities were qualitatively addressed through the comparison of simulated passive tracer paths and observed drifter tracks. Depth averaged hydrodynamics during the drifter field experiments were simulated in Delft3D-FLOW/WAVE with a grid of passive tracers inserted at 5 minute intervals throughout the tidal cycles sampled. Model drifters were collected 30 minutes after release, relating track length to an average of the velocities over the spatiotemporal extent covered. Model drifters were released in grids covering the study area due to the inexact similarities between simulated and observed drifters at most locations. Observed drifter tracks were often more similar to simulated passive tracer paths at different locations making drifter track comparisons more useful with grids of release points. Tidal forcing conditions were simulated for the 16 days prior to the field experiments to ensure a more than adequate model spinup period and capture tidal cycle variations. Dynamic coupling between Delft3D-FLOW and WAVE simulated the wave conditions of the 3 days prior to each field experiment as a wave prediction spinup period.

Simulated drifter tracks were compared to provide examples of predicted flow patterns at various points in the tidal cycle. General comparisons were made using a numerical simulation forced by the tidal wave forcing conditions present during the third field experiment. Simulated flow patterns during the rising tide may be generally described by a circulation cell to the north of the ebb jet in the  $\pi/6$  tidal phase shifting into a widening flow divergence point north of the inlet in the  $3\pi/6$ , and  $5\pi/6$  tidal phases (Figure 37a, Figure 37b, Figure 37c). Model predicted current patterns during the falling tide may be described as changing from entirely inlet directed flow at the

start of the  $7\pi/6$  tidal phase changing to flow southeast and into the ebb jet in the  $9\pi/6$  and  $11\pi/6$  tidal phases (Figure 37d, Figure 37e, Figure 37f).

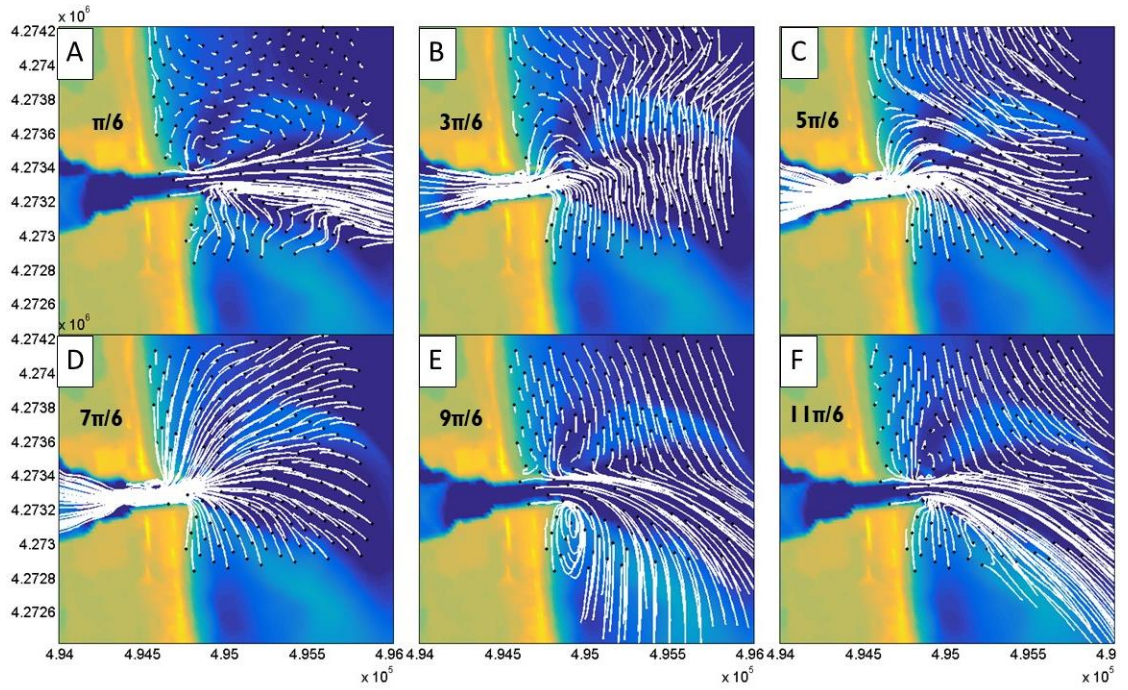


Figure 37: Simulated passive tracer paths over 30 minutes representing drifter track predictions plotted over bathymetry. Release points are presented as dots.

#### 5.4.1 Comparisons of Simulated and Observed Drifter Tracks

Hydrodynamics during the first, second, and third field experiment were simulated with grids of simulated drifters released every 5 minutes throughout the field experiment duration. Simulated drifters were released for 30 minutes. Observed drifter tracks were divided into 30 minute segments for comparisons with simulated results, where track length permitted. Drifter predictions during the third experiment, defined by flow out of the inlet, generally matched observations better than drifter predictions for the first or second field experiment which was defined by flow into the inlet.

Observed drifter tracks from the first field experiment indicate that in small waves (i.e.  $H_s$  of 0.4 m) and a small tidal range, simulations did not predict current patterns well. In the first quarter of the rising tide, the model predicted erroneous current patterns with no simulated drifter tracks within 500 m of observations travelling in similar directions (Figure 38b). Near the middle of the rising tide, simulated drifter tracks near the divergence point matched observed track shapes, however divergence point northing was overpredicted by approximately 200 m to 400 m (Figure 38c, Figure 38d). Drifter measurements and model predictions indicated relatively little current pattern variation throughout the latter half of the rising tide (Figure 38e, Figure 38f). In the early rising tide, observed drifter tracks were similar to those measured in the second half of the rising tide while simulated drifters indicated flow out of the inlet and substantially different flow directions (Figure 38g). Simulated flow patterns did not match observations in the early rising tide. Simulations of the first field experiment generally did not capture the flow features indicated by drifter observations well, however may have indicated similar flow features at incorrectly predicted locations near the middle of the rising tide.

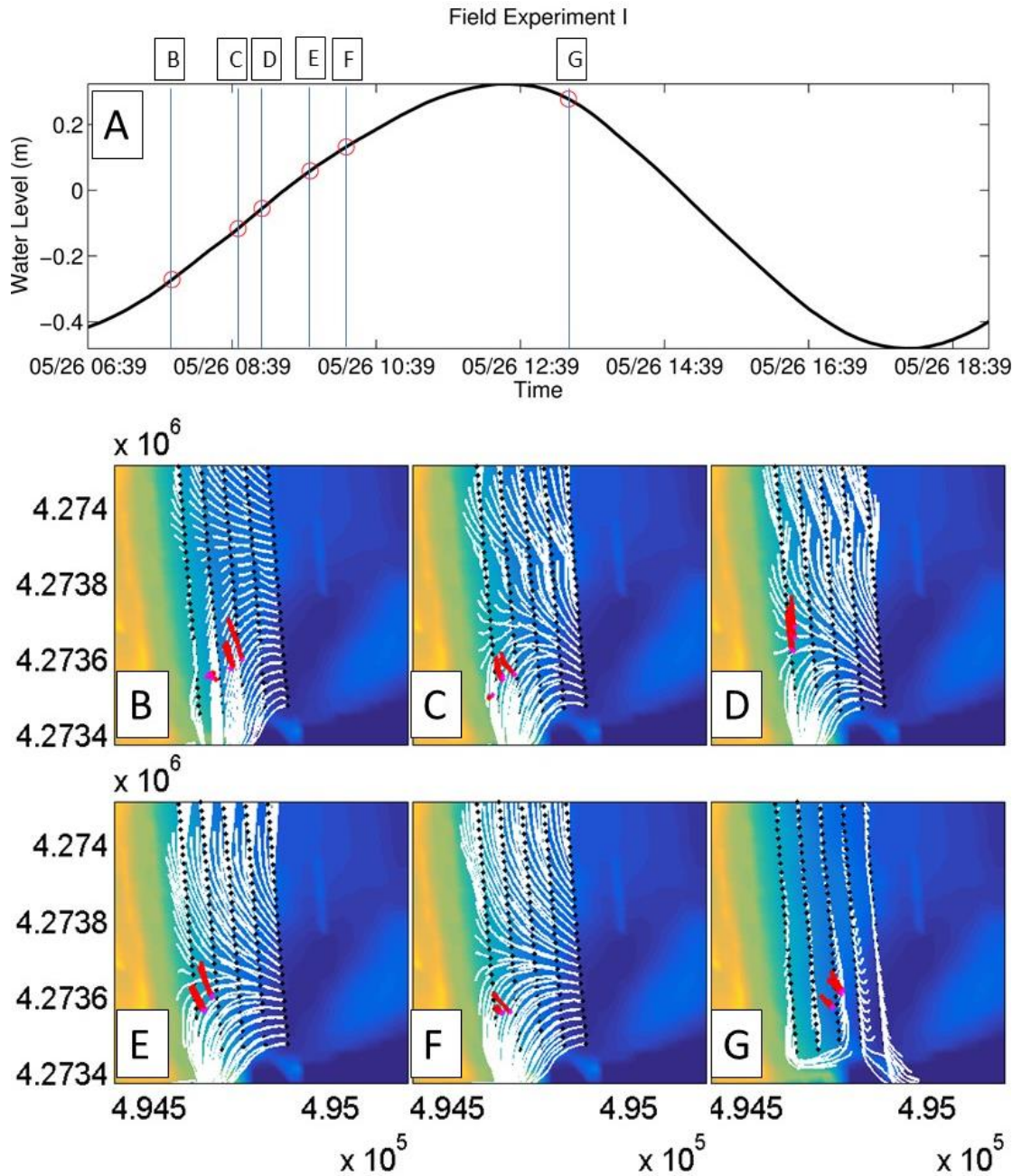


Figure 38: A) Simulated water level within the inlet during the first experiment. Six release times are indicated with 'o' markers and vertical lines. Times are presented in EDT. B,C,D,E,F,G) Simulated (white) and observed (red) drifter releases during the first field experiment. Simulated (black) and observed (magenta) release locations indicated as dots. Simulated drifter release and collection times were 30 minutes apart. Sufficiently long observed drifter tracks were separated into 30 minute segments.

Observed drifter tracks from the second field experiment indicate that in typical waves (i.e.  $H_s$  of 0.5 m) and a large tidal range, the model predicted similar flow features during the middle of the rising tide, with mixed agreement between later in the rising tide and early in the falling tide. Model predicted current patterns during the middle of the rising tide included a flow divergence point between 300 and 400 m north of the inlet, with flow south of the divergence point entering the inlet. During the middle of the rising tide observed drifter tracks less than one hour apart traveled northwest and south into the inlet at different northings, which is likely indicative of a flow divergence point (Figure 39b, Figure 39c, Figure 39d). The path angle of drifter tracks observed travelling north near the middle of the rising tide was similar to model predicted drifter path angle within 100 m north of the flow divergence point. Simulated drifters entering the inlet near the middle of the rising tide generally followed observations, but with drifters travelling over the north jetty, which indicates again that the flow impediment imposed by the jetty may not have been well simulated. The simulation appears to overpredict the northing location of the flow divergence point by approximately 100 m, matching similar observed and simulated tracks which traveled north. By the third quarter of the rising tide, the simulated divergence point had migrated more than 400 m north while the observed data indicate a similar position as during the middle of the rising tide (Figure 39e). The simulation also predicted flow reversal within the inlet while drifters were observed traveling in (Figure 39f). North of the inlet after flow reversal, simulations predicted similar velocity magnitudes but failed to capture direction (Figure 39g). Simulated flow patterns in the second field experiment generally agreed with observations during the

middle of rising tide, but disagreed between the last quarter of the rising tide and first quarter of the ebbing tide.

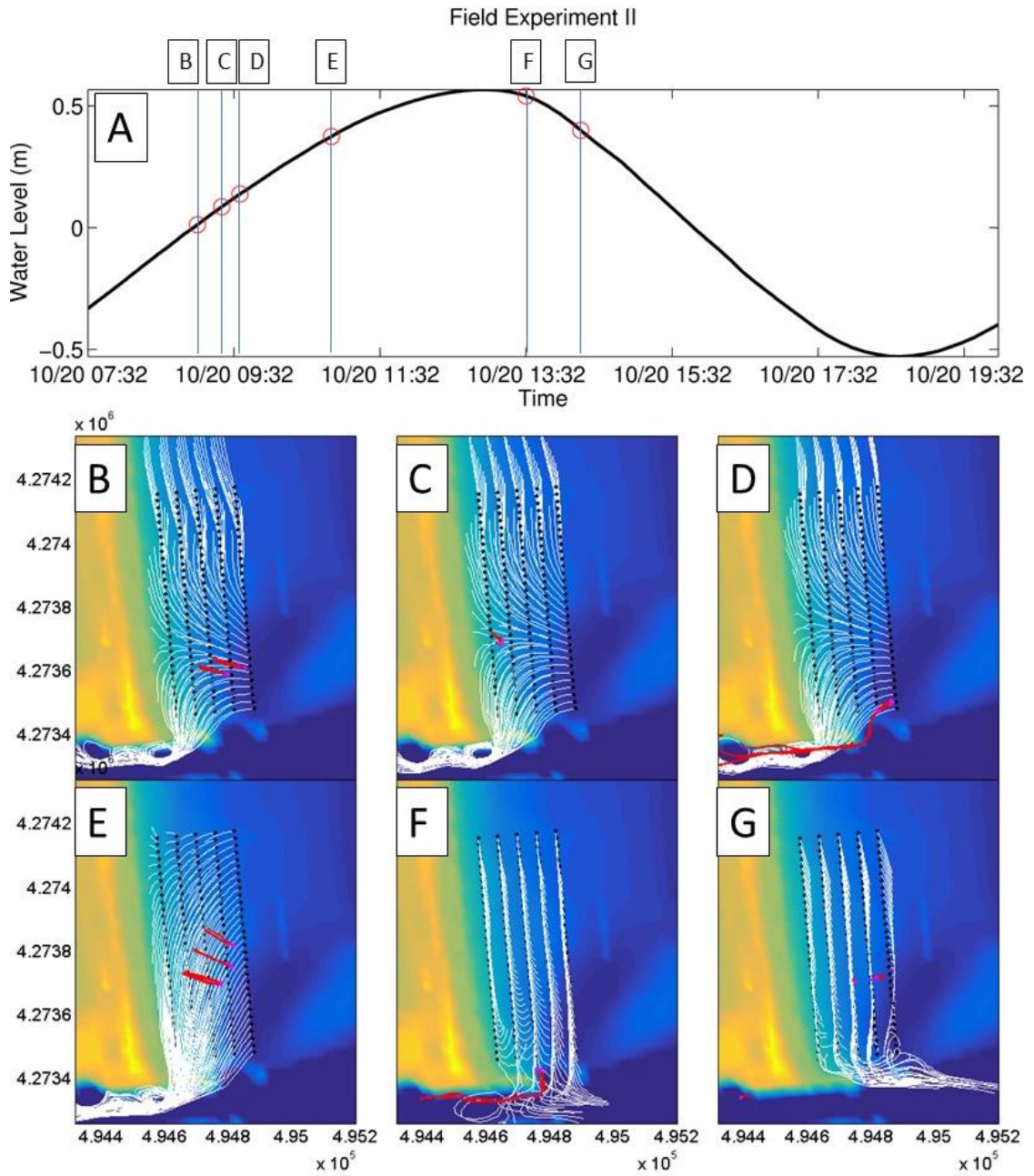


Figure 39: A) Simulated water level in the inlet during the second experiment. Six release times are indicated with ‘o’ markers and vertical lines. Times are presented in EDT. B,C,D,E,F,G) Simulated (white) and observed (red) drifter releases during the second field experiment. Simulated (black) and observed (magenta) release locations indicated as dots. Simulated drifter release and collection times were 30 minutes apart. Sufficiently long observed drifter tracks were separated into 30 minute segments.

Observed drifter tracks from the third field experiment indicate that the model simulations predicted flows with reasonable agreement between the first and third quarters of the falling tide for a typical tidal range and significant wave heights, but introduced circulation cells and divergence points not supported by observations. In the second quarter of the rising tide, model predictions matched observations reasonably well with drifters heading south and into the ebb jet, disagreeing about track angle (Figure 40b). The area of simulated drifters which traveled southeast expanded to match subsequent observations in the second quarter of the falling tide. In the third fourth of the falling tide simulated drifter tracks compared well with observations, matching the path angle of drifters entrained in the ebb jet well (Figure 40d, Figure 40e). During low tide, simulated drifters matched paths of drifters entrained in the ebb jet, but turned east to the north of the inlet while observations indicated a continued flow southeast (Figure 40f). After low tide, simulated drifters matched observed drifters following the ebb jet as it turned north, but the simulation introduced a circulation cell to the north of the inlet in direct contrast to the observed drifters travelling southeast (Figure 40g). Drifter tracks from the third field experiment generally indicate that the ebb jet was well simulated, as were flow patterns north of the inlet over a substantial portion of the falling tide, but that to the north of the inlet near low tide the model introduced erroneous decelerations and direction shifts eastward.

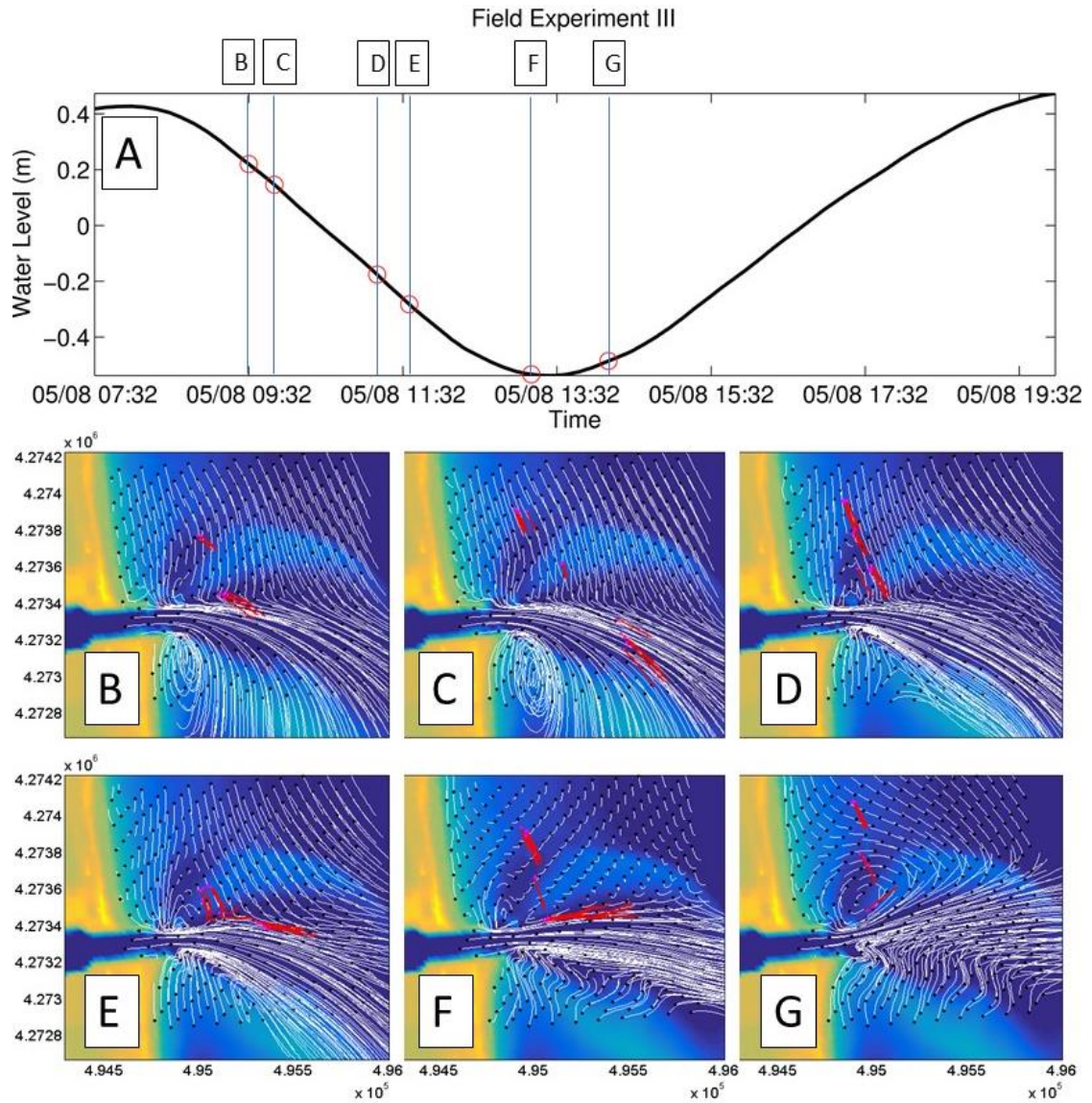


Figure 40: A) Simulated water level within the inlet during the third experiment. Six release times are indicated with 'o' markers and vertical lines. Times are presented in EDT. B,C,D,E,F,G) Simulated (white) and observed (red) drifter releases during the third field experiment. Simulated (black) and observed (magenta) release locations indicated as dots. Simulated drifter release and collection times were 30 minutes apart. Sufficiently long observed drifter tracks were separated into 30 minute segments.

#### **5.4.2 Comparisons of Drifter Tracks Simulated with Different Bathymetries**

Hydrodynamics were simulated near the Indian River Inlet using several model input bathymetries. A gridded bathymetry input '.xyz' file was compiled from the NOAA post-sandy digital elevation model (DEM) and interpolated onto the selected computational grid to generate a bathymetry file in Delft3D QUICKIN. The first bathymetry option was created entirely from NOAA DEM values (Figure 41a). The primary difficulty, which motivated the testing of alternate bathymetry options, was the large differences between model and measured water depth at the sensor locations in Aquadopp array four. The sensors in the fourth Aquadopp array were between approximately 400 m to 1400 m north and 130 m to 260 m west of the north jetty tip, and at the two northernmost sites bathymetry errors were nearly 3 m. Bathymetric differences prevented useful comparisons with data from the fourth Aquadopp deployment. A second bathymetry option was developed using elevation data compiled as part of the modeling effort of Keshtpoor et al. (2015). The second bathymetry option involved a relatively narrow rectangular section of elevation data, which spanned approximately half of the Delaware Atlantic coast, replacing bathymetry data from the NOAA DEM in Delft3D QUICKIN (Figure 41b). Differences between bathymetry options were particularly relevant in the nearshore to the north of the inlet and the ebb shoal, exceeding 2 m in locations (Figure 41c). Bathymetry option one included an erroneously shallow nearshore in various locations immediately north of the inlet. Ebb shoal shape and the depth of the surrounding areas also varied substantially between the two bathymetry options. Elevation difference patterns were typically less than 2 m farther than 2 km from the inlet.

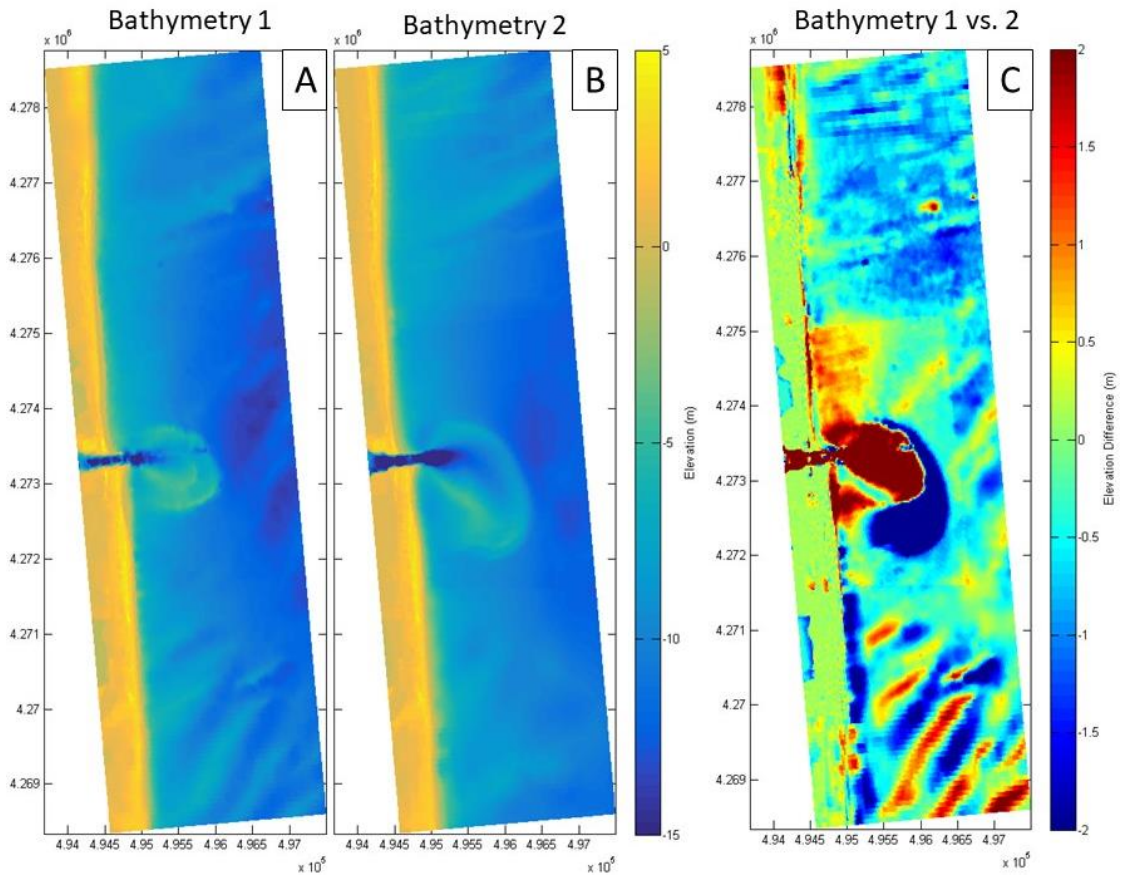


Figure 41: A) A selection of model input elevation generated using bathymetry option one near the Indian River Inlet, generated entirely from the NOAA post-sandy DEM. Color indicates elevation. B) Model input elevation near the Indian River Inlet using elevation data compiled for the modelling effort of Keshtpoor et al. (2015). C) Elevation differences between bathymetry options one and two near the Indian River Inlet. Color indicates elevation difference, with positive values indicating higher elevations in bathymetry option one.

Model simulations used for Willmott score validations and observed drifter track comparisons included the elevation changes introduced for bathymetry option two. Changing bathymetry options during the modeling effort resulted in hydrodynamic predictions for both options. The impact of the bathymetric changes

between the two data sources are particularly evident in comparisons of simulated drifter tracks using the two options. Hydrodynamics near the inlet were simulated with both bathymetry options using the same forcing conditions, passive tracer grid, release times, and retrieval times.

In the rising tide, simulated drifter tracks indicate substantially different current patterns between simulations using the two bathymetry options. Simulated drifters released at the start of the  $\pi/6$  tidal phase within 300 m north of the inlet follow substantially different paths between the two bathymetry options. Drifters simulated with bathymetry option one travel into the ebb jet and recirculate north into two eddy-like patterns in the  $\pi/6$  tidal phase, which is entirely absent from the relatively low dispersion ebb jet of the bathymetry option two simulation (Figure 42a, Figure 42b). At the beginning of the  $3\pi/6$  tidal phase the flow pattern within 300 m north of the inlet include a clearly defined flow separation following a line to the northwest using bathymetry option two while simulations using bathymetry option one predicted slower speeds and larger variability in flow direction (Figure 48c, Figure 42d). At the start of the  $5\pi/6$  tidal phase simulations using bathymetry option two predicted a flow divergence point approximately 1000 m north of the inlet while simulations using bathymetry option one predicted smaller velocities and flow divergence farther to the north (Figure 42e, Figure 42f).

In the falling tide, drifter tracks were more similar between simulations using bathymetry options one and two. Drifter track easting velocity magnitudes north of the inlet during the  $7\pi/6$  simulated with bathymetry option one were typically less than easting velocity magnitudes simulated with bathymetry option two (Figure 42g, Figure 42h). Simulated drifter tracks at the start of the  $9\pi/6$  tidal phase were similar between

bathymetry options, but with different easting velocity components within 100 m north of the inlet and a different ebb jet angle (Figure 42i, Figure 42j). The  $11\pi/6$  tidal phase also had similar drifter tracks in simulations with both bathymetry options, with variations in easting velocity approximately 200 m east of the north jetty tip (Figure 42k, Figure 42l).

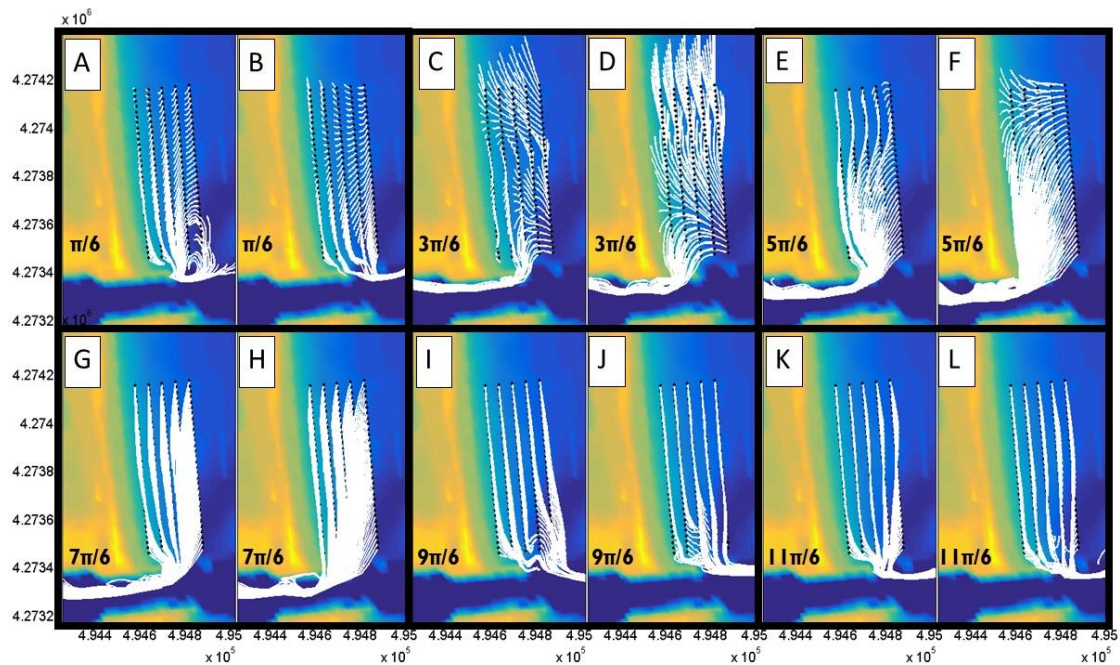


Figure 42: A,C,E,G,I,K) Simulated drifter tracks from model simulations using bathymetry option one, released at the beginning of the  $\pi/6$ ,  $3\pi/6$ ,  $5\pi/6$ ,  $7\pi/6$ ,  $9\pi/6$ , and  $11\pi/6$  tidal phases. B,D,F,H,J,L) Simulated drifter tracks from model simulations using bathymetry option two.

Comparisons of drifter tracks simulated with different model bathymetries for the same area indicated relatively important changes to local current patterns, particularly during the rising tide. Ebb jet patterns in the early rising tide and flow

divergence point location and importance in the middle to late rising tide vary substantially with bathymetry. As both bathymetry options were generated using relatively recent data, comparisons between the two are related to the importance of accurate bathymetry in numerically simulating the current patterns around the Indian River Inlet. Simulations of features such as the flow divergence point north of the inlet and the final ebb jet shapes are shown to be largely dependent on bathymetry. Model simulations indicate accurate bathymetry data are important for current pattern predictions.

#### **5.4.3 The Relative Importance of Tide and Wave Forcing to Current Patterns near the Indian River Inlet**

Hydrodynamics near the Indian River Inlet during the Aquadopp deployments were simulated with and without wave forcing to compare the impact of wave and tidal forcing on the Willmott skill score ( $d$ ) validations of Eulerian quantities. All simulations included tidal forcing, as water level variations on the order of 1 m often have large impacts on shallow water wave predictions. The exclusion of wave forcing from simulations generally had a small impact on water level and easting velocity skill scores (Table 5). The simulations which included wave forcing predicted water levels with an average of 0.014 lower Willmott scores and a mean index of agreement difference of 0.035. Easting velocity prediction skill scores typically improved with the inclusion of waves with a mean increase of 0.074 and a mean change of magnitude 0.0913. Northing velocity was substantially impacted by waves, with a mean decrease of 0.209 in simulations with waves. The decrease in northing velocity skill score is largely related to the over-prediction of northing velocities north of the inlet under the large waves which were present during the beginning of the Aquadopp array four

sample (Figure 49c). The sites not in Aquadopp array four indicate a mean decrease in northing velocity Willmott skill score of 0.105. While water level predictions did not depend substantially on wave processes, the inclusion of waves in simulations contributed 0.0913 of the easting velocity validation and decreased northing velocity by 0.105 for significant wave heights less than 1 m. Willmott skill score comparisons indicate that, other than during large wave conditions, water levels and velocities are dominated by tidal forcing rather than wave forcing. The impact of wave forcing on flow velocities for sub-meter significant wave heights is not negligible, however, the contribution of tidal forcing is substantially greater.

Table 5: Water level ( $h$ ), easting velocity ( $u$ ), and northing velocity ( $v$ ) Willmott skill score (index of agreement,  $d$ ) validations for simulations with and without wave forcing.

Site	Wave and Tide Forcing			Tidal Forcing Only		
	$h$	$u$	$v$	$h$	$u$	$v$
C1	0.986	0.726	0.731	0.972	0.727	0.775
D1	0.987	0.294	0.667	0.971	0.305	0.707
A2	0.962	0.896	0.736	0.932	0.903	0.774
B2	0.964	0.892	0.291	0.932	0.308	0.588
A4	0.838	0.384	0.336	0.948	0.373	0.771
B4	0.95	0.369	0.551	0.948	0.377	0.864
C4	0.951	0.263	0.362	0.949	0.133	0.786
D4	0.951	0.409	0.573	0.949	0.39	0.795
E4	0.84	0.452	0.688	0.95	0.503	0.76

Table 6: Willmott skill score differences in water level, easting velocity, and northing velocity validations with and without wave forcing.

Site	$h$	$u$	$v$
C1	-0.014	0.001	0.044
D1	-0.016	0.011	0.04
A2	-0.03	0.007	0.038
B2	-0.032	-0.584	0.297
A4	0.11	-0.011	0.435
B4	-0.002	0.008	0.313
C4	-0.002	-0.13	0.424
D4	-0.002	-0.019	0.222
E4	0.11	0.051	0.072

Hydrodynamics during the third field experiment were simulated with and without wave forcing in the study area to compare of the impact of wave and tidal forcing on current patterns and drifter tracks. Model drifters were released every 5 minutes and collected after 30 minutes (Figure 43). Drifter tracks were typically similar lengths with and without wave forcing, indicating similar flow speeds. The majority of drifters followed similar paths with and without wave forcing, with tracks gradually separating over the 30-minute release duration. The gradual separation of the drifter tracks with different forcing options likely reflects the integral of small changes in the flow field. Drifter tracks in the inlet channel or ebb jet were largely unchanged with the inclusion or exclusion of wave forcing. Simulated flow features such as the circulation cell in the  $\pi/6$  tidal phase, or the flow divergence point in the  $3\pi/6$ , and  $5\pi/6$  tidal phases were similar with both forcing conditions, indicating a tidal dependence. Simulated drifter track lengths were substantially different near the shore to the north of the inlet. Wave forcing was predicted to drive flow patterns near the shore and tidal forcing is predicted to dominate currents over the rest of the domain. Tidal forcing is indicated to drive flow features such the predicted circulation cell and flow divergence point.

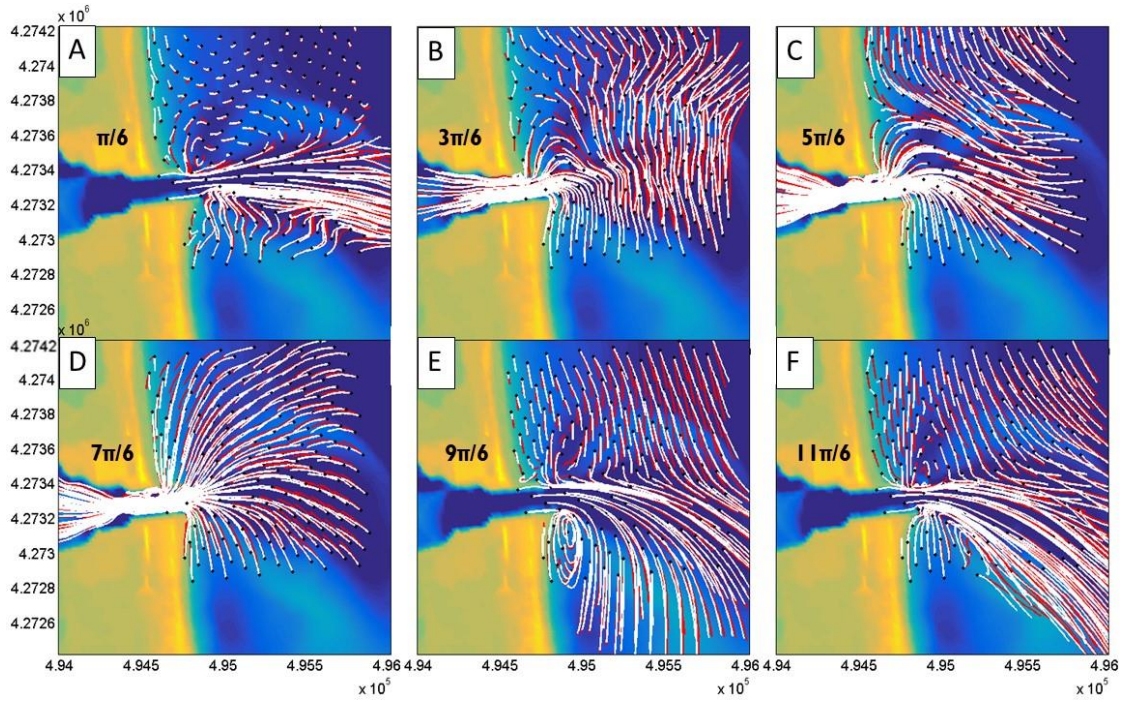


Figure 43: Model drifter tracks using tidal and wave forcing (white) at various phases of the tidal cycle compared with model drifter tracks using tidal forcing only (red). Release points are presented as dots. Simulated drifter release and collection times were separated by 30 minutes.

## Chapter 6

### CONCLUSIONS

A suite of GPS-tracked current-following Lagrangian drifters were designed and constructed to study current patterns to the north of the Indian River Inlet, which has been the location of chronic erosion and numerous sediment nourishment projects. Drifters were deployed within 1000 m north of the inlet during four field experiments spanning the entire semi-diurnal tidal cycle. Hydrodynamics near the inlet were predicted in 2D dynamically coupled Delft3D-FLOW and Delft3D-WAVE simulations. Numerical model setup was quantitatively validated with previously collected Eulerian current meter data and qualitatively compared with observed drifter tracks.

Measured drifter tracks indicate that many of the flow features near the Indian River Inlet are tidally controlled. Drifter measurements were separated by tidal phase and expressed as twelve fractions of  $2\pi$ . With flow into the inlet, during the  $3\pi/6$ ,  $4\pi/6$ , and  $5\pi/6$  tidal phases observed drifter tracks indicated a flow divergence point to the north of the inlet at variable locations. Observed flow reversal within the inlet was between 1 and 1.5 hours after high tide within the inlet. With flow out of the inlet, between the  $9\pi/6$  and  $\pi/6$  tidal phases, observed flow north of the inlet was to the southeast and into the ebb jet. Ebb jet deflection was observed to decrease with tidal phase. During the tidal phases with flow reversal (i.e.  $2\pi/6$ ,  $7\pi/6$ , and  $8\pi/6$ ) observed flow patterns displayed the most variation with factors other than tidal phase. Drifter velocities north of the inlet were typically between  $0.1 \text{ m s}^{-1}$  and  $0.3 \text{ m s}^{-1}$ , with velocities south of the north jetty tip generally greater than  $0.35 \text{ m s}^{-1}$  and often greater than  $0.45 \text{ m s}^{-1}$ .

Delft3D simulations predicted Eulerian quantities with a wide range of skill scores. Willmott scores ( $d$ ) and refined Willmott scores ( $d_r$ ) were calculated to compare measured Aquadopp data to simulation results at nine points near the inlet. Water level was predicted well with mean  $d$  of 0.94 and mean  $d_r$  of 0.77. Easting velocity was predicted with varied skills, having a mean  $d$  of 0.52 and mean  $d_r$  of 0.22, but large standard deviations of 0.25 and 0.26. Northing velocity predictions also had varied skill scores, with a mean  $d$  of 0.55 and a mean  $d_r$  of 0.34 and standard deviations of 0.18 and 0.26. Currents were predicted well near the inlet, but simulations failed to capture an eastward flow direction shift landward of the north jetty tip. More than 100 m from the inlet, easting velocities were predicted poorly and northing velocities were predicted well outside of large wave events. Significant wave heights were not predicted remarkably well, with a mean  $d$  of 0.49 but a mean  $d_r$  of -0.12. Peak period prediction skill scores were satisfactory, with a mean  $d$  of 0.50, a mean  $d_r$  of 0.26, and standard deviations of 0.10 and 0.20. Wave direction was predicted fairly poorly, with a mean  $d$  of 0.25 and a mean  $d_r$  of -0.50. Water level and current predictions generally captured overall trends better than wave characteristic predictions.

Simulated current patterns were qualitatively compared to observed drifter tracks. The model reproduced observed flow patterns well north of the inlet during the three later quarters of the falling tide, in the ebb jet sufficiently after flow reversal, and within 100 m north of the inlet in the middle of the rising tide. Simulated current patterns north of the inlet did not match observations during the early rising or early falling tide. The model also predicted inlet flow reversal from flooding to ebbing too early. Simulated current patterns surrounding the divergence point generally matched

observed drifter track shapes, but flow divergence point locations were frequently predicted 100 m to 400 m too far north. Model current pattern agreement with observations tended to decline near high and low tide, but with general agreement sufficiently before or after inlet flow reversal. Both model simulations and observations indicate a flow divergence point north of the inlet in the middle of the rising tide and a decrease in ebb jet deflection through the falling tide.

The comparisons of simulations distinguished by a single variation allowed issues such as the impact of localized bathymetric changes and the dominant forcing mechanism to be addressed. Accurate bathymetry was determined to be important to hydrodynamic predictions of the area based on simulations conducted with different bathymetry sources. Changing bathymetry sources introduced substantial variations in simulated flow patterns. Bathymetric inaccuracies likely impacted all simulated flow patterns. Simulated water levels, velocities, and drifter tracks also indicated that tidal forcing is dominant over the majority of the study area. Skill score comparisons indicate that the accuracy of predictions is largely dependent on tidal forcing. Simulated drifter track comparisons with and without wave forcing indicate a tidal dominance over the majority of the study and in flow features such as the divergence point and the current patterns around flow into or out of the inlet.

## REFERENCES

- Andres, A. S. (1987). Estimate of direct discharge of fresh ground water to Rehoboth and Indian River bays. Newark, DE: Delaware Geological Survey, University of Delaware.
- Austin, M. J., Scott, T. M., Russell, P. E., & Masselink, G. (2012). Rip current prediction: development, validation, and evaluation of an operational tool. *Journal of coastal research*, 29(2), 283-300.
- Bertin, X., Fortunato, A. B., & Oliveira, A. (2009). A modeling-based analysis of processes driving wave-dominated inlets. *Continental Shelf Research*, 29(5), 819-834.
- Bruun, P. (1995). The development of downdrift erosion. *Journal of Coastal Research*, 1242-1257.
- Bruun, P. (2001). The development of downdrift erosion: an update of paper in JCR, Vol. 11 (4). *Journal of coastal research*, 82-89.
- Chang, M. S. (1969). Mass transport in deep-water long-crested random gravity waves. *Journal of Geophysical Research*, 74(6), 1515-1536.
- Chen, J. L., Hsu, T. J., Shi, F., Raubenheimer, B., & Elgar, S. (2015). Hydrodynamic and sediment transport modeling of New River Inlet (NC) under the interaction of tides and waves. *Journal of Geophysical Research: Oceans*, 120(6), 4028-4047.
- Churchill, J. H., Hench, J. L., Luettich, R. A., Blanton, J. O., & Werner, F. E. (1999). Flood tide circulation near Beaufort Inlet, North Carolina: implications for larval recruitment. *Estuaries and Coasts*, 22(4), 1057-1070.
- Davis, R. A., & Fox, W. T. (1981). Interaction between wave-and tide-generated processes at the mouth of a microtidal estuary: Matanzas River, Florida (USA). *Marine Geology*, 40(1), 49-68.
- Davis, R. E. (1985). Drifter observations of coastal surface currents during CODE: The statistical and dynamical views. *Journal of Geophysical Research: Oceans*, 90(C3), 4756-4772.
- Delft Hydraulics, (2014a). Delft3D-FLOW User Manual: Simulation of multi-dimensional hydrodynamic flows and transport phenomena, including sediments. Hydro-morphodynamics. Technical report.

- Delft Hydraulics, (2014b). Delft3D-WAVE User Manual: Simulation of short-crested waves with SWAN. Hydro-morphodynamics. Technical report.
- DiCosmo, N. R. (2015). Hydrodynamics and sediment transport offshore of the downdrift beach and southern ebb shoal of Indian River Inlet, DE. University of Delaware.
- Dissanayake, D. M. P. K., Roelvink, J. A., & Van der Wegen, M. (2009). Modelled channel patterns in a schematized tidal inlet. *Coastal Engineering*, 56(11), 1069-1083.
- Dodet, G., Bertin, X., Bruneau, N., Fortunato, A. B., Nahon, A., & Roland, A. (2013). Wave-current interactions in a wave-dominated tidal inlet. *Journal of Geophysical Research: Oceans*, 118(3), 1587-1605.
- FitzGerald, D. M. (1996). Geomorphic variability and morphologic and sedimentologic controls on tidal inlets. *Journal of Coastal Research*, 47-71.
- Galgano, F. A. (2008). Shoreline behavior along the Atlantic coast of Delaware. *Middle States Geographer*, 41, 74-81.
- Galgano, F. A. (2009). Beach erosion adjacent to stabilized microtidal inlets. *Middle States Geographer*, 42, 18-32.
- Gebert, J. A., Watson, K. D., & Rambo, A. T. (1992). 57 years of coastal engineering practice at a problem inlet: Indian River Inlet, Delaware. In *Coastal Engineering Practice* (pp. 503-519). ASCE.
- Hansen, J. E., Elias, E., List, J. H., Erikson, L. H., & Barnard, P. L. (2013). Tidally influenced alongshore circulation at an inlet-adjacent shoreline. *Continental Shelf Research*, 56, 26-38.
- Hayes, M. O. (1980). General morphology and sediment patterns in tidal inlets. *Sedimentary geology*, 26(1), 139-156.
- Hench, J. L., & Luettich Jr, R. A. (2003). Transient tidal circulation and momentum balances at a shallow inlet. *Journal of Physical Oceanography*, 33(4), 913-932.
- Johnson, D., Stocker, R., Head, R., Imberger, J., & Pattiaratchi, C. (2003). A compact, low-cost GPS drifter for use in the oceanic nearshore zone, lakes, and estuaries. *Journal of atmospheric and oceanic technology*, 20(12), 1880-1884.

- Johnson, D., & Pattiaratchi, C. (2004). Transient rip currents and nearshore circulation on a swell-dominated beach. *Journal of Geophysical Research: Oceans*, 109(C2).
- Keshtpoor, M., Puleo, J. A., Gebert, J., & Plant, N. G. (2013). Beach response to a fixed sand bypassing system. *Coastal Engineering*, 73, 28-42.
- Keshtpoor, M., Puleo, J. A., Shi, F., & DiCosmo, N. R. (2014). Numerical simulation of nearshore hydrodynamics and sediment transport downdrift of a tidal inlet. *Journal of Waterway, Port, Coastal, and Ocean Engineering*, 141(2), 04014035.
- MacMahan, J., Brown, J., & Thornton, E. (2009). Low-cost handheld global positioning system for measuring surf-zone currents. *Journal of Coastal Research*, 744-754.
- Moffatt, J., & Nichol, F. (2007). Sediment management plan: Rehoboth Bay, Sussex County, Delaware. DNREC Final Rep.
- Molinari, R., & Kirwan Jr, A. D. (1975). Calculations of differential kinematic properties from Lagrangian observations in the western Caribbean Sea. *Journal of Physical Oceanography*, 5(3), 483-491.
- Monahan, E. C., & Monahan, E. A. (1973). Trends in drogue design. *Limnology and Oceanography*, 18(6), 981-985.
- Murray, S. P. (1975). Trajectories and Speeds of Wind-Driven Currents Near the Coast. *Journal of Physical Oceanography*, 5(2), 347-360.
- O'Brien, M. P. (1967). Equilibrium flow areas of tidal inlets on sandy coasts. In *Coastal Engineering 1966* (pp. 676-686).
- Okubo, A., & Ebbesmeyer, C. C. (1976). Determination of vorticity, divergence, and deformation rates from analysis of drogue observations. In *Deep Sea Research and Oceanographic Abstracts* (Vol. 23, No. 4, pp. 349-352). Elsevier.
- Olabarrieta, M., Warner, J. C., & Kumar, N. (2011). Wave-current interaction in Willapa Bay. *Journal of Geophysical Research: Oceans*, 116(C12).
- Orescanin, M., Raubenheimer, B., & Elgar, S. (2014). Observations of wave effects on inlet circulation. *Continental Shelf Research*, 82, 37-42.

- Puleo, J. A. (2010). Estimating alongshore sediment transport and the nodal point location on the Delaware–Maryland coast. *Journal of waterway, port, coastal, and ocean engineering*, 136(3), 135-144.
- Puleo, J. A., Hutschenreuter, K., Cowan, P., Carey, W., Arford-Granholm, M., & McKenna, K. K. (2016). Delaware surf zone injuries and associated environmental conditions. *Natural Hazards*, 81(2), 845.
- Roberts, T. M., Wang, P., & Puleo, J. A. (2013). Storm-driven cyclic beach morphodynamics of a mixed sand and gravel beach along the Mid-Atlantic Coast, USA. *Marine Geology*, 346, 403-421.
- Schmidt, W. E., Woodward, B. T., Millikan, K. S., Guza, R. T., Raubenheimer, B., & Elgar, S. (2003). A GPS-tracked surf zone drifter. *Journal of Atmospheric and Oceanic Technology*, 20(7), 1069-1075.
- Schmidt, W. E., Guza, R. T., & Slinn, D. N. (2005). Surf zone currents over irregular bathymetry: Drifter observations and numerical simulations. *Journal of Geophysical Research: Oceans*, 110(C12).
- Scott, T., Austin, M., Masselink, G., & Russell, P. (2016). Dynamics of rip currents associated with groynes—field measurements, modelling and implications for beach safety. *Coastal Engineering*, 107, 53-69.
- Shi, F., Hanes, D. M., Kirby, J. T., Erikson, L., Barnard, P., & Eshleman, J. (2011). Pressure-gradient-driven nearshore circulation on a beach influenced by a large inlet-tidal shoal system. *Journal of Geophysical Research: Oceans*, 116(C4).
- Spencer, D., Lemckert, C. J., Yu, Y., Gustafson, J., Lee, S. Y., & Zhang, H. (2014). Quantifying dispersion in an estuary: A Lagrangian drifter approach. *Journal of Coastal Research*, 70(sp1), 29-34.
- Spydell, M., Feddersen, F., Guza, R. T., & Schmidt, W. E. (2007). Observing surf-zone dispersion with drifters. *Journal of Physical Oceanography*, 37(12), 2920-2939.
- Spydell, M. S., Feddersen, F., & Guza, R. T. (2009). Observations of drifter dispersion in the surfzone: The effect of sheared alongshore currents. *Journal of Geophysical Research: Oceans*, 114(C7).
- Spydell, M. S., Feddersen, F., Olabarrieta, M., Chen, J., Guza, R. T., Raubenheimer, B., & Elgar, S. (2015). Observed and modeled drifters at a tidal inlet. *Journal of Geophysical Research: Oceans*, 120(7), 4825-4844.

- Wargula, A., Raubenheimer, B., & Elgar, S. (2014). Wave-driven along-channel subtidal flows in a well-mixed ocean inlet. *Journal of Geophysical Research: Oceans*, 119(5), 2987-3001.
- Willmott, C. J. (1981). On the validation of models. *Physical geography*, 2(2), 184-194.
- Willmott, C. J., Robeson, S. M., & Matsuura, K. (2012). A refined index of model performance. *International Journal of Climatology*, 32(13), 2088-2094.
- Zippel, S., & Thomson, J. (2015). Wave breaking and turbulence at a tidal inlet. *Journal of Geophysical Research: Oceans*, 120(2), 1016-1031.